Thin-Film Electrostatic Actuators and Adhesives for High-Voltage Robotics

Ethan Schaler
Ronald S. Fearing, Ed.

Electrical Engineering and Computer Sciences
University of California at Berkeley

May 11, 2018

Thin-Film Electrostatic Actuators and Adhesives for High-Voltage Robotics

by

Ethan Weber Schaler

A dissertation submitted in partial satisfaction of the

requirements for the degree of

Doctor of Philosophy

in

Engineering – Electrical Engineering and Computer Sciences

in the

Graduate Division

of the

University of California, Berkeley

Committee in charge:

Prof. Ronald S. Fearing, Chair
Prof. Ana C. Arias
Prof. Kristofer S. J. Pister
Prof. Tarek I. Zohdi

Spring 2018

Thin-Film Electrostatic Actuators and Adhesives for High-Voltage Robotics

Abstract

Thin-Film Electrostatic Actuators and Adhesives for High-Voltage Robotics

by

Ethan Weber Schaler

Doctor of Philosophy in Engineering – Electrical Engineering and Computer Sciences

University of California, Berkeley

Prof. Ronald S. Fearing, Chair

Thin-film electrostatic actuators and adhesives operating at high-voltages have potential as light-weight, low-cost force sources in *mm*- to *cm*-scale robotics.

First, new designs for repulsive-force electrostatic actuators (RFAs) were fabricated and evaluated, including: 2-layer linear and rotary RFAs, multi-layer RFAs for increased stroke, and RFAs with work-optimized electrode geometries. Second, a new bidirectional repulsive-/attractive-force electrostatic actuator (RAFA) was introduced, which employs the RFA electrode patterns but can controllably generate either repulsive or attractive forces by simply varying two input voltages. Third, a flexible, 8-fingered robotic gripper was developed, which employs electrostatic adhesion to grasp and manipulate flexible films (such as satellite multi-layer insulation).

RFAs exhibit interesting characteristics – including stable open-loop operation and peak force at rest – and are compatible with thin-film / planar manufacturing processes. Demonstrated applications include RFA-powered 1- and 2-DoF micro-mirror systems, and a RAFA-powered 132 *mg* crawling robot.

Contents

List of Figures

List of Tables

Acknowledgments

I would like to give a huge thank you to everyone in the Biomimetic Millisystems Lab, especially my advisor – Ron Fearing – those who graduated before me – Andrew Gillies, Cameron Rose, Jane Esterline, and Austin Buchan – and those racing me out – Carlos Casarez and Jessica Lee. I've been fortunate enough to work with two motivated, intelligent undergraduate researchers – Loren Jiang and Caitlyn Lee – who both made important contributions to my core research. I also look forward to seeing how the newest members of the lab – Ben McInroe, Anusha Nagabandi, and Justin Yim – conclude their own PhDs.

I'm grateful to my collaborators at UC Berkeley – Tarek Zohdi, Ali Javey, Hiroki Ota, and Yuji Gao – and at NASA Jet Propulsion Laboratory – Aaron Parness, Donald Ruffatto, Victor White, and Paul Glick – for exciting research projects in the past (and the future).

I appreciate the advice, mentoring, and support from members of my dissertation committee – Ana Arias, Kris Pister, and Tarek Zohdi – and qualification exam committee – Ali Javey, Liwei Lin, and Kris Pister – as my research has evolved and progressed over time.

I've made many wonderful friends at Berkeley – Dan Armendariz, Aaron Bestick, Dan Calderone, and Phil Sandborn (to name a few not mentioned elsewhere) – with whom I've shared the many climbing / hiking / camping adventures, long car rides, and late night conversations that have kept me sane over the past 6 years.

I'm most grateful for the support of my family. My Dad has always been ready to brainstorm new ideas, troubleshoot my experiments, listen as I vent my frustrations, and request co-authorship on my papers. My Mom has provided steadfast guidance throughout the trials and tribulations of academic life (while enjoying the same as a professor), and shows no sign of yielding the family title for most distinguished author anytime soon. She has also encouraged me to make time for proper food, exercise, and socializing – albeit with a bit of a "do as I say, not as I do" attitude. My Brother has made his own remarkable progress life – succeeding in challenging internships, developing his own research expertise, graduating, publishing, and starting a life in NYC – so I can't wait to see what he accomplishes next!

I wouldn't have achieved this without you all.

Chapter 1

Introduction

The Biomimetic Millisystems Lab develops a variety of mobile *cm*-scale robots, that are lightweight, robust, and highly capable. The past 20 years of research have been devoted to constructing crawling [52], running [9, 36, 37], climbing [10], and flying robots [4, 5, 58, 80], which have demonstrated open-loop stable high-speed running [36, 37], controlled diving [92], smooth-surface climbing [10, 79], collaborative behavior (step climbing [13], launching [91], flying [58]), and more.

These robots are primarily manufactured using a versatile in-house process known as Smart Composite Microstructures (SCM) [126]. SCM consists of thin-films / sheets of various materials that are individually patterned, layered, and bonded together to form a functional multi-layer composite. The materials in each layer of the composite can be selected to meet required functions, including:

Structure: Stiff, durable, high strength-to-weight, (e.g. Carbon fiber, PET, Cardboard)

Flexure: Flexible, durable, high peel / tear strength (e.g. PET, Rip-stop nylon, Polyimide)

Sensor: Mechanical / chemical transducer, conductor (e.g. Surface-mount chips, Piezoresistive materials, Conductive wiring)

Actuator: High power-to-weight, high force-to-weight (e.g. Piezoelectric actuator, Shape memory polymer, Electrostatic actuator)

SCM composites are then assembled into various robot structures – including rigid chassis, hinged linkages, legs, wings, sensor bodies, and more – and connected to the robot's powerplant – typically electromagnetic motors with a gearbox [9, 37], piezoelectric actuators [7, 32, 49, 69, 107, 108], or shape-memory alloy wires [6, 50, 52, 64].

Prior SCM robots have also demonstrated structures, flexures and sensors integrated in a single SCM stack [35]. However, these SCM robots do not have an actuation source integrated directly into the SCM stack, but rather fabricated / assembled separately and connected via SCM linkages. My research seeks to change this, by developing an SCM-compatible actuator (Table 1.1).

Table 1.1: SCM elements and examples of fabricated devices. Note that [97, 98, 100] contain my SCM-compatible actuator work included in this dissertation, and [35] contains my work on an SCM-compatible sensor.

SCM Element	Example	Rigid	Compliant	Functional	Source
Structure / Flexure	Robot Bodies (1st Gen.)	Cardboard	PET	–	[9]
Structure / Flexure	Robot Bodies (2nd Gen.)	PET	Ripstop Nylon	–	[14]
Sensor	Tactile Sensor (Body-Integrated)	Flex-PCB	Foam	–	[35]
Sensor	Strain Gauge (Leg-Integrated)	Fiberglass	PDMS	CNT / Ag-NP Ink	[35]
Actuator	Micro-Mirror (1-DoF)	Copper	Polyimide	RFA	[100]
Actuator	Micro-Mirror (2-DoF)	Stainless Steel	Polyimide	RFA	[97]
Actuator	Milli-Robot (Inchworm)	Carbon Fiber	Polyimide	RAFA	[98]

RFA – Repulsive-Force Electrostatic Actuator   **RAFA** – Repulsive-/Attractive-Force Electrostatic Actuator

Future SCM-integrated actuators could provide controllable power for limb actuation – the primary actuation requirement in small, mobile robots – but also power a wide variety of auxiliary functions including active damping / stiffening (for gait modification, turning, or rapid deceleration during locomotion) [50], variable mechanical advantage (by changing lever-arm lengths to transition from running to jumping), and joint locking (for low-power static positioning) [2]. In each case, the actuator element would be manufactured as layers within the SCM stack to provide either out-of-plane normal forces or in-plane shear forces.

To select an ideal technology for this SCM-compatible actuator, we observed that a number of thin-film actuator technologies exist, including: shape memory alloy / polymer, piezoelectric actuators, and electrostatic actuators [60]. The SCM-compatible actuator also needs to meet three other demands, in order for the SCM actuator to have the same versatility as the other SCM layers:

1. Material interchangeability (so we can tune the SCM mechanical properties)

2. Electrically powered (so it operates in the same fashion as SCM sensor layers)

3. Fabrication / operation at the *mm*- to *cm*-scale

The first two requirements eliminate shape memory polymers and piezoelectric actuators, which both require relatively exotic materials with limited material properties, and focused our attention on electrostatic actuators, which can utilize any combination of conducting / insulating materials. Electrostatic actuators also have inherently simple electrode designs that are easily fabricated on the *μm*- to *cm*-scale using conventional manufacturing processes.

A number of thin-film electrostatic actuator technologies exist – film slider [74, 122], parallel plate / stackable (LSEA) [55, 72], zipper [15], scratch drive [19, 104], and dielectric elastomer [76] – as well as several MEMS-scale electrostatic technologies that could still yield useable forces at the *mm*-scale – distributed electrostatic (DEMA) / integrated force arrays [11, 72], and repulsive-force electrostatic actuators [41, 44, 45, 113].

For this initial SCM-compatible actuator, we selected a repulsive-force electrostatic actuator (RFA) technology that generates out-of-plane forces / motion. The decision to focus

on a repulsive-force electrostatic actuator was three-fold: RFAs have open-loop stable operation by generating peak-force at initial / rest positions, RFAs can be designed to avoid certain failure modes (pull-in, stiction, or shorting) common to attractive-force electrostatic actuators, and RFAs have only been fabricated at the MEMS-scale prior to this work.

1.1 Overview

In this dissertation, I will present my work on three designs for thin-film electrostatic actuators and a thin-film electrostatic adhesive:

In Chapter 2, I demonstrate thin-film repulsive-force electrostatic actuators (RFAs) that employ a new electrode pattern, are fabricated for the first time at the mm-scale, and are useful for low-force actuation applications. Compared to prior patterns, the new electrode geometry increases electrostatic force production by an order of magnitude (at equal voltages) and eliminates the most common shorting failure modes. These electrostatic actuators have stable open-loop operation with no pull-in instability, low mechanical hysteresis, and peak force in rest configurations. The actuators are fabricated with a planar, flex-circuit manufacturing process, allowing production at scale and over large areas. Two-layer out-of-plane linear actuators (25 x 10 mm electrode area) were characterized: with 0–1000 V inputs ($40 \cdot 10^6$ V/m), blocked normal forces of 9.03 mN (36.1 Pa) were generated, and controllable linear displacements up to 511 μm were measured across an open loop bandwidth of 43 Hz. Finally, we present a 290 mg 1-DoF micro-mirror system for laser beam steering that uses a two-layer out-of-plane rotational actuator for open-loop stable operation with controlled angular displacements up to 5.1° at 1000 V / 16 Hz. This work was published in *Sensors and Actuators A: Physical* [100].

In Chapter 3, I present a two degree-of-freedom micro-mirror system driven by 4 flexible, multi-layer thin-film repulsive-force electrostatic actuators (RFAs, each 13 x 19.5 mm). We demonstrate a functional multi-layer (>2-layer) RFA: it uses 4 – 8 layers for increased stroke length, has stable actuation without pull-in, has a consistent electrode pattern on each layer for ease of fabrication, separates oppositely-polarized electrodes on each layer with a polyimide substrate to prevent intra-layer shorting, and orients like-polarized electrodes on adjacent layers to prevent inter-layer shorting. We use four 4-layer RFAs (in antagonist pairs) to drive a micro-mirror system with 62 Hz bandwidth and 8.8° / 7.6°, stable, controllable rotations about 2-DoF at up to 2000 V. This work will appear at *Actuators 2018* [97].

In Chapter 4, I demonstrate a new thin-film electrostatic actuator (RAFA) capable of generating bidirectional repulsive- and attractive-forces. The two-layer actuator controllably produces measured electrostatic pressures up to 156 Pa (38.9 mN, for 2.5 cm^2 electrode area) in repulsion and 352 Pa (88.0 mN) in attraction when operating at 0–1.2 kV. The four

patterned electrodes (two per layer) have a cross-section geometry optimized in simulation for maximum blocked force over a 25–500 μm stroke length. RAFAR, a 132 mg milli-robot, uses a 1.45 cm^2 RAFA to crawl at 0.32 mm/s with anisotropic friction feet. This work will appear at *MARSS 2018* [98].

In Chapter 5, I present a flexible, electrostatic adhesive gripper designed to controllably grasp and manipulate soft goods in space. The 8-fingered gripper has 50 cm^2 of active electrodes operating at 3 kV. It generates electrostatic adhesion forces up to 3.5 N (0.70 kPa) on Ge-coated polyimide film and 1.2 N on a multi-layer insulation (MLI) blanket, a film composite used for satellite thermal insulation. Extremely low-force gripper engagement (0.08 N) and release (0.04 N) of films is ideal for micro-gravity. Individual fingers generate shear adhesion forces up to 4.76 N (5.04 kPa) using electrostatic adhesive and 45.0 N (47.6 kPa) with a hybrid electrostatic / gecko adhesive. To simulate a satellite servicing task, the gripper was mounted on a 7-DoF robot arm and performed a supervised grasp, manipulate, and release sequence on a hanging, Al-coated PET film. This work appeared at *IROS 2017* [99].

In Chapter 6, I conclude by summarizing the advances in thin-film electrostatic actuators / adhesives made over the course of this research, identifying areas of research still ripe for exploration, and highlighting potential applications of these technologies.

Chapter 2

Thin-Film Repulsive-Force Electrostatic Actuators

Content in this chapter was originally published as "Thin-Film Repulsive-Force Electrostatic Actuators," *Sensors and Actuators A: Physical* [100].

2.1 Introduction

Advances in planar manufacturing have leveraged new processes and materials to develop a range of innovative robots and sensors [35, 51, 82, 111, 124, 126]. Devices are composed of functional materials (films, fabrics, composites, inks, etc.) and use layering, patterning, folding, and bonding steps to form complex kinematic structures with integrated circuitry [35]. We apply these same standard manufacturing steps to fabricate thin-film repulsive-force electrostatic actuators.

Our initial goal is to produce *cm*-scale planar actuators, capable of generating *mN* forces and *mm* displacements at ∼30 *Hz* (video-compatible) frequencies, for applications in mobile robotics (i.e. a lightweight laser beam steering system) and beyond. Numerous viable actuator technologies exist at this scale: successful implementations of thermal / shape memory [38, 117], piezoelectric [56], dielectric elastomer [103, 105], and (attractive-force) electrostatic [15, 55, 72, 104] planar actuators have all been demonstrated, and the merits of each have been comprehensively discussed [53, 60]. Electrostatic actuators have the benefits of operating with larger displacements than piezoelectric actuators and higher speeds than thermal / shape memory actuators, and are well-suited for planar manufacturing. We focus specifically on repulsive-force electrostatic actuators, due to advantages in stability, controllability, and reliability over other electrostatic actuators.

In this chapter, we demonstrate a new electrode geometry for planar repulsive-force electrostatic actuators (RFA) – see Fig. 2.1 – that operates with increased forces, displacements, and field strengths as compared to existing RFA designs. The new RFA is simulated to
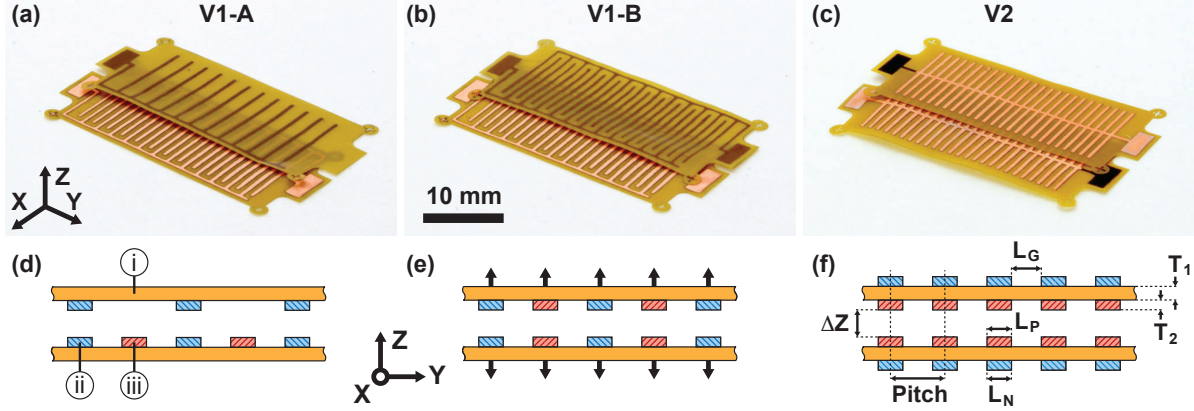
Figure 2.1: Flexible, two-layer repulsive-force actuator designs evaluated in this work: (a) V1-A, the electrode design used by S. He, et al. [45], (b) V1-B, an improved design proposed by S. He, et al. [41], (c) V2, the electrode design used in this work. For each actuator electrode design, the two functional layers are photographed (a-c) and the cross-sections are illustrated (d-f). Each actuator layer is composed of a polyimide substrate (i) with negative (ii) and positive (iii) electrodes. Actuator layers experience a net repulsive electrostatic pressure, illustrated in (e). Actuator dimensions include the substrate ($T_1 = 25~\mu m$) and electrode ($T_2 = 18~\mu m$) thickness, positive ($L_P = 500~\mu m$) and negative ($L_N = 500~\mu m$) electrode width, gap between adjacent electrodes ($L_G = 500~\mu m$), and inter-layer height (ΔZ).

establish performance bounds, fabricated using a flex-circuit planar manufacturing process, and characterized as the driving actuator in one degree-of-freedom linear and rotational systems.

2.2 Background

Electrostatic actuators typically consist of sets of moveable electrodes (conductive plates or combs) separated by an insulating dielectric, with electrostatic forces proportional to the charge accumulation on and electric fields between electrodes due to an applied electric potential. Operation of all electrostatic actuators is limited by electrical breakdown (shorting), which occurs when the electric field strength between electrodes exceeds the dielectric strength of the insulating medium (3–$110 \cdot 10^6$ V/m in air and 154–$303 \cdot 10^6$ V/m in polyimide) [23, 24, 54, 106]. A comparison of meso-scale electrostatic actuators is provided in Table 2.1.

At μm-scales, parallel plate actuators use electrodes arranged in pairs of parallel plates [128], and comb drive actuators use a pair of interdigitated combs [114]. To actuate, an applied voltage draws the electrodes together for gap-closing operation. To improve stroke length, the actuator output is often coupled to an inchworm mechanism [78]. At mm-scales,

Table 2.1: Survey of meso-scale electrostatic actuators, with key normalized metrics highlighted in grey.

Design	$\mathbf{A}$ / mm^2	$\mathbf{L}$ / mm	$\mathbf{\Delta L}$ / mm	ε / $\%$	$\mathbf{E}$ / V/m	$\mathbf{F}$ / N	$\mathbf{P}$ / Pa	$\mathbf{BW}$ / Hz	Source
Dielectric Elastomer	0.070 x 18	21	–	+61*	$43 \cdot 10^6$*	0.75	$600 \cdot 10^3$	15	[70]
Parallel Plate	0.040 x 1.56	0.97	0.124	+13	$21 \cdot 10^6$	$2.23 \cdot 10^{-3}$	$1.38 \cdot 10^3$	39*	[78]
Integrated Force Array	0.002 x 1	10	0.700	-7.0	$80 \cdot 10^6$	$62 \cdot 10^{-6}$	$28 \cdot 10^3$	–	[33]
Stacked Electro.	54 x 54	2.27	0.420	-20.5	$28 \cdot 10^6$	1.27	435	–	[55]
Electro. Film Slider	50 x 100	0.380	–	–	$14.3 \cdot 10^6$	4.4	880	–	[74]
Distributed Electro.	0.005 x 4	5	0.028	-0.6	$33 \cdot 10^6$	$6.3 \cdot 10^{-6}$	315	1.6*	[72]
Distributed Electro.	31 x 28	11	4	-36	$5 \cdot 10^6$	–	–	–	[72]
Zipper Electro.	50 x 10	18.1	18	-99*	$110 \cdot 10^6$	–	–	12	[15]
Repulsive Force	3.26 x 3.26	0.004	0.086	+2000	$3.8 \cdot 10^6$	$5 \cdot 10^{-6}$*	2.9*	80-200	[45]
RFA (V1-A)	80 x 10	0.136	–	–	$2 \cdot 10^6$	$2.74 \cdot 10^{-3}$	3.4	–	This Work
RFA (V1-B)	25 x 10	0.136	–	–	$2 \cdot 10^6$	$1.04 \cdot 10^{-3}$	4.2	–	This Work
RFA (V2)	25 x 10	0.431	0.511	**+119**	$40 \cdot 10^6$	$9.03 \cdot 10^{-3}$	**36.1**	**43**	This Work

$\mathbf{A}$ – Area (orthogonal to Stroke axis) $\mathbf{L}$ – Length (parallel to Stroke axis) $\mathbf{\Delta L}$ – Stroke Length
ε – Strain ($\mathbf{\Delta L/L}$, with + indicating expansion) $\mathbf{E}$ – Electric Field Strength $\mathbf{F}$ – Force
$\mathbf{P}$ – Pressure (solved from $\mathbf{F / A}$) $\mathbf{BW}$ – Frequency Bandwidth
(*) denotes properties calculated from provided information

integrated force arrays [11, 33] and distributed electrostatic actuators [72] are massively-parallelized actuators with 100s–1000s of connected parallel plate electrode units. Actuators at this scale are micro-fabricated, have high force density, low strains, and the highly-parallelized designs have low yields [11].

At cm-scales, dielectric elastomer actuators (DEA) use compliant electrodes fabricated on each side of low modulus elastomer film [70, 76, 77, 83]. DEAs generate large strains (60%) and high pressures (100s kPa) during operation: applied voltages thin the elastomer (distance between the electrodes) and stretch the cross-sectional area. DEAs also exhibit significant viscoelastic behavior due to the compliant elastomer film. Gap-closing distributed electrostatic actuators [72], stacked electrostatic actuators [55], and zipper electrostatic actuators [15] generate mm to cm strokes, sub-N forces, and 100s Pa pressures. Linear surface-drive electrostatic film actuators [74] and motors [122] are flex-circuit devices that generate up to 4.4 N forces and 100s Pa pressures.

Repulsive force electrostatic actuators (RFA) are a subset of electrostatic actuators that generate a net repulsive force (instead of attractive force) through clever configuration of the 2+ sets of differentially polarized electrodes [112]. Similarly charged electrodes oppose one another on moveable layers to generate the inter-layer repulsive force. Oppositely charged electrodes establish the electric fields and potential gradients in the actuator, but minimize attractive forces between moveable layers by: spacing oppositely-charged electrodes further apart than like-charged electrodes to produce weaker out-of-plane attractive forces, using symmetry to minimize in-plane attractive forces, and having attractive forces act as internal body forces on noncompliant substrates.

RFAs in general have low complexity, generate peak force at the initial displacement, have linear or rotational outputs based on suspension design (minimizing transmission requirements), and avoid many common failure modes of electrostatic actuators – RFAs have no pull-in limit, no increased likelihood of breakdown as electrodes displace normally, and no stiction problem.

RFAs were first reported by W. Tang, et al. [112]: electrodes patterned below a comb drive linear lateral resonator were used as a tunable electrostatic spring to control the height of the combs translating over the substrate, with measured out-of-plane displacements of 0.4–2 μm (from an initial 2 μm offset) at 30 V [113]. RFAs were further developed as a MEMS actuator for controllable 1-DoF [41–44] and 3-DoF [45,118] micro-mirrors. Modeling of two- and three-layer actuators and optimization of the electrode geometry show that maximum force is achieved when electrodes have equal width and spacing ($L_G = L_P = L_N$), and maximum out-of-plane displacement is proportional to in-plane electrode pitch [42,43]. Multiple RFAs were successfully fabricated with PolyMUMPs, including a 3-DoF micro-mirror system capable of out-of-plane translation (86 μm) and roll / pitch rotation ($\pm$ 1.5°) at 200 V [45].

We successfully scale up these RFAs for operation at the meso-scale. The V1 designs (Fig. 2.1d-e) employ the same electrode configurations as prior works: alternating positive- and negative-voltage electrodes on one side of a shared substrate, with multiple layers aligning similarly-polarized electrodes on the common side. The new V2 design (Fig. 2.1f) reconfigures the electrodes: rows of positive- and negative-voltage electrodes are aligned on opposite sides of a shared substrate, with multiple layers aligning similarly-polarized electrodes on the common side. In V1, maximal electric fields are directed between adjacent electrodes, so peak voltage, field, and force are all limited by the dielectric strength of air, the inter-electrode spacing (L_G), and any layer misalignment (ΔY). In V2, maximal electric fields are directed through the substrate, so these properties are independent of electrode geometry or layer alignment, and limited only by the dielectric strength of the substrate. Relatedly, the principle failure modes in V1 are shorting between adjacent electrodes (due to manufacturing defects) or layers (due to layer misalignment during set-up or operation) – problematic in dynamic systems; in V2, shorting is only possible through the more resilient substrate.

2.3 Simulation

A 2D numerical simulation of the RFA was developed in MATLAB. The actuator electrostatics (charge distribution, electric potential, and forces) are solved using an explicit finite differences method, with a high-fidelity, non-uniform rectangular mesh and iterated to convergence.

2.3.1   Modeling

Analytical models for two-layer RFA systems were derived by S. He, et al. [41, 43], using conformal transformations to map unit cells of the RFA electrode configuration into a parallel plate electrode configuration for ease of calculation. This transformation, however, assumes unit cells with perfectly aligned, symmetric electrodes – two design requirements not guaranteed when designing these actuators for manufacturing. Agreement between analytical models and numerical simulations of RFAs has been verified [41], thus only numerical simulations are used throughout this dissertation.

The constitutive equations at each node ($\underline{x}_i$) of the simulation, relating electric potential (V), electric field ($\underline{E}$), displacement field (D), and polarization density ($\underline{P}$), are defined as:

$$\underline{E} = -\nabla V \tag{2.1}$$
$$\underline{D} = \varepsilon_r \varepsilon_0 \underline{E} = \varepsilon_0 \underline{E} + \underline{P} \tag{2.2}$$
$$\underline{P} = (\varepsilon - \varepsilon_0)\underline{E}, \text{ with } \varepsilon = \varepsilon_r \varepsilon_0 \tag{2.3}$$

Net charge density (ρ) in the system consists of bound (ρ_b) and free (ρ_f) charge densities, related by:

$$\rho = \rho_f + \rho_b \tag{2.4}$$
$$\rho_f = \nabla \cdot \underline{D} \tag{2.5}$$
$$\rho_b = -\nabla \cdot \underline{P} \tag{2.6}$$

Combining (2.1), (2.2) and (2.5), and applying partial differentials:

$$\nabla \cdot \varepsilon \nabla V = -\rho_f \tag{2.7}$$
$$\varepsilon_y V_y + \varepsilon V_{yy} + \varepsilon_z V_z + \varepsilon V_{zz} = -\rho_f \tag{2.8}$$

The partial derivatives have a finite differences formulation (2nd order, using Lagrangian polynomials for non-uniform grid interpolation) [8] centered at $\underline{x}_i$ of:

$$\begin{aligned} \varepsilon_y &= a_{y,i}\varepsilon(\underline{x}_{i-1}) + b_{y,i}\varepsilon(\underline{x}_i) + c_{y,i}\varepsilon(\underline{x}_{i+1}) \\ V_y &= a_{y,i}V(\underline{x}_{i-1}) + b_{y,i}V(\underline{x}_i) + c_{y,i}V(\underline{x}_{i+1}) \\ V_{yy} &= a_{yy,i}V(\underline{x}_{i-1}) + b_{yy,i}V(\underline{x}_i) + c_{yy,i}V(\underline{x}_{i+1}) \end{aligned} \tag{2.9}$$

with a_i, b_i, c_i defined in [8]. Dirichlet boundary conditions at the electrodes – $V_- = 0$ and $V_+ = V_{Applied}$ – mimic the voltage source powering the actuator. Neumann boundary conditions are defined along the system perimeter – $\partial V/\partial \underline{n} = 0$. Boundaries of the simulation space are at least 5 times the dimensions of the actuator-containing space, to mitigate computation artifacts due to the finite boundaries. Meshing of the simulation space uses a non-uniform rectangular mesh, with highest mesh density at electrode and substrate surfaces to capture the electric fringing field behavior (Fig. 2.2).
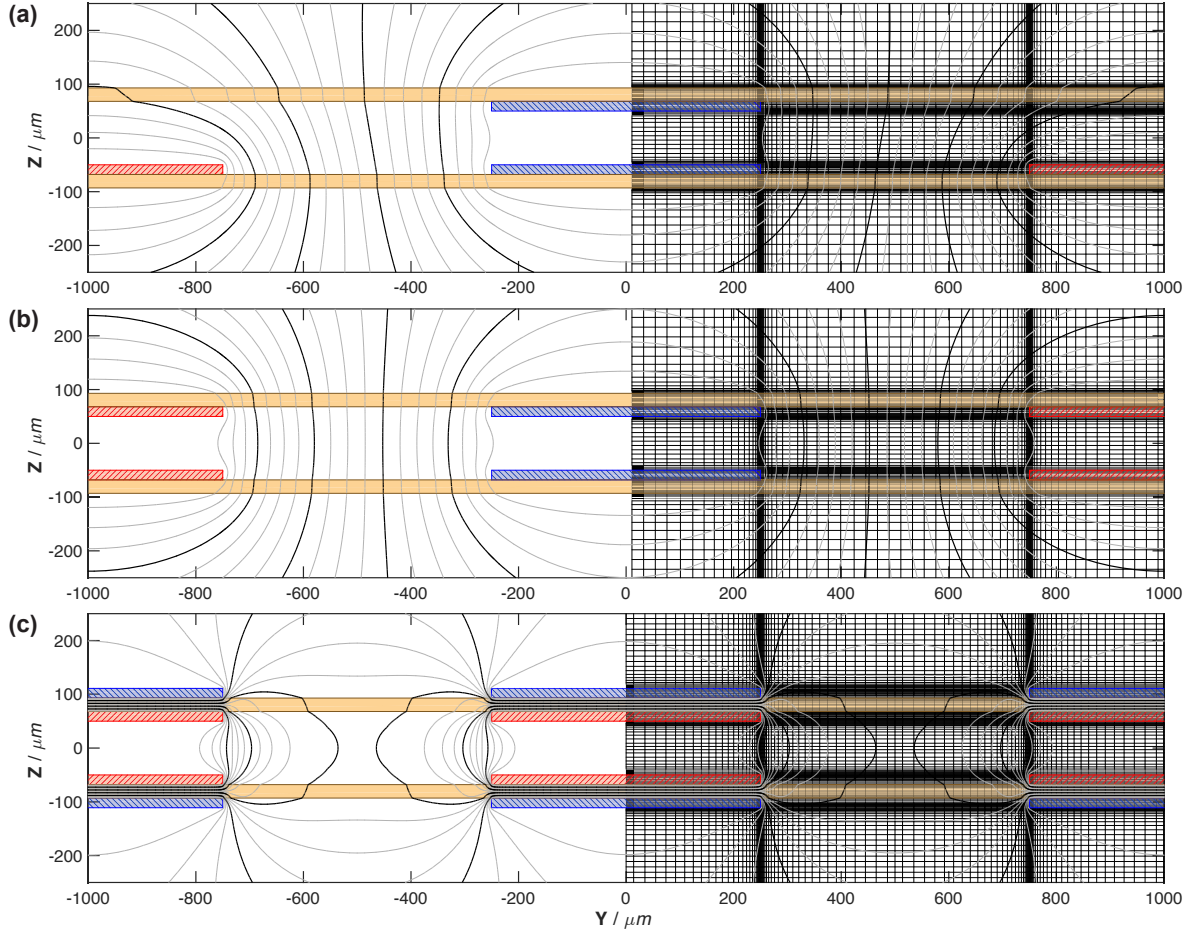
Figure 2.2: Sample mesh grid for simulations of actuator V1-A (a), V1-B (b), and V2 (c) designs. A rectangular mesh is used, with increased density – minimum grid spacing is 1 μm – around material interfaces (electrode / substrate edges).

The voltage distribution in this system is calculated by solving for $V(\underline{x}_i)$ in (2.8) and (2.9) (assuming $\rho_f = 0$ outside electrodes), reimposing boundary conditions, and iterating to convergence. Once V converges, $\underline{E}$, $\underline{P}$, and ρ can be calculated directly.

The electrostatic force on a region of the actuator is:

$$\underline{F} = \iiint_{\mathbb{V}_{\mathbb{E}}} (\rho_f \underline{E}) d\mathbb{V} + \iiint_{\mathbb{V}_{\mathbb{D}}} (\rho_b \underline{E}) d\mathbb{V} + \iint_{\mathbb{S}} (\frac{1}{2}(\sigma_f + \sigma_b) \underline{E} \cdot \hat{n}) d\mathbb{S} \qquad (2.10)$$

with force contributions from the electrode ($\mathbb{V}_{\mathbb{E}}$) and dielectric ($\mathbb{V}_{\mathbb{D}}$) volume interiors and the interfacing surfaces between these regions ($\mathbb{S}$), and with corresponding free (σ_f) and bound (σ_b) surface charge densities. To accurately quantify the net repulsive force between layers – which is roughly 2-orders of magnitude smaller than the attractive body forces between

electrodes on each side of a dielectric substrate – the simulation is assumed to converge when forces on each electrode change by less than 0.05% over 500 iterations.

2.3.2 Results

The simulation results presented in Fig. 2.3 demonstrate that meso-scale actuators (2.5 cm^2 area with 500 μm electrode widths and gaps) can generate mN-range forces with >500 μm gaps at 1 kV potentials. The electric potential distributions for the three actuator designs are shown in Fig. 2.3a-c.

From Fig. 2.3e, the V1 designs have a maximum electric field strength limited by the air dielectric to 5.0·10^6 V/m (for $L_G = 500$ μm) and a corresponding maximum voltage of 2.5 kV [54]. The V2 design uses a polyimide substrate instead of air as the insulating dielectric between oppositely-polarized electrodes, which increases the maximum electric field strength to 236·10^6 V/m (47x increase) and maximum voltage to 5.9 kV (2.3x increase). Note that in the V2 design, the field strength in air around the electrodes can exceed the dielectric strength of air – indeed, fields above $5.0 \cdot 10^6$ V/m extend approximately 50 μm from the edges of electrodes at 1000 V. This can cause localized air ionization – without breakdown – as all shorting paths between positive / negative electrodes must still pass through the more robust polyimide substrate.

From Fig. 2.3f, the new V2 electrode design generates consistently greater electrostatic pressures and forces than comparable V1-A / B designs. For actuators with equivalent configurations (L_G, L_P, $L_N = 500$ μm, $H = 50$ μm, 2.5 cm^2 actuator area) and operating at $V = 1$ kV, V2 produces estimated forces of 13.1 mN, compared to 0.934 mN for V1-B (14x decrease) and 0.249 mN for V1-A (53x decrease). Operating at their respective breakdown voltages, V2 generates forces of 455 mN, compared to 5.95 mN for V1-B (76x decrease) and 1.59 mN for V1-A (286x decrease). Interestingly, above certain inter-layer heights, V1-A and V1-B actuators transition to a net attractive force between layers, while V2 does not exhibit this behavior and always produces a net repulsive force. Finally, the significance of the fringing fields is highlighted in Fig. 2.3d, where 90% of the actuator's force is generated by the 20 μm of electrode area nearest each edge – 4% of total actuator area. Future fabricated actuators can thus generate greater electrostatic pressure via increasing electrode density (reduced electrode width (L_P, L_N) and pitch) up to manufacturing limits.

2.4 Fabrication

A flex-circuit manufacturing process is used to produce planar repulsive-force electrostatic actuators patterned with the V1-A / B and V2 electrode designs introduced in Section 2.3. The fabrication process is illustrated in Fig. 2.4; fabricated actuator layers are shown in Fig. 2.1 and a magnified view of V2 is provided in Fig. 2.5.
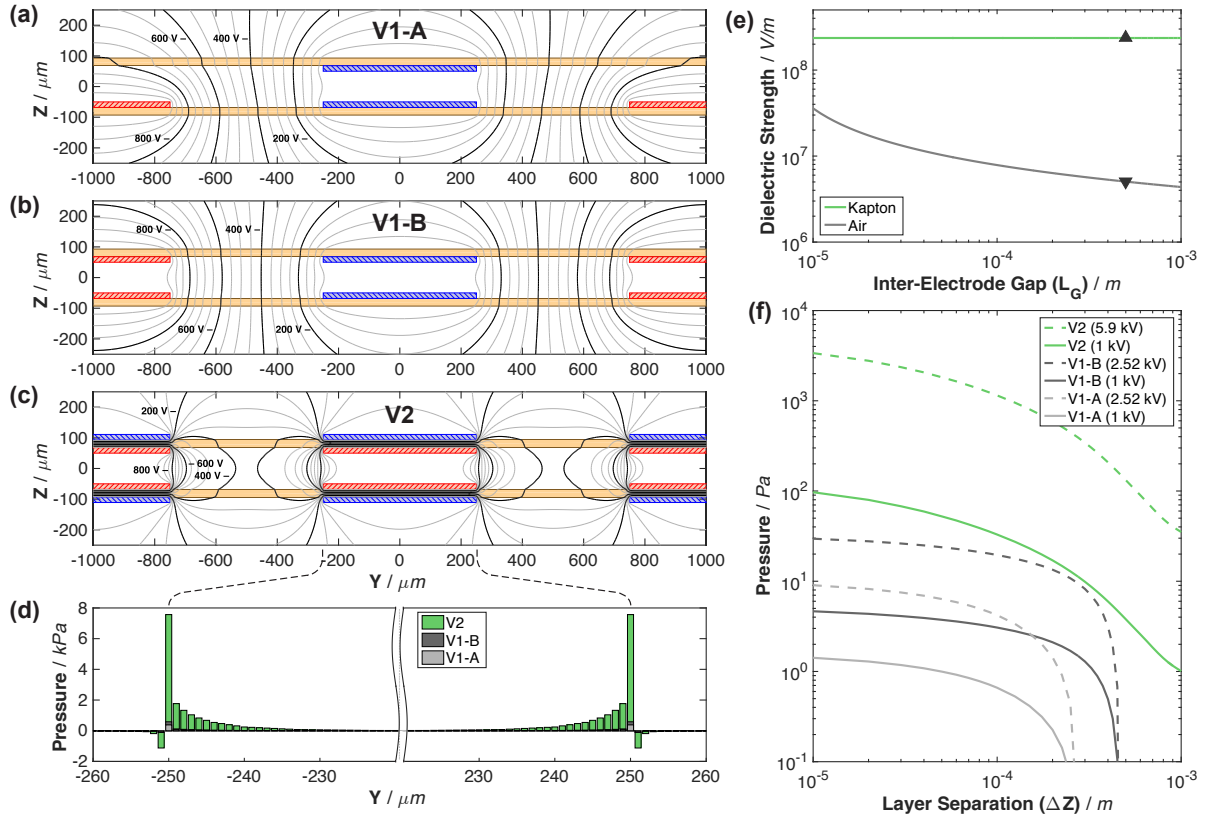
Figure 2.3: Simulation results for the repulsive-force electrostatic actuator. Electrostatic potential (V) for designs V1-A (a), V1-B (b), and V2 (c), with electrodes operating at $0\ V$ (blue) / $1000\ V$ (red) and dielectric substrate (orange). (d) Net electrostatic pressure across the top layer of each design, focusing on the center electrode and with $1\ \mu m$ mesh size. (e) Dielectric strength at breakdown versus inter-electrode gap (L_G) in polyimide [23, 24] and air [54, 106]. Manufactured V1-A / B actuators (with $L_G = 500\ \mu m$) are limited by air breakdown at $5.0 \cdot 10^6\ V/m$ (▼); V2 actuators are limited by polyimide breakdown at $2.4 \cdot 10^8\ V/m$ (▲). Note that in V2 actuators, the field strength around the electrodes can exceed the dielectric strength of air without breakdown, as all shorting paths between positive / negative electrodes must pass through the more robust polyimide substrate. (f) Net electrostatic pressure produced by a complete actuator versus layer separation (ΔZ) in each design. Operating voltage (shown in legend) is either $1\ kV$ or maximum voltage corresponding to predicted electrostatic breakdown field strength from (e).

2.4.1 Design

RFA layers are fabricated out of Pyralux (DuPont, AP 8515E) – a double-sided laminate composed of copper foil (18 μm) electro-deposited on a polyimide substrate (25 μm) that is designed for high-voltage and flex-circuit applications.

The polyimide substrate provides resilience to electrical breakdown (236 V/um dielectric strength at 25 μm thick), operation up to 6 kV, low dielectric losses (dissipation factor under 0.003), trivial mechanical creep at sub-MPa loading, and high folding endurance (285,000 cycles) [23], although time-to-failure decreases with faster charging / discharging rates and higher peak-to-peak voltages [26, 65]. The Cu foil is ductile, has good flexural endurance (>6000 cycles), and is resistant to delamination (1.6 N/mm peel strength) [24]. Thus, the actuators are mechanically resilient to the physical impulses (drops, collisions, etc.) that would be common during use in a mobile robot platform.

2.4.2 Process

Actuator layers are fabricated using a positive wet etching process, shown in Fig. 2.4. Device layers are fabricated from Pyralux (DuPont, Pyralux AP 8515E), and mask layers consist of polyimide sheets (American Durafilm, Kapton 100HN (25 μm)) with thermal adhesive (GBC, Octavia Hot Mount Adhesive) laminated onto one side. Mask layers are secured to both sides of a device layer. The actuator electrode pattern is cut into the mask layers (positive mask) and the actuator substrate extents are cut through all mask / device layers using a UV laser cutter (PhotoMachining Inc., 355 nm). Excess mask and substrate material are removed manually. The mask / device layers are run through a laminator to set the thermal adhesive and provide an etch barrier. Any exposed thermal adhesive is removed with acetone (Fischer Scientific). The device layer is selectively etched with ferric chloride (MG Chemicals, FeCl$_3$) to pattern the Cu electrodes. Mask layers are released with acetone and the device layer is cleaned with water. Production time is approximately 4 hours per sheet of actuator layers.

Final assembly of the actuator layers can be performed multiple ways: laminating the layers to substrates (Section 2.5.1), attaching the layers to a flexible suspension (Section 2.5.2), or folding pre-connected layers over one another (Section 2.6). In each instance, power wires are directly soldered to electrode pads on each layer, and visual alignment marks (+) at the actuator corners are used to ensure precise alignment between layers.

2.4.3 Process Advantages

From a manufacturing perspective, this thin-film process enables cheaper fabrication of actuator layers with greater surface area, and provides significant design freedoms over conventional MEMS processes. The fabrication uses 2-3 patterning steps and 1 etch step to fabricate batches of complete V1 or V2 actuator layers. Actuators with +2 layers (see Chap. 3) can be assembled by stacking discrete layers or folding up a sheet of connected units. Within each layer, the substrate provides all necessary mechanical structure and electrical insula-
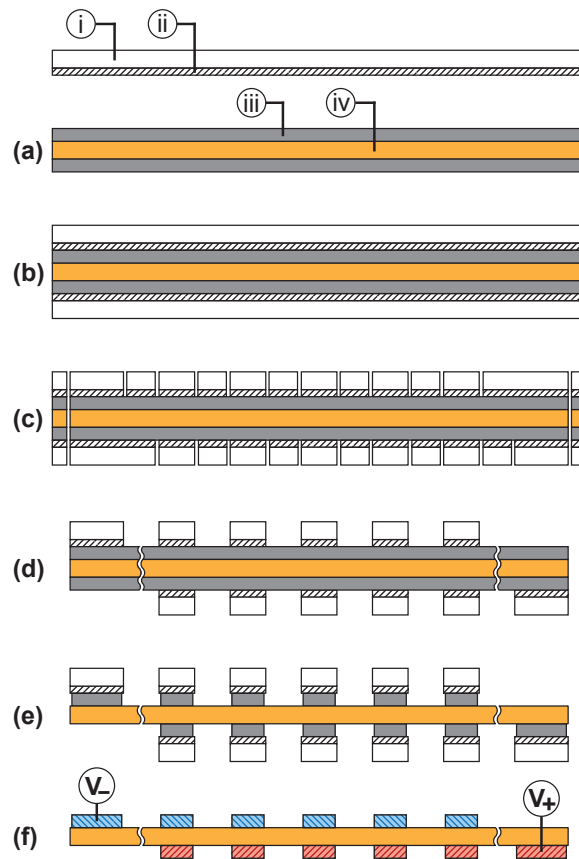
Figure 2.4: Fabrication process for each actuator layer: (a) Preparation of two mask layers – polyimide film (i) with a thermal adhesive (ii) laminate – and a Pyralux® device layer – a double-sided laminate of Cu-foil (iii) on a polyimide substrate (iv). (b) Placement of mask layers on the device layer. (c) Cutting (via laser cutter) the electrode patterns into the mask layers and actuator extents through the device layer. (d) Removal of excess mask and substrate. (e) Etching the Cu. (f) Release of mask layers and soldering of power lines.
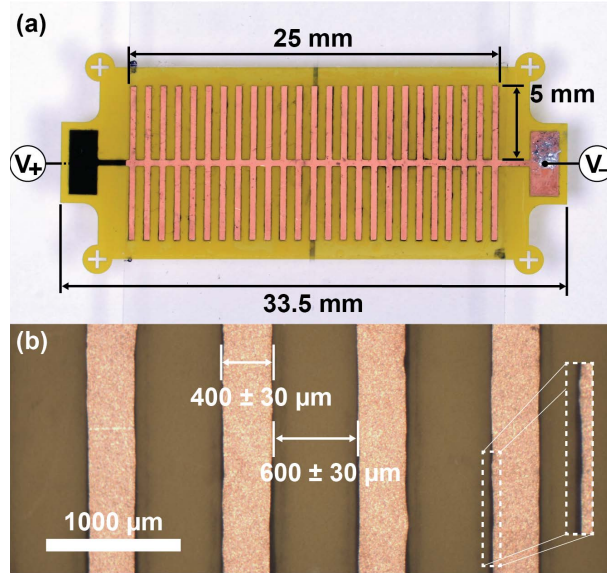
Figure 2.5: Photo of fabricated actuator layer with two-sided V2 electrode pattern (a), and magnified view of electrodes (b). Dashed region highlights minor variation between widths of front-side (copper) and back-side (dark region) electrodes; over-etching results in L_P, $L_N \approx 400 \ \mu m$. Also note visual alignment marks (+) at actuator corners.

tion for the positive / negative voltage traces (no extra laminates required). For each device, interface leads can be directly soldered to electrodes without compromising the substrate (no wire-bonder needed). MEMS processes, in comparison, require numerous deposition, masking, and etching steps to produce a single spring-suspended device layer with routing for positive / negative lines on a floating dielectric. As a result, the V1-A design is simple to produce with PolyMUMPS, while the V1-B design is more complex and our new V2 design is entirely incompatible.

2.5 Characterization

2.5.1 Force Measurements

Blocked force measurements of the RFAs were performed using the experimental set-up shown in Fig. 2.6. Alignment sensitivity of the actuator layers is measured by translating the two layers relative to one another in discrete X-, Y-, and Z-axis offsets (ΔX, ΔY, ΔZ), as shown in Fig. 2.8.

2.5.1.1 Experimental

Two actuator layers are laminated to individual glass microscope slides (Fischer Scientific, 75 x 25 x 1 mm) with thermal adhesive. One glass slide is mounted on a stack of two linear
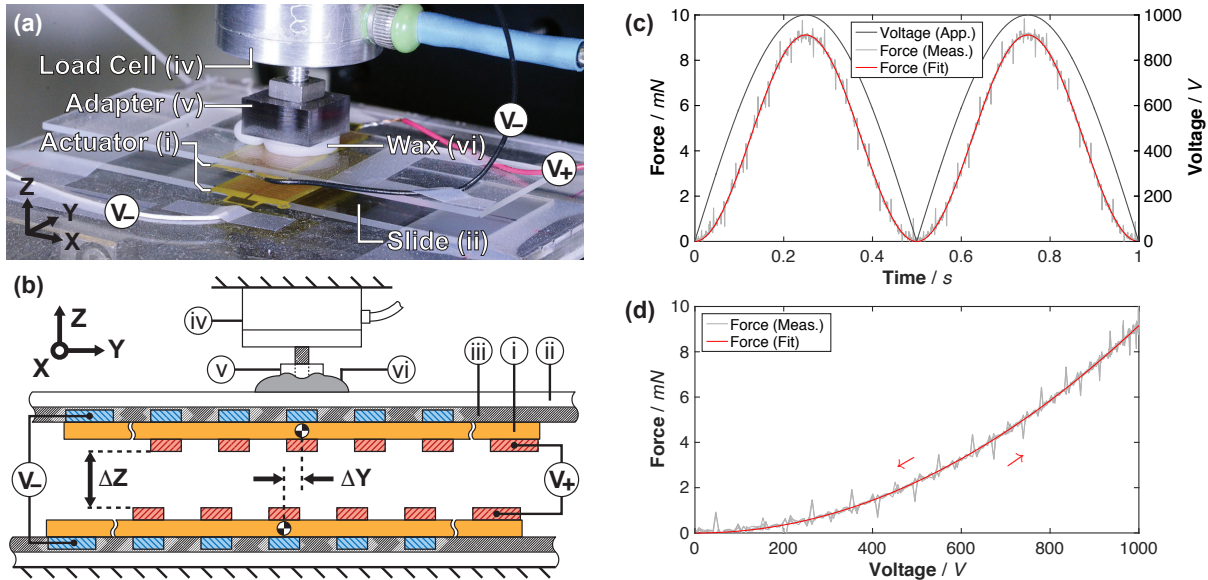
Figure 2.6: Testing setup for blocked force characterization (a) with mechanical diagram (b) (electrical diagram in Fig. 2.7). Two actuator layers (i) are bonded to glass slides (ii) with thermal adhesive (iii). The bottom layer sits on a multi-DoF stage; the top layer connects to a load cell (iv) via an adapter (v) and wax (vi), and is aligned parallel to the bottom layer. (c-d) Force characterization at ΔX, $\Delta Y = 0 \ \mu m$ and $\Delta Z = 50 \ \mu m$. Applied voltage is the square-root of a sinusoid at 2 Hz and 1000 V peak-to-peak. (c) Force (measured and sinusoidal fit) and applied voltage versus time; (d) force (measured and quadratic fit) versus voltage, where fit has $R^2 = 0.9992$ (for 10 s / 20 cycles of data). Force data is unfiltered, and periodic peaks are 60 Hz noise.

stages (Newport, 423 Series) to provide X- / Y-axis offsets, with the actuator layer face-up. A single-axis load cell (Omega, LCFA-50G) is mounted to a third linear stage providing Z-axis offsets, suspended over the other stages, and an interface block is secured to the end of the load cell input shaft. The second glass slide, with actuator face-down, is placed and aligned on top of the first actuator layer. Liquid paraffin wax is poured on the top side of the glass slide, and the load cell with interface block is lowered into the liquid wax and allowed to solidify. The wax provides mechanical connection between the actuator and load cell while guaranteeing the two actuator layers are parallel. The top actuator layer can then be raised away from the bottom layer.

A LabView interface controls the experiment (Fig. 2.7). A low-voltage drive signal (V_{Drive}) – in this case a 2 Hz, 0–10 V square-root of sinusoid waveform – is generated by a DAQ (National Instruments, NI USB 6341) and supplied to a high-voltage amplifier (Trek, PZD700 Piezo Driver / Amplifier). The amplifier provides 100x gain to V_{Drive}, and this signal then powers the actuator. Voltage (V_{VP}) and Current (V_{CP}) probes provide measurement of the actuator's electrical properties during testing. The load cell – a full
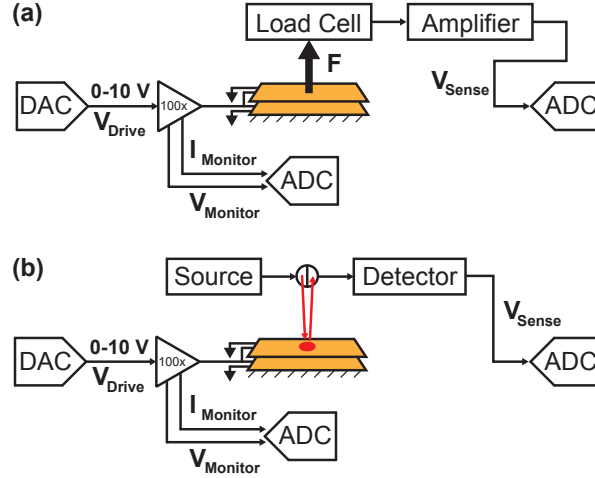
Figure 2.7: Electrical diagrams for measuring blocked force (a) and free displacement (b). V_{Drive} is amplified using a Trek Piezo Driver / Amplifier. Forces are measured with a single-axis load cell (Omega, LCFA-50G) and strain gauge amplifier (Techkor Instrumentation, MEPTS-9000). Displacements are measured using custom optical sensors [109].

Wheatstone bridge strain gauge circuit – measures the electrostatic normal force applied to the top actuator layer and a strain gauge amplifier (Techkor Instrumentation, MEPTS-9000) boosts this signal (V_{Sense}) by 100x. V_{Sense} is then logged by the DAQ.

2.5.1.2 Results

Maximum repulsive force (9.03 mN) is generated by a two-layer V2 actuator in a ($\Delta X, \Delta Y = 0 \ \mu m$, $\Delta Z = 50 \ \mu m$) configuration at 1000 V. Recorded actuator behavior in this configuration is provided in Fig. 2.6c-d, and shows the quadratic relationship between the applied voltage and blocked force. Operation of a well-aligned (in the X / Y-plane) actuator will apply purely normal (Z-axis) force to the top layer. Repulsive force increases with the inverse square of Z-axis offsets (Fig. 2.8a), to a maximum of 9.03 mN (at $\Delta Z = 50 \ \mu m$), and has good agreement with the simulated forces. Closer than this ($\Delta Z < 50 \ \mu m$), electrode imperfections produce non-uniformities in the electric field that reduce the repulsive force. Upon contact ($\Delta Z = 0 \ \mu m$), the internal (V_+) electrodes act as a single conductive body, which redistributes the surface charge and generates a net attractive force between the actuator layers (Fig. 2.8a, Inset).

Y-axis offsets (Fig. 2.8b, $\Delta Y > 0 \ \mu m$) between the layers reduce the repulsive normal force, and sufficient lateral offsets can actually transition the net repulsive force to an attractive force. The ΔY transition from repulsive to attractive force varies with ΔZ: $\Delta Y_{Trans.} = 92, 128, 178, 275 \ \mu m$ (9.2–27.5% phase offset, given the 1 mm pitch electrodes) for $\Delta Z = 50, 100, 200, 500 \ \mu m$, respectively, so closely spaced layers tolerate less ΔY misalignment. Maximum attractive force occurs at $\Delta Y = 500 \ \mu m$ (50% phase offset) and
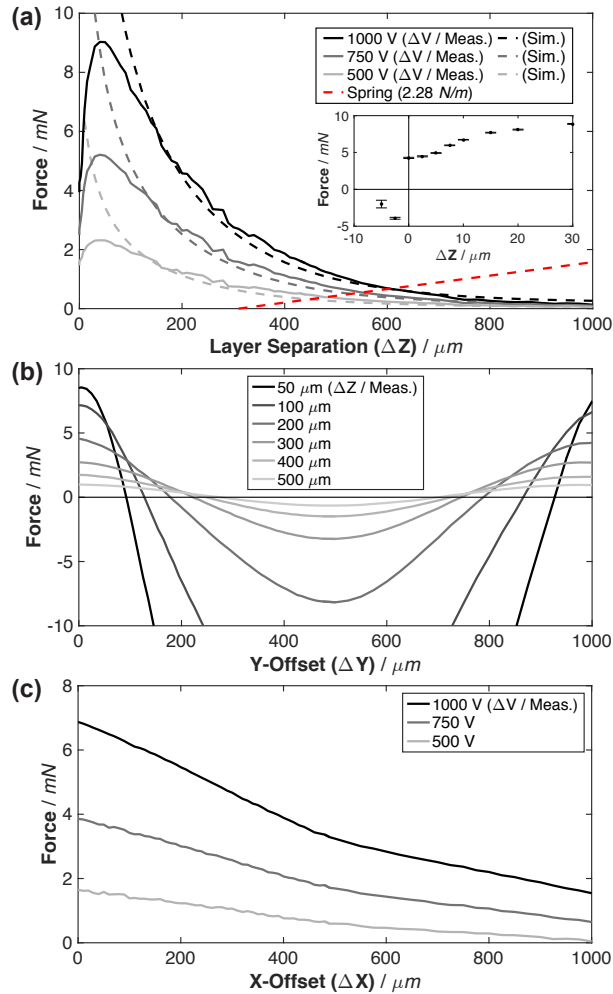
Figure 2.8: Repulsive normal force characterization for the RFA (V2 pattern) at a range of ΔX, ΔY, and ΔZ offsets, with square-root of sinusoid inputs at 2 Hz / 1000 V peak-to-peak. (a) Measured (Meas.) and simulated (Sim.) force versus ΔZ (ΔX, $\Delta Y = 0$ μm, $\bar{\sigma} = 0.042$ mN) at three voltages, and suspension spring force ($k_S = 2.28$ N/m). Inset figure shows near- / in-contact behavior, with mechanical contact force removed. (b) Force versus Y-axis offsets ($\Delta Z = 50$–500 μm, $\Delta X = 0$ μm, $\bar{\sigma} = 0.127$ mN). (c) Force versus X-axis offsets ($\Delta Z = 100$ μm, $\Delta Y = 0$ μm, $\bar{\sigma} = 0.045$ mN).

maximum repulsive force occurs at 0% / 100% phase offsets. A Y-axis shear force is also produced during the transition from pure repulsive to pure attractive modes. This behavior demonstrates the need to assemble RFAs with precise lateral alignment to ensure maximum repulsive forces are generated (and attractive forces are avoided).

X-axis offsets (Fig. 2.8c, $\Delta X > 0$ μm) reduce the overlap between electrode traces on each layer and proportionally reduce the repulsive normal force. The slope changes at $\Delta X = 500$ μm when the centerline trace no longer overlaps (see Fig. 2.5). Electrode traces remain well-aligned with respect to the Y-axis, avoiding a transition from repulsive to attractive force.

2.5.2   Displacement Measurements

Free displacement measurements of the RFAs were performed using the set-up shown in Fig. 2.9, with results in Fig. 2.11. The actuator top layer is suspended on a parallel 4-bar suspension (Fig. 2.10) that provides orientation, Z-axis compliance for large displacements, and X- / Y-axis stiffness to maintain alignment. The actuator layers have an initial offset of $\Delta Z_0 = 310$ μm to prevent operation near $\Delta Z = 50$ μm, where repulsive force markedly decreases (see Fig. 2.8).

2.5.2.1   Experimental

The actuator bottom layer is laminated onto a glass slide and secured to a 1-DoF rotational stage (Newport, MT-RS Series). The actuator top layer is suspended from a 3D-printed mount (FormLabs, Form 2) on a 3-DoF linear stage (Newport, M-461 Series) to align the top layer over the bottom layer. The spring suspension (Fig. 2.10) consists of four sets of cantilevered beams – compliant in Z, stiff in X / Y – laser-cut from PET film (American Durafilm, 25 μm) as a single unit and adhered to the top layer with thermal adhesive. Two fiberoptic optical sensors – developed by E. Steltz [109] – provide displacement measurements of the actuator's top layer, and distinguish between Z-axis translational and X-axis rotational or flexing modes. The sensors are mounted parallel to one another in a 3D-printed clamp on an independent 3-DoF stage; sensor light is reflected off of matte paper sheets adhered onto the actuator top layer. The actuator is controlled from LabView, driven by a square-root of sinusoid signal supplied from the high-voltage amplifier, and monitored with voltage and current probes. The displacement is measured by the fiberoptic sensors and logged by the DAQ.

For testing at different pressures, the full testing set-up is placed in a vacuum chamber (Abbess Instruments) and pumped down to the desired pressure using a vacuum pump (Pittsburgh Automotive, Two Stage Vacuum Pump). Vacuum feedthroughs for electricity and fiber-optic cables are used to drive the actuator and measure displacements.
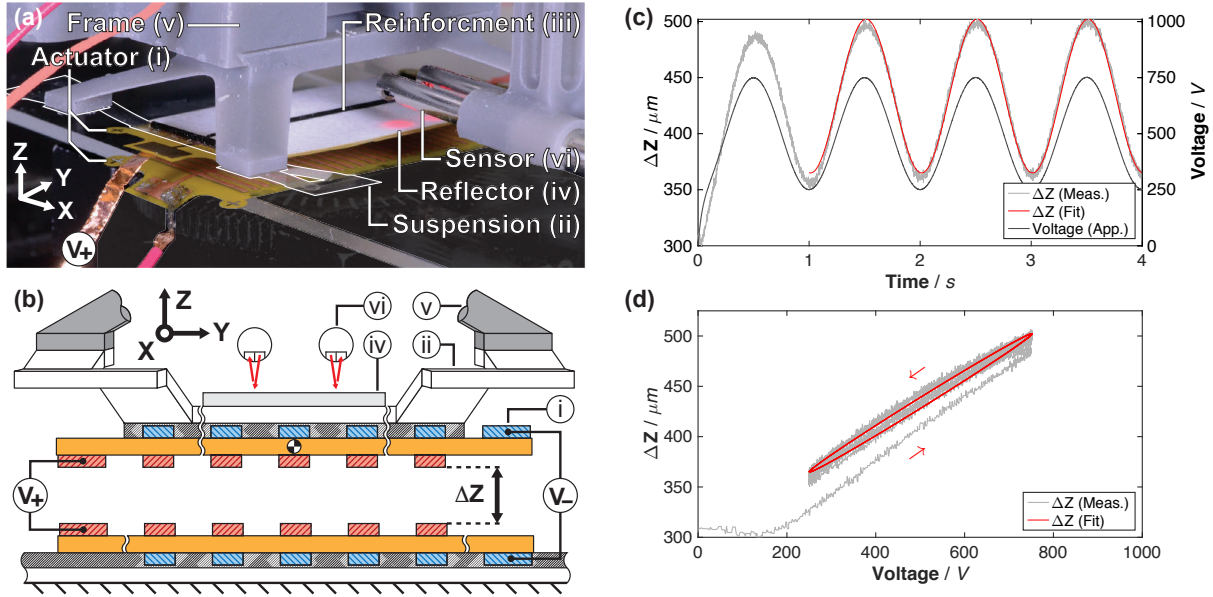
Figure 2.9: Testing setup for free displacement characterization (a) with mechanical diagram (b) (electrical diagram in Fig. 2.7). Of the two actuator layers (i), the bottom layer is bonded to a glass slide, and the top layer is reinforced with carbon fiber rods (iii) and connected to a 3D-printed frame (v) via a film cantilever spring suspension (ii, outlined in white). Displacement is monitored by optical emitter / detector sensors (vi) at two locations, reflected off a paper reflector (iv). Power is supplied by copper foil wires (V_+/V_-). (c-d) Displacement characterization with an applied sinusoid input voltage at 1 Hz / 500 ± 250 V peak-to-peak. (c) Measured actuator ΔZ and actuator voltage versus time, with fit shown; (d) measured actuator ΔZ versus actuator voltage, with fit shown.

2.5.2.2 Results

The actuator's measured displacement at low-frequency operation is shown in Fig. 2.9. A sinusoidal voltage (500 V bias and ± 250 V amplitude) is applied to generate sinusoidal displacements of 132 μm peak-to-peak, after initial transients subside. Applying 500 ± 500 V generates larger 242 μm peak-to-peak displacements (Fig. 2.12), at the cost of increased nonlinear behavior and hysteresis – likely caused by viscoelastic behavior in the PET suspension or residual charge in the polyimide substrate.

The actuator's frequency-dependent displacement, magnitude, and phase behavior is shown in Fig. 2.11, and exhibits second-order behavior as modeled in Fig. 2.13. Displacement is measured peak-to-peak during stable operation after transients subside. The actuator has a -3 dB bandwidth of 43 Hz. A stable Z-axis resonant mode at $f_0 = 29$ Hz has a peak displacement of $\Delta Z_{f_0} = 511$ μm and quality factor of $Q = 1.59$ (17.3–35.5 Hz).
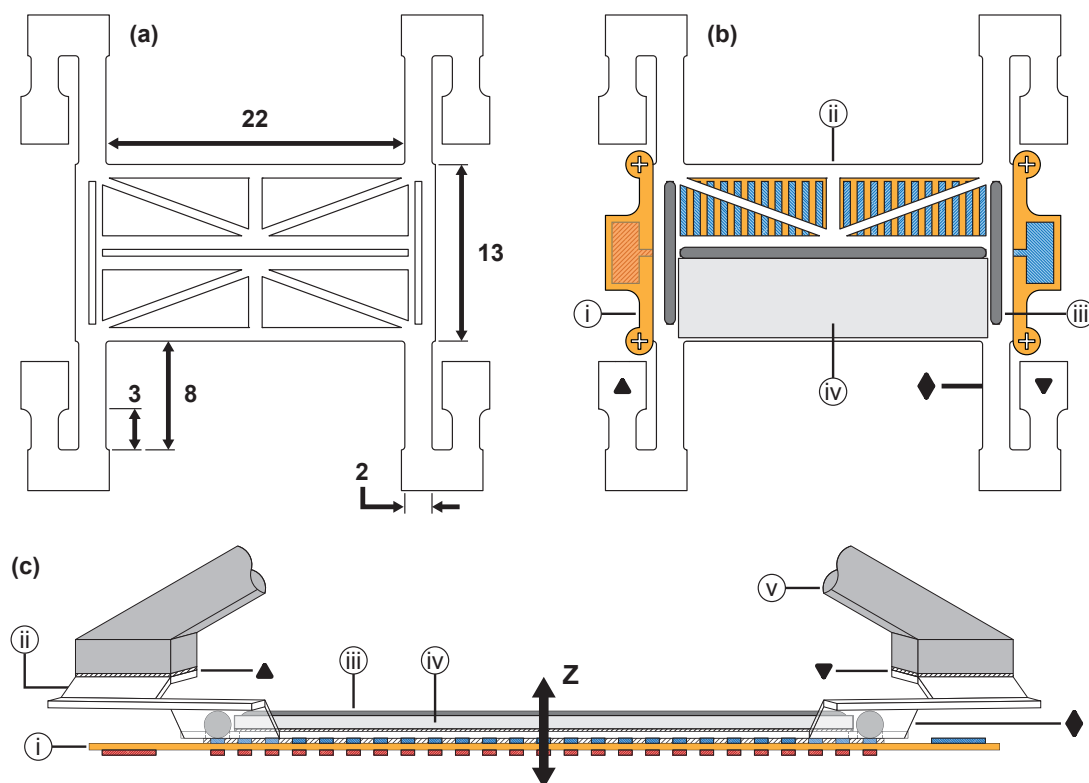
Figure 2.10: Suspension design and assembly for the top actuator layer in the free displacement measurement experiment. (a) Design for the parallel four-bar suspension, with four folded spring elements (units in mm). (b) Top view of assembly containing the actuator layer (i) adhered to the film suspension (ii), carbon fiber rod reinforcement (iii), and an optical reflector (iv). The suspension is cut from a single PET film (25 μm thick). The carbon fiber rods fit into pre-cut slots in the suspension aligned on top of existing electrode traces (to prevent modifying the electrical field distribution). (c) Cross-section view of actuator assembly mounted to the 3D-printed frame (v). Markers (▲ / ▼ / ♦) show suspension alignment between top and side view. Suspension allows Z-axis translation of the actuator layer.
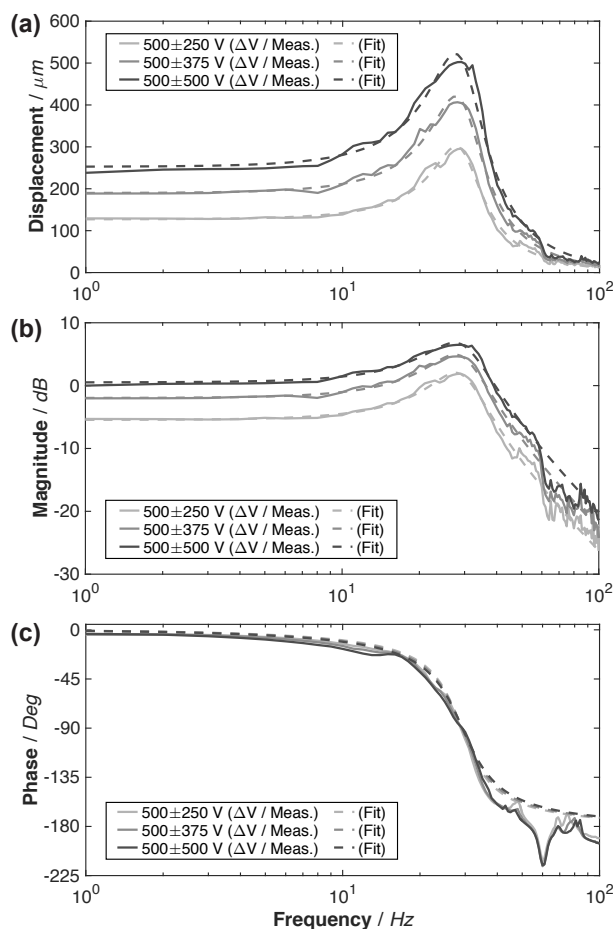
Figure 2.11: Actuator displacement (peak-to-peak) (a), magnitude (b), and phase (c) versus frequency. Applied sinusoid input voltage at 1–100 Hz and 500 ± 250 / 375 / 500 V peak-to-peak. Data is fit with second-order linear systems. The actuator has stable 240–260 μm peak-to-peak displacements at sub-10 Hz frequencies, 511 μm displacements at 29 Hz resonance, and a 43 Hz open-loop bandwidth. The resonant peak has a quality factor of 1.59 (-3 dB from peak at 17.3 and 35.5 Hz).
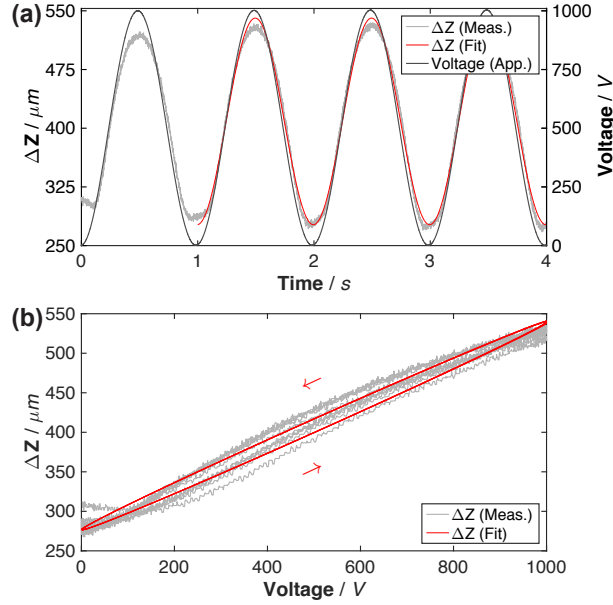
Figure 2.12: Displacement characterization with an applied sinusoid input voltage at $1\ Hz$ / $500 \pm 500\ V$ peak-to-peak. (a) Actuator ΔZ (measured and sinusoid fit) and actuator voltage versus time; (b) actuator ΔZ (measured and sinusoid fit) versus actuator voltage. Deviations from pure sinusoidal displacement are visible around peaks.

From the resonant behavior:

$$Q = \omega_0/\Delta\omega \tag{2.11}$$

$$\omega_0 = \sqrt{(k_A + k_S)/m_A} \tag{2.12}$$

$$b_S = (m_A\omega_0)/Q \tag{2.13}$$

Given the measured mass ($m_A = 135\ mg$) and suspension stiffness ($k_S = 2.28\ N/m$), the calculated net stiffness is $4.5\ N/m$ ($k_A + k_S$) and the parallel effective electrostatic spring stiffness is $2.2\ N/m$ (k_A). This agrees with the direct estimation of k_A from Fig. 2.8a:

$$k_A = dF/dZ \approx \Delta F/\Delta Z = 2.36\ N/m \tag{2.14}$$

around the average operating point of $\Delta Z = 425\ \mu m$ and $500\ V$; the effect of k_S is also plotted in Fig. 2.8a. Damping ($b_S = 0.0155\ Ns/m$) is generated predominantly by the structure as opposed to air, as seen in Fig. 2.14. X-axis rotational modes are predicted at $0.34\ Hz$ and $5.8\ kHz$, and an X-axis bending mode predicted at $51\ Hz$ is increased to above $200\ Hz$ with stiffeners (reflectors and the carbon fiber reinforcing rods).
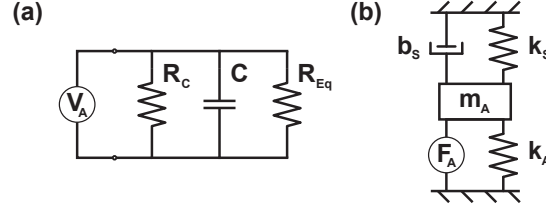
Figure 2.13: Electrical (a) and mechanical (b) models for the actuator. Electrical components include: voltage source (V_A) and actuator capacitance ($C = 840\ pF$), leakage resistance ($R_C = 350\ G\Omega$), and equivalent resistance ($R_{Eq} = 3.5\ G\Omega$, at resonance) due to mechanical load. At resonance, $R_{Eq} = b_S/T^2$, with the linear approximation of $T = \Delta F/\Delta V = 2.11 \cdot 10^{-6}\ N/V$ (electro-mechanical transformation ratio) determined using $\pm 250\ V$ deviations around the $500\ V$ and $\Delta Z = 425\ \mu m$ operating point in Fig. 2.8a. Mechanical components include: actuator force source (F_A), actuator electrostatic spring ($k_A = 2.2\ N/m$), actuator mass ($m_A = 0.135\ g$), suspension spring ($k_S = 2.28\ N/m$), and suspension damping ($b_S = 0.0155\ Ns/m$).

2.5.3 Internal Power Measurements

Mechanical power is calculated from the actuator's resonant behavior. Assuming a second-order system:

$$P = \frac{F^2}{2b_S}, \text{ with } F = (k_S + k_A) \cdot \Delta Z_{f_{DC}} \tag{2.15}$$

ΔZ at $f_{DC} = 1\ Hz$ is provided in Fig. 2.11; the stiffnesses (k_A, k_S) and damping (b_S) are provided in Fig. 2.13. Calculated mechanical power for the actuator at resonance is 38.0 μW.

Electrical power is calculated directly from the voltage and current probe measurements. The actuator behaves electrically as a non-ideal capacitor (Fig. 2.15) – with parallel capacitance ($C = 840\ pF$), leak resistance ($R_C = 350\ G\Omega$), and equivalent resistance ($R_{Eq} = 3.5\ G\Omega$, at resonance) due to mechanical work – and is modeled in Fig. 2.13. Electrical input power increases quadratically (1.78 mW at 1 Hz to 52.3 mW at 29 Hz resonance) and current increases linearly (2.73 μA to 75.5 μA) with frequency (Fig. 2.16), using a $500 \pm 500\ V$ sinusoidal driving voltage.

The actuator has an electromechanical coupling factor of 1.8% (1 Hz) – 3.7% (29 Hz), based on:

$$\kappa = \sqrt{\frac{W_{Mech.}}{W_{Ele.}}} = \sqrt{\frac{(k_A + k_S)\Delta Z^2}{C\Delta V^2}} \tag{2.16}$$

The low coupling factor results from the actuator's large parallel plate capacitance between oppositely-charged electrodes in the V2 design.
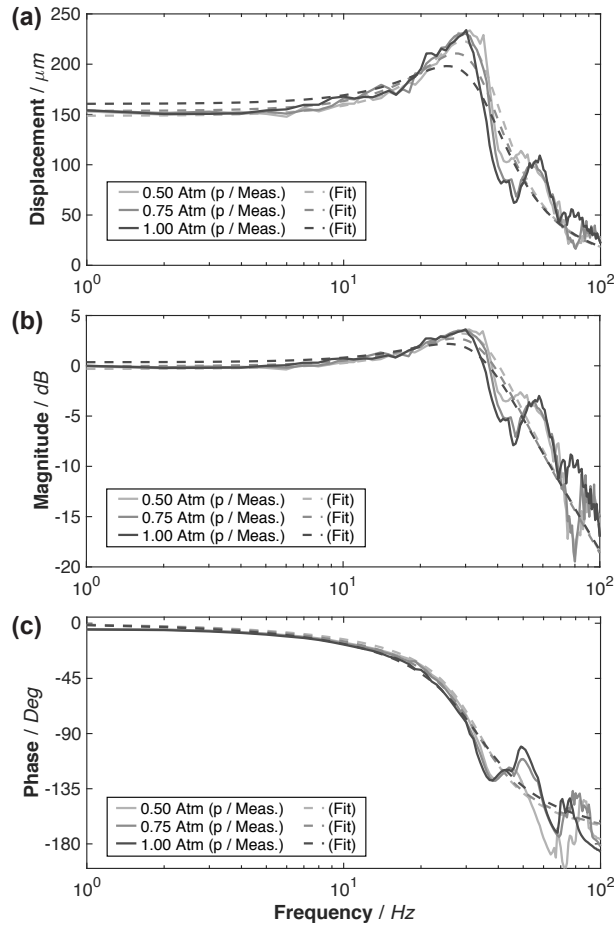
Figure 2.14: Actuator displacement (peak-to-peak) (a), magnitude (b), and phase (c) versus frequency, at three environmental pressures (0.50, 0.75, and 1.00 Atm). Actuator is driven by an applied sinusoid input voltage at 1–100 Hz and 500 ± 250 V peak-to-peak, and layers have an initial gap of $\Delta Z = 114$ μm. Data is fit with 2-pole linear system model. Air damping has minimal effect on actuator operation: peak displacement is a near-constant 230–234 μm at 30 Hz across the three pressures (increased amplitude would be expected at lower pressures).
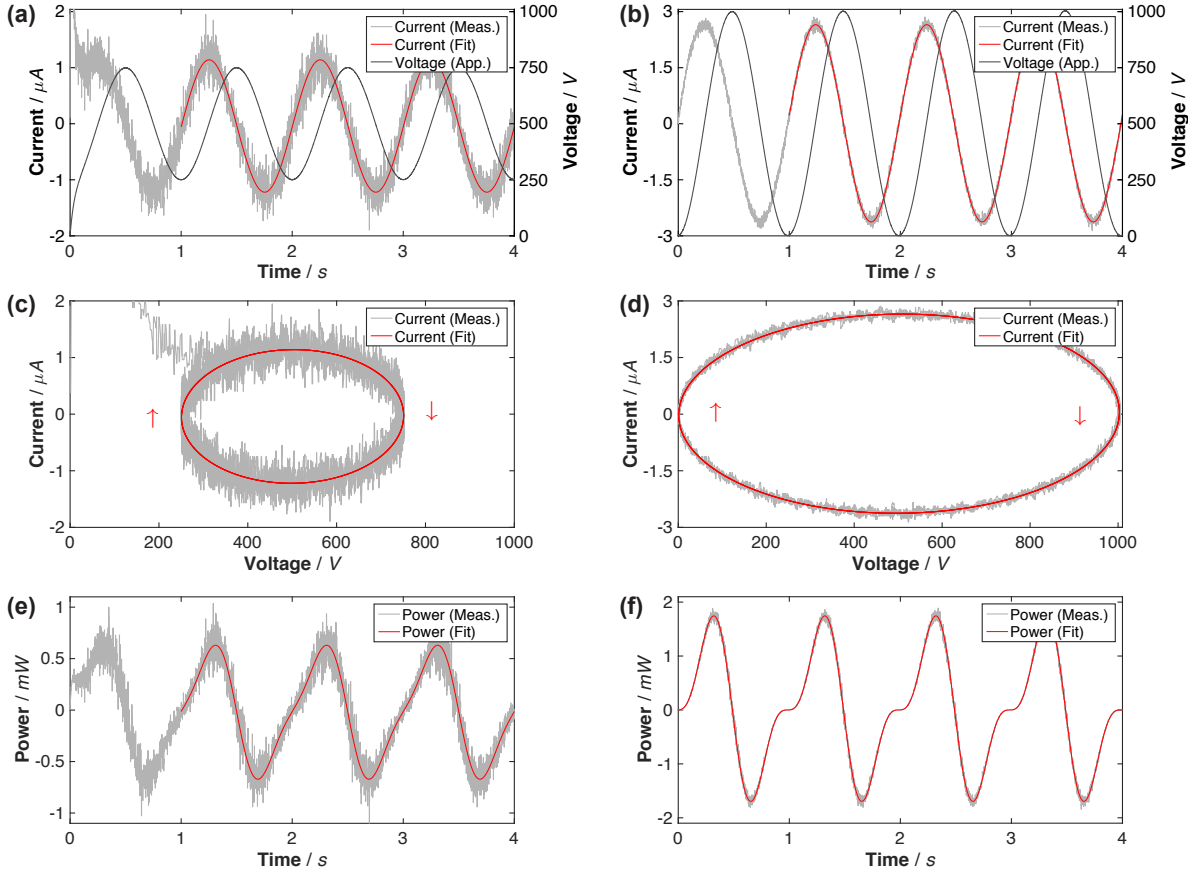
Figure 2.15: Actuator applied voltage, measured current, and calculated input electrical power versus time, recorded during operation of displacement experiments. Applied voltage is a sinusoid input at $1\ Hz\ /\ 500 \pm 250\ V$ peak-to-peak (a / c / e) and $1\ Hz\ /\ 500 \pm 500\ V$ peak-to-peak (b / d / f). (a / b) Current (measured and sinusoid fit) and voltage versus time; (c / d) current (measured and sinusoid fit) versus voltage; (e / f) calculated input power versus time, with fit. The actuator's measured electrical behavior is consistent with an $840\ pF$ capacitance; current due to parallel resistances ($350\ G\Omega$ leakage and $3.5\ G\Omega$ equivalent resistance) are below the measurement resolution. The I-V plot is elliptical, and current leads voltage by 89.1–89.3°, based on fits in (a / b). Resistance was measured directly with an electrometer (Keithley Instruments, 610C). Note that the initial ramp up in applied voltage from $0\ V$ to the $500 \pm 250\ V$ sinusoid in (a / c) results in a current spike to $4.7\ \mu A$ that settles to steady state within $0.15\ s$. (a / c / e) is unfiltered data; (b / d / f) has a 3-point moving median filter applied.
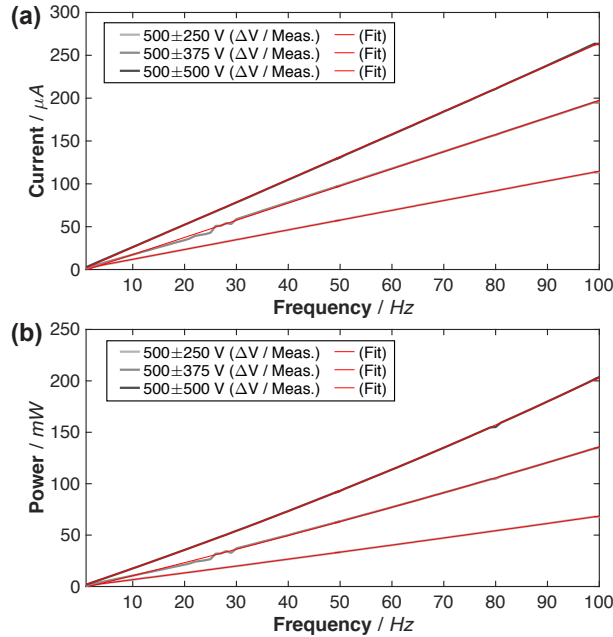
Figure 2.16: Actuator electrical performance: (a) peak current versus frequency, with linear fit; (b) peak power versus frequency, with quadratic fit. Applied voltage is a sinusoid input, at 1–100 Hz and 500 ± 250 / 375 / 500 V peak-to-peak. Current consumption is expected to be linear (with frequency) in a non-ideal capacitor model, with slope proportional to capacitance (840 pF) and vertical offset due to parallel resistances (below the measurement noise and resolution). Power consumption is expected to be quadratic (with frequency) in a non-ideal capacitor model.

An individual 1-DoF translational actuator was tested for >700,000 cycles during the Sec. 2.5.2 and 2.5.3 experiments – characterization of the actuator's displacement dependence on input voltage, input frequency, and environmental pressure. No degradation of the actuator performance was observable at the end of testing, but note that no continuous experiment has been performed thus far to measure long-term changes to actuator operation or device life.

2.6 Application Example

We demonstrate a low-cost, 1-DOF micro-mirror driven by a flexible actuator for beam-steering applications (Fig. 2.17), such as laser mapping (on mobile robots) and laser engraving / marking. The micro-mirror system is self-contained (no extra transmission required), compact (45 x 15 mm, with 20 x 10 mm of active actuator area), and lightweight (290 mg, including a 14 mg / 3 x 6 mm mirror).

The micro-mirror system consists of a 2-layer rotational RFA: the electrodes are fabricated
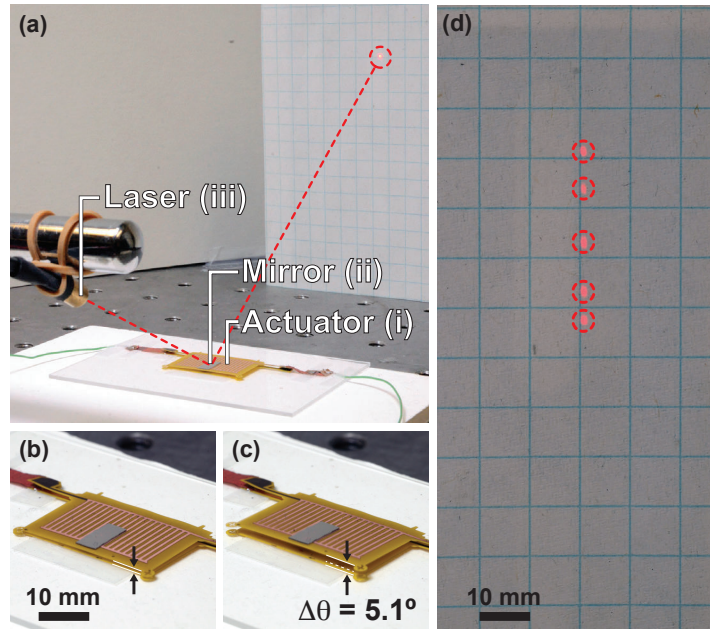
Figure 2.17: (a) 1-DoF micro-mirror composed of a 2-layer RFA (i) and a metallized glass coverslip mirror (ii) controllably steers a laser beam (iii). Resonant performance at 16 Hz and 1000 V peak-to-peak, with: (b-c) actuation of RFA and (d) movement of laser dot at resonance (approx. 5.1°).

from a single sheet of Pyralux AP that is folded in half to form the two layers. The bottom layer is adhered to a glass slide; the top layer is aligned / suspended by two polyimide torsional springs. The two layers are connected at the spring anchors, and share common V_+ / V_- terminals at these locations. Power to the top layer is supplied by copper traces on the spring suspension. The mirror is a metallized glass coverslip (100 μm thick), cut to size and placed on the top layer. The mirror reflects the beam from a laser diode mounted over the micro-mirror system.

The micro-mirror operates stably with open-loop control: applied voltages of 0–1000 V generate angular displacements of 2.2° (at low-frequencies) up to 5.1° (at 16 Hz resonance). The micro-mirror has peak input power of 2.57–41.0 mW and current of 3.81–60.4 μA at 1–16 Hz, respectively. Further, as the actuator displacement is proportional to its applied voltage, the micro-mirror can deflect controllably to any intermediate angles, unlike many commercial two-state (on / off) micro-mirrors.

Future applications of this actuator technology could also include large-area actuators (changing reflectivity / transparency for building thermal regulation [129]) and actuation on robot platforms that already employ high-voltage electrostatic grippers / adhesives [99].

2.7 Conclusion

In this chapter, we have demonstrated meso-scale repulsive force electrostatic actuators that employ a redesigned electrode geometry and are made using a flex-circuit planar manufacturing process. The electrode design changes enable actuators that operate at 20 times greater field strength and generate 8.6–10.5x greater electrostatic pressure (over previous RFA electrode designs) at the same operating voltage and electrode feature size. At the same time, our actuators are extremely robust – individual actuators have been tested without failure for >700,000 cycles at up to 1000 V, 0.1–100 Hz, and 0.25–1.00 Atm – since electrode defects or layer misalignment during operation reduce the repulsive force rather than causing a destructive shorting failure. This actuator design has other notable advantages:

- Open-loop stable operation without pull-in behavior (unlike attractive force electrostatic actuators)

- Peak force is generated at rest configuration (unlike attractive force electrostatic actuators)

- Voltage-controlled force and displacement, with no measured maximum ΔZ at which repulsive force becomes attractive (unlike prior RFA designs)

- Low mechanical hysteresis (unlike piezoelectric actuators and DEAs)

- Simple suspension for moving layers, since only one axis requires high stiffness and precise alignment

- No shorting failures if electrodes have manufacturing defects or if actuator layers are misaligned or touch, since oppositely-polarized electrodes are insulated by a resilient, incompressible dielectric substrate instead of air gaps (unlike prior RFA designs)

The fabrication process is comparable to conventional flexible PCB manufacturing processes, so cm-scale actuators can be immediately and inexpensively mass-produced. PCB vendors can even use the same Pyralux substrates we employ in this research to produce one- or two-sided actuator layers with higher density traces – 100 μm traces or gaps, compared to the 500 μm traces tested in-lab.

Fabricated actuators were observed to generate maximum repulsive forces up to 9.03 mN (36.1 Pa) and displacements of 242–511 μm across an open-loop stable bandwidth of 43 Hz with a 29 Hz resonant peak. A 290 mg micro-mirror system driven by an RFA was demonstrated to produce 5.1° rotations at 16 Hz resonance, and controllably steer a laser beam. Future work will investigate optimization of the actuator electrode geometry (for greater work output) and integrated capacitive sensing of actuator layer positions (for closed-loop control and drift compensation).

Chapter 3

Multi-Layer Actuators for a Micro-Mirror

Content in this chapter was originally published as "Multi-Layer, Thin-Film Repulsive-Force Electrostatic Actuators for a 2-DoF Micro-Mirror," *Actuators 2018* [97].

3.1 Introduction

Two complementary electrostatic actuator technologies have rapidly advanced in recent years: 2-layer MEMS repulsive-force actuators [42, 45, 113, 118] and multi-layer, thin-film attractive-force actuators [55, 72]. Thin-film actuators are lightweight, cheap, and easily fabricated (compared to MEMS actuators); multi-layer actuators generate greater strokes than two-layer actuators. Repulsive-force actuators have open-loop stable operation and generate peak force at initial configurations [100]. These characteristics make a multi-layer, thin-film repulsive-force actuator (RFA) ideal for sensor platforms on meso-scale robots [12, 35], including the two degree-of-freedom micro-mirror shown in Fig. 3.1.

Ben Mrad and colleagues [45, 118] demonstrated 3-DoF micro-mirrors (fabricated via PolyMUMPs) driven by 2-layer actuators with no pull-in and stable actuation over the full stroke length ($\pm 1.5°$ / 86 μm). Other micro-mirror systems have been produced in large arrays ($\pm 12°$ 1-DoF deflection) [115] and using micro-assembly (3.5° / 0.5 μm 3-DoF deflection) [127].

Ito and Saneyoshi [55] demonstrated the feasibility of a 50-layer thin-film actuator (400 μm stroke) with unstable gap-closing actuation and a pull-in limit, while He and Ben Mrad [42] modeled without fabrication a 3-layer MEMS RFA.

Schaler, *et al.* [100] introduced 2-layer thin-film RFAs and presented: the electrode pattern used in this chapter, an out-of-plane translational actuator (511 μm stroke), and a 1-DoF rotational micro-mirror system (5.1° deflection at resonance). Other 2-layer thin-film electrostatic actuators at the meso-scale have been shown that use attractive, rather than
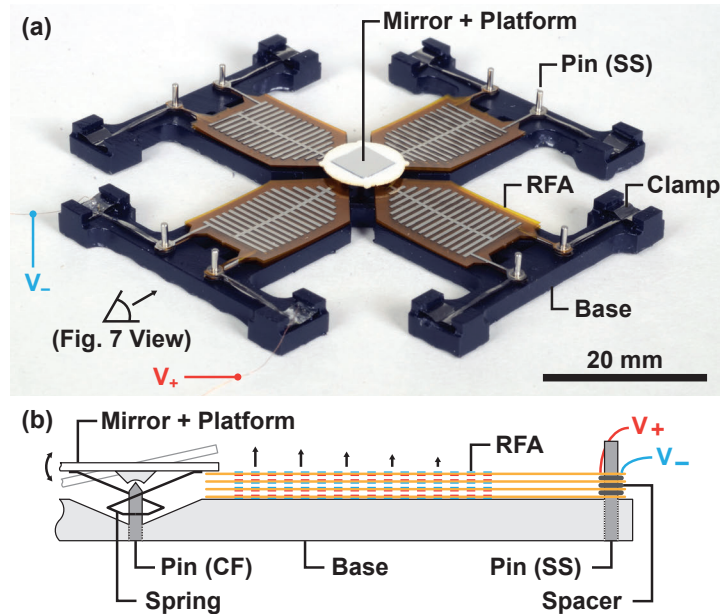
Figure 3.1: Fabricated 2-DoF micro-mirror system. (a) Image of assembled micro-mirror system with 3D-printed base, four 4-layer RFAs, and spring-loaded mirror. (b) Cross-section diagram of micro-mirror system (CF – carbon fiber; SS – stainless steel).

repulsive, actuation modes, including: a linear surface-drive actuator [74], an electrostatic film motor in a 49 g electroadhesive robot [122], and an electrostatic vibrator in a 47 mg crawling robot [85].

3.2 Fabrication

Multi-layer RFAs are easily fabricated by stacking multiple thin-film actuator layers – we demonstrate 4 to 8-layer stacks. The fabrication process for individual layers is shown in Fig. 3.2. Each layer consists of two stainless steel foil electrodes (Trinity Brand Industries, 12 μm thick) adhered to each side of a polyimide (Dupont Kapton, 25 μm) substrate with thermally-activated sheet adhesive (GBC Octiva Hot Mount, 17.5 μm). The electrodes and the substrate are laser-micromachined with a UV laser (PhotoMachining Inc., 355 nm), visually aligned, and laminated to form a composite.

Fig. 3.3 shows an individual RFA layer and a magnified view highlighting alignment quality between electrodes on each side of the dielectric substrate (minor 35 μm misalignment is visible at the tip). The electrode dimensions correspond to those defined in Fig. 3.4.

Complete layers are stacked to form actuators (Fig. 3.1, 3.5): pins on a 3D-printed base and spacers (100 μm) provide exact alignment constraints between layers; spring suspension (k = 2.3 N/m) from cantilevered beams and residual curvature of individual layers provides a gravity offset and restoring force. This electrode pattern is scalable to sub-100 μm features
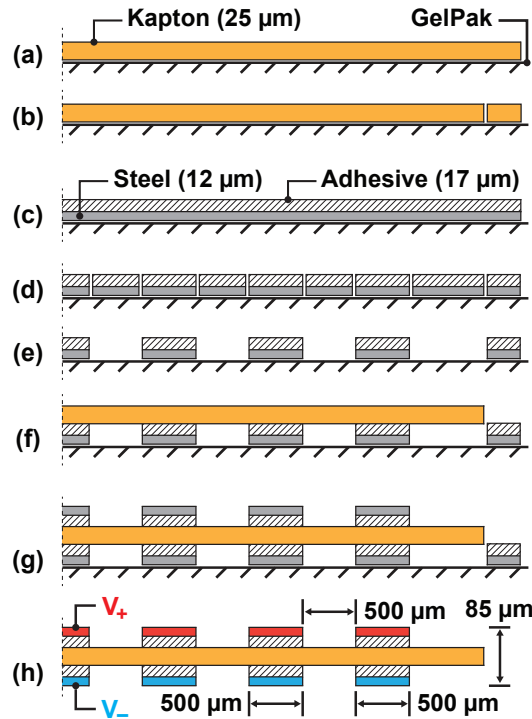
Figure 3.2: Process for fabricating a single RFA layer. (a-b) Substrate is laser-cut from Kapton film (25 μm) secured on GelPak. (c-d) Electrodes are laser-cut from stainless steel foil (12 μm) bonded to thermally-activated sheet adhesive (17 μm) and secured on GelPak. (e) Excess foil is removed from the patterned electrodes. (f-g) Kapton substrate is visually aligned on top of one set of patterned electrodes, bonded (with heat), removed, flipped over, and repeated on a second set of electrodes. (h) Electrodes are connected to a power supply (V_+ / V_-), with opposite sides charged differentially.
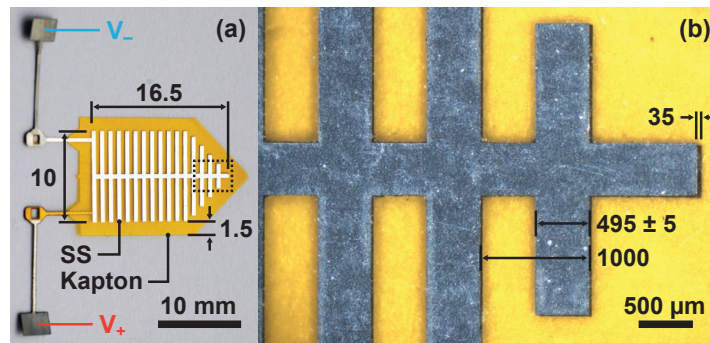
Figure 3.3: Fabricated actuator layer (a) with magnified view of outlined area (b).
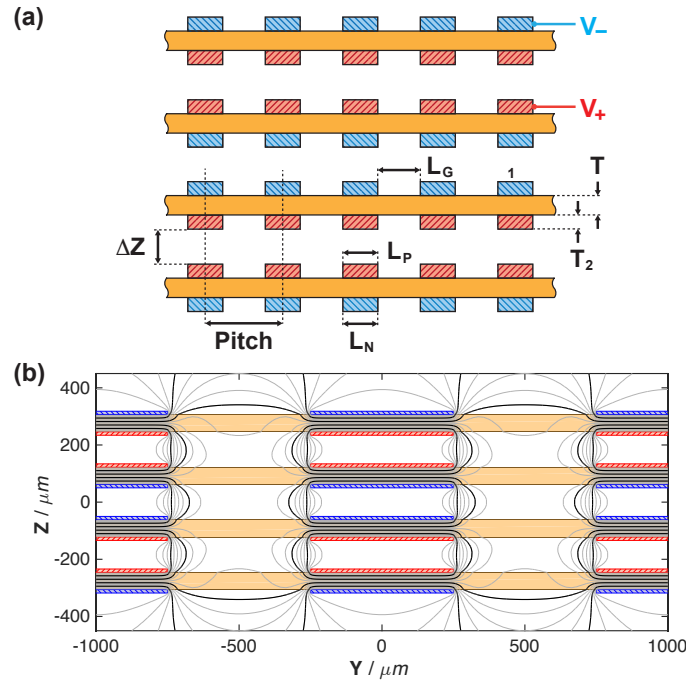
Figure 3.4: Cross-section diagram (a) and electrostatic simulation (b) of the multi-layer RFA, with each layer consisting of metal electrodes laminated to an insulating substrate ($L_P = L_N = L_G = 500 \ \mu m$, Pitch $= 1000 \ \mu m$, $T_1 = 60 \ \mu m$, $T_2 = 12.5 \ \mu m$). Exterior layers experience the greatest electrostatic force imbalance and thus the largest net repulsive forces, as seen in Fig. 3.5.

with other manufacturing processes. The cross-section schematic and simulation of electric potential throughout a 4-layer RFA is shown in Fig. 3.4.

3.3 Characterization

A multi-layer RFA was assembled (Fig. 3.5) and the actuator's free displacement dependence on number of layers was measured at two operating voltages (Fig. 3.6). The RFA, with 2 – 8 layers, is driven by a square-root of sinusoid signal ($0 - 1000$ or $2000 \ V$ peak-to-peak at $0.25 \ Hz$) for 6 cycles. The minimum and maximum RFA height each cycle is recorded by camera and measured in ImageJ. Layers are added in pairs to ensure the outermost (exposed) electrodes are always grounded.

RFA displacement increases with both number of layers and voltage: from $0.62 \ mm$ (2 layers at $1000 \ V$) to $1.55 \ mm$ (8 layers at $2000 \ V$) – a $2.5\times$ increase. RFA displacement can thus be increased by operating at a higher voltage (as demonstrated previously in [100]) or by adding extra layers for a given operating voltage.

Note that the actuator performance can be negatively affected by substrate electrostatic
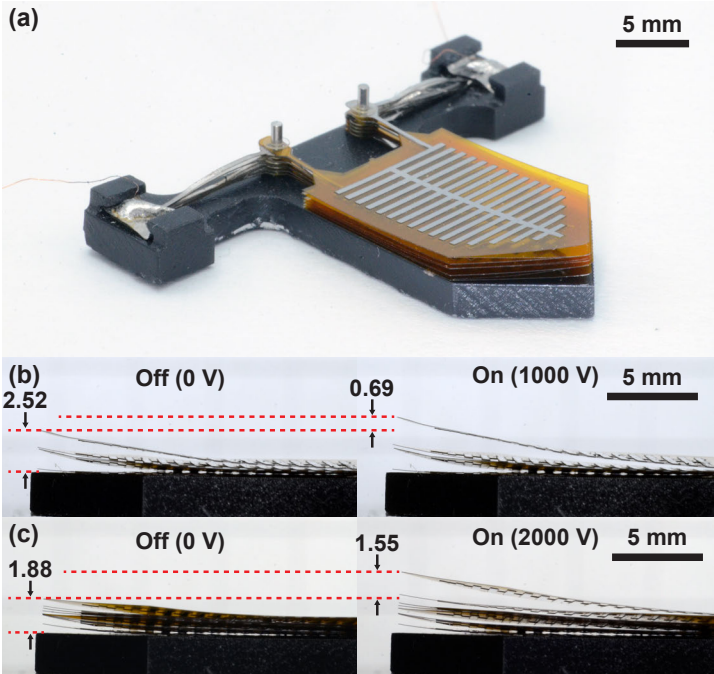
Figure 3.5: Isometric view (a) of an 8-layer RFA, and side views of a 4-layer (b) and 8-layer (c) RFA operating at 0 to 1000 / 2000 V, respectively.
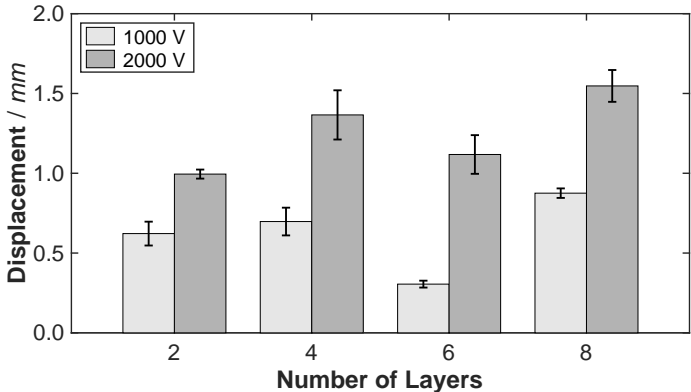
Figure 3.6: RFA displacement versus number of layers at $0 - 1000$ / 2000 V, with error bars for 6 cycles of a single RFA stack. Note that static charging of the polyimide substrate is presumed to account for the reduced displacement in the 6-layer test.

charging, which causes individual layers to stick together and reduces the net stack free displacement. This behavior is seen in the 6-layer test with 0.30 mm displacements at 1000 V and 1.12 mm displacements at 2000 V (once the increased repulsive force partially overcomes the static cling). Electrostatic charging of polyimide substrates has been previously reported in literature [21, 120], and has been successfully minimized using an O_2 plasma etch [66].

3.4   Micro-Mirror

3.4.1   Fabrication

The micro-mirror assembly (Fig. 3.1) uses four stacks of 4-layer RFAs arranged symmetrically around a spring-loaded mirror platform. The four RFAs operate in antagonistic pairs to increase the mirror deflection about each of the two axes of rotation. The RFAs push against, but are not bonded to, the mirror platform. This creates a sliding contact point that decouples the impact of actuators operating orthogonally to one another.

The metallized glass coverslip mirror (100 μm thick) sits on a mirror platform containing a pin-and-socket joint for smooth 2-DoF pivoting with a polyimide helical spring suspension (12 μm thick) providing restoring forces. The pin is a sharpened 0.5 mm carbon-fiber rod; the socket is 3D-printed (Formlabs, Form 2).

3.4.2   Operation

Fig. 3.7 shows the 2-DoF micro-mirror in operation, and steering a laser beam to repeatably draw multiple patterns using open-loop control. Each actuator is driven by an individual high-voltage amplifier – Trek PZD700 for high frequency, 1000 V tests, and XP Power GP60 for low frequency, 2000 V tests – and opposing actuators are supplied inverted signals (with an offset bias of 50% peak voltage).

Fig. 3.8 shows the angular displacement of the mirror due to the two antagonistic actuators operating on one axis of the 2-DoF micro-mirror. The actuators are driven in 100 V steps from 0 – 1000 V, with measured mirror deflections of +1.4° to -2.6° (over 5 cycles). Deflections up to 8.8° (Fig. 3.7) were measured when operating at 2000 V. Hysteresis is visible between forward- and back-driving the actuator – 0.27° at 500 V, the neutral position where both actuators operate at equal voltage. Discrepancy between the maximum positive / negative displacement is likely due to variation in layer manufacturing, alignment, or stacking that enable one actuator to generate greater forces than the other.

Fig. 3.9 shows the frequency response for the same axis of the 2-DoF micro-mirror, with actuators now driven by 0 – 1000 V sinusoids. The mirror has a low frequency (1 Hz) net displacement of 3.8° and a bandwidth of 35 Hz (-3 dB).

The measured operating properties and peak angular displacement of the micro-mirror are presented in Table 3.1, along with the performance of published micro-mirror systems. Compared to existing 3-DoF systems in [45, 118, 127]: this 2-DoF system generates larger
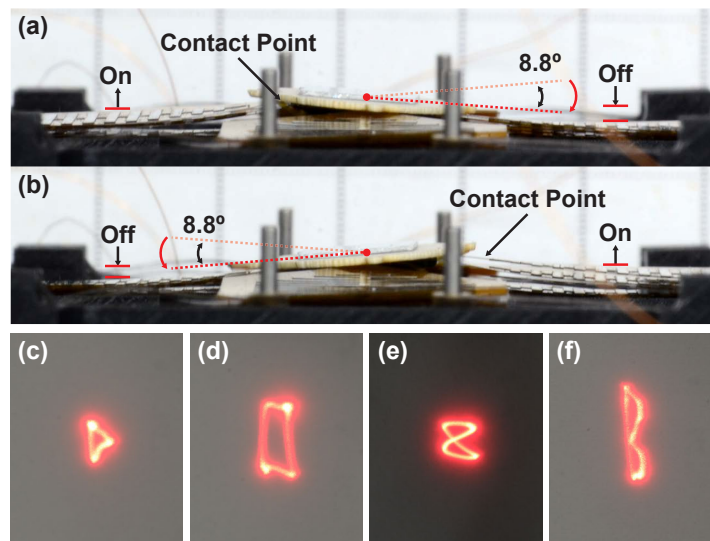
Figure 3.7: Steerable mirror deflections (a-b) along one axis with operation at $1\ Hz$ / 2000 V. 2-DoF laser patterns (c-f) with actuators operating at controlled waveforms between $0 - 2000\ V$ to form (left to right): triangle, rectangle, Lissajous, and 'B'.
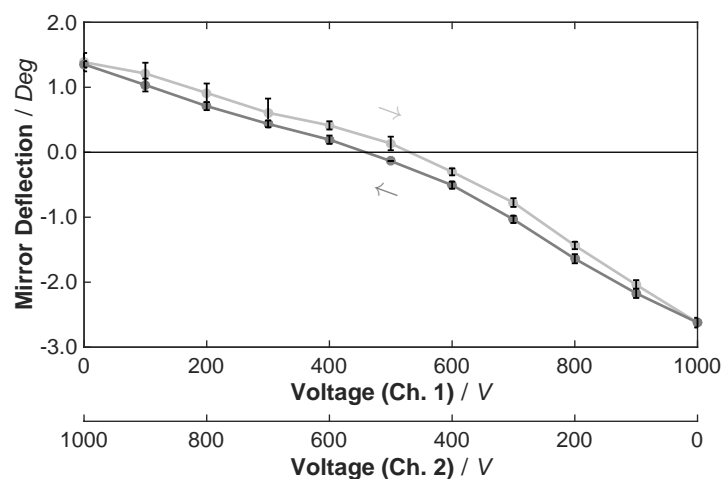
Figure 3.8: Angular displacement of mirror versus applied voltages $(0 - 1000\ V)$ of two antagonistic actuators. Average and standard deviation for 5 cycles with $0.5\ s$ ramp and hold in $100\ V$ increments.
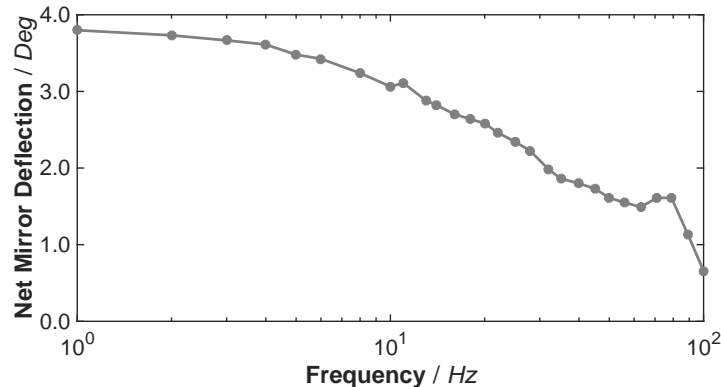
Figure 3.9: Angular displacement of mirror (net) versus operating frequency, for actuators operating with an applied sinusoidal voltage at $0 - 1000\ V$.

Table 3.1: Operational performance of electrostatic micro-mirrors from this and other work.

Design	Mechanical			Electrical		Performance			Source
	Process	A (mm^2)	DoF (#)	V (V)	E (V/m)	BW (Hz)	θ (°)	ΔZ (μm)	
Attractive Force	Micro-Masonry	0.9 x 0.9	3	80	$2.1{\cdot}10^6$	1200	3.5	0.5	[127]
Repulsive Force	PolyMUMPS	3.3 x 3.3	3	200	$3.8{\cdot}10^6$	200	±1.5	86	[45]
RFA (2-Layer)	Wet Etch	45 x 15	1	1000	$40{\cdot}10^6$	16	5.1	–	[100]
		25 x 10	1	1000	$40{\cdot}10^6$	43	–	511	[100]
RFA (4-Layer)	Laser	60 x 60	2	2000	$33{\cdot}10^6$	35	8.8 / 7.6	–	This Work

A – Area   **DoF** – Degrees of Freedom   **V** – Voltage   **E** – Electric Field Strength   **BW** – Bandwidth θ – Angular Displacement Δ**Z** – Normal Displacement

angular displacements (up to 8.8° and 7.6° at 2000 V along the two axes) and higher field strength (33 MV/m), but a lower bandwidth (35 Hz) and minimal out-of-plane translation.

3.5   Conclusion

We have demonstrated multi-layer, thin-film repulsive-force electrostatic actuators that generate greater displacements than conventional 2-layer RFAs. A simple manufacturing process using laser-cut metal foil enables rapid fabrication of many RFA layers. A 2-DoF micro-mirror system was then developed, which employs four 4-layer RFAs to stably tilt a spring-loaded mirror up to 8.8° and 7.6° on its two axes with a 35 Hz bandwidth. Prior MEMS devices were limited to angular deflections of ±1.5° [45] (stable) and 3.5° [127] (unstable), albeit with higher bandwidth.

Future work will reduce the RFA layer size for a more compact system, explore linear (as opposed to cantilever) suspensions for greater angular deflection, and add capacitive sensing for closed-loop control of mirror position.

Chapter 4

Bidirectional Actuators for a Milli-Robot

Content in this chapter was originally published as "Bidirectional, Thin-Film Repulsive-/Attractive-Force Electrostatic Actuators for a Crawling Milli-Robot," *MARSS 2018* [98].

4.1 Introduction

An array of novel μm- to cm-scale actuation technologies have enabled the proliferation of mobile meso-scale robots in recent years.

Numerous mm- to cm-scale robots employ electrostatic actuators: a multi-phase electrostatic film motor with electroadhesion [74, 122], an oscillating electrostatic film actuator inducing robot body vibrations [85], paper zipper actuators with anisotropic friction feet [15], and scratch drive actuators providing inchworm locomotion [19, 104]. All use attractive-force electrostatic actuators, and all except [19, 85] are tethered. Electrostatic actuators operate with few moving parts, simple control signals, and forces proportional to applied voltages.

Other meso-scale robots are powered by piezoelectric actuators – flying insect [69], myriapod [49], HAMR-V/F [7,32], LPMR [18] – by shape memory alloy actuators – RoACH [52], MEDIC [64], HAMR [6] – and by magnetic actuators [81, 121]. Finally, vibration-induced ambulation of robots has been achieved in a silicon hexapod [86] (via substrate excitation), Resbot [102] (using electromagnetic motors), and the previously mentioned electrostatic- [85] and piezoelectric- [18] actuator powered robots.

In this chapter, we present a new bidirectional, thin-film Repulsive-/Attractive-Force electrostatic Actuator (RAFA), and use it to construct a 132 mg milli-robot (Fig. 4.1). RAFAs generate active, voltage-controlled forces throughout the full actuation cycle (both extension and retraction), yielding larger work-loops than unidirectional actuators with passive spring returns (Fig. 4.7) [15,85,104]. RAFAs use simple integrated springs and spacers
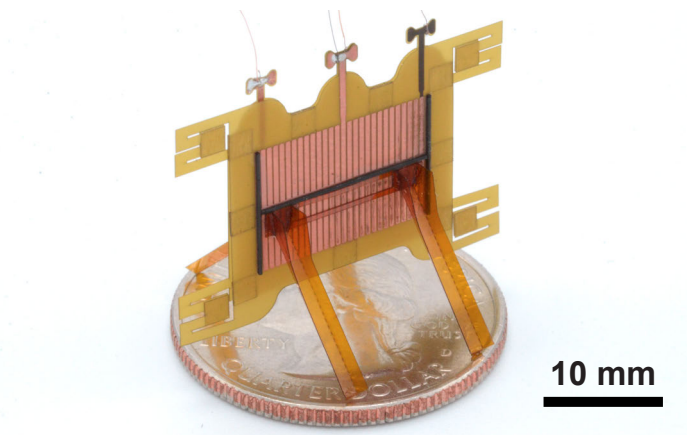
Figure 4.1: RAFAR, a 132 *mg* thin-film crawling milli-robot with integrated repulsive-/attractive-force electrostatic actuator.

for alignment (bidirectional slider film motors need tensioners, yaw guards, etc. [122]), and employ no exotic materials or manufacturing processes.

4.2 Background

Electrostatic actuators consist of sets of differentially-polarized electrodes that operate in one of two modes: attractive-force actuators (AFAs) generate attractive forces and gap-closing motion while repulsive-force actuators (RFAs) generate repulsive forces and gap-opening motion [100]. AFAs have unstable operation (pull-in instability) and stroke length is limited by the initial electrode gap. RFAs have open-loop stable operation (force, displacement are directly proportional to voltage) and stroke length is limited only by the electric field strength [100]. Both RFAs and AFAs can operate in series to increase stroke length [11, 55, 61, 97].

RFAs were initially developed by Tang, *et al.* [113], to levitate a MEMS resonator's moving electrodes. He, *et al.* further investigated MEMS RFA designs [41], simulated multi-level RFAs [42], and fabricated 1-/2-DoF micro-mirrors [43, 45] and low-voltage RFAs [118].

Schaler, *et al.* [100] introduced *cm*-scale linear and rotational thin-film RFAs with a new, higher-force electrode pattern. Then, [97] demonstrated multi-layer thin-film RFAs and a 2-DoF micro-mirror. Thin-film RFAs consist of metal foil / polyimide composites that are inexpensive, simple to fabricate, and allow greater flexibility in electrode configurations or multi-layer devices than MEMS equivalents.

RAFAs employ 2 control signals to selectively operate 1 actuator as a RFA or AFA, and achieve bidirectional actuation. Bidirectional motion with 2 antagonistic actuators was shown using AFAs [62], RFAs [97], and bimorph piezoelectric actuators [125]. Bidirectional motion of 1 MEMS electrode operated as a RFA / AFA was shown in [88], but required individual control signals to 6+ adjacent electrodes.
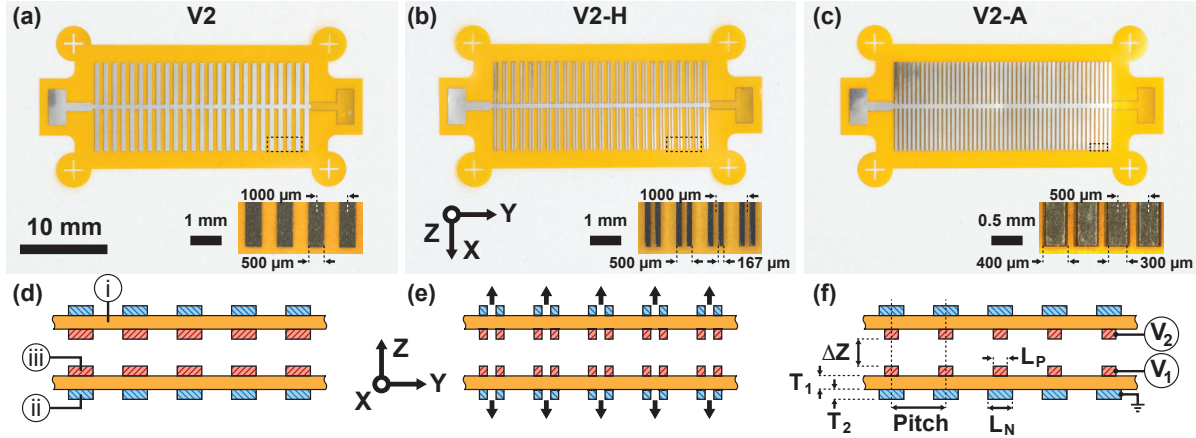
Figure 4.2: Flexible, two-layer repulsive-force actuator designs fabricated in this work: (a) V2, the electrode design used in Schaler, et al. [100], (b) V2-H, an improved design with hierarchical electrodes, (c) V2-A, an improved design with asymmetrical electrodes. For each actuator electrode design, the two functional layers are photographed (a-c) and the cross-sections are illustrated (d-f). Each actuator layer is composed of a polyimide substrate (i) with negative (ii) and positive (iii) electrodes. Actuator layers experience a net repulsive electrostatic pressure, illustrated in (e). Actuator dimensions include the substrate ($T_1 = 60 \ \mu m$) and electrode ($T_2 = 12.5 \ \mu m$) thickness, positive (L_P) and negative (L_N) electrode width, pitch ($Pitch$), and inter-layer height (ΔZ), listed hereafter as $\underline{x} = [L_P, L_N, Pitch]$. For V2, $\underline{x} = [500, 500, 1000] \ \mu m$ ($L_P = L_N = Pitch/2$); for V2-H, $\underline{x} = [167, 167, 1000] \ \mu m$ in clusters of two electrodes separated by 333 μm pitch; for V2-A, $\underline{x} = [300, 400, 500] \ \mu m$.

4.3 Simulation

Three actuator electrode designs are investigated for maximizing repulsive-work (see Fig. 4.2):

V2 Symmetric electrodes, all of equivalent size / pitch

V2-H Hierarchical electrodes, all of equivalent size but clustered in groups by varying pitch

V2-A Asymmetrical electrodes, with consistent pitch but positive / negative electrodes of non-equivalent size

(**V1** and **V2** electrode designs are compared in Ch. 2 [100])

In each case, the actuator layers are modeled with dimensions equivalent to the fabricated actuator layers in Sec. 4.4.1. Positive and negative metal electrodes are defined on opposing sides of an insulating substrate (a continuous dielectric film) and offset by a patterned adhesive film.

For each RFA design, the electric potential (V), electric field ($\underline{E}$) vector, and corresponding bound / free surface (σ_b, σ_f) and volumetric (ρ_b, ρ_f) charge densities are calculated via

finite differences simulation. Details on numerical simulation of RFAs can be found in E. Schaler, *et al.* [100] and alternate models are presented in [41–43]. The electrostatic force on a region of the actuator is:

$$\underline{F} = \iiint_{\mathbb{V}_\mathbb{E}} (\rho_f \underline{E}) d\mathbb{V} + \iiint_{\mathbb{V}_\mathbb{D}} (\rho_b \underline{E}) d\mathbb{V} + \iint_\mathbb{S} (\frac{1}{2}(\sigma_f + \sigma_b)\underline{E} \cdot \hat{n}) d\mathbb{S} \tag{4.1}$$

with force contributions from the electrode ($\mathbb{V}_\mathbb{E}$) and dielectric ($\mathbb{V}_\mathbb{D}$) volume interiors and the interfacing surfaces between these regions ($\mathbb{S}$, with surface normal vector $\hat{n}$). The electrostatic pressure is calculated by dividing the electrostatic force by electrode area (with lengths based on multiples of electrode pitch). The actuator work (W):

$$W = \int_{\Delta Z_0}^{\Delta Z_1} \underline{F}(\Delta Z) dZ \tag{4.2}$$

is estimated by piecewise integration of the electrostatic force at a range inter-layer heights (ΔZ). Subsequently the V2-A design was also modeled with the RAFA electrode polarization to determine attractive force and work over an equivalent range.

4.3.1   Optimization

The work-optimized electrode geometry is determined by solving the nonlinear, convex optimization problem:

$$\min_{\underline{x}} -W(\underline{x}), \text{ with } \underline{x} = [L_P, L_N, Pitch] \tag{4.3}$$

$$W(\underline{x}) = P(\underline{x}) \cdot \int_{\Delta Z_0}^{\Delta Z_1} F_z(\underline{x}, \Delta Z) dZ \tag{4.4}$$

$$P(\underline{x}) = \frac{F_z(\underline{x}, \Delta Z, \Delta Y)}{F_z(\underline{x}, \Delta Z, 0)} \tag{4.5}$$

subject to constraints:

$$L_P, L_N \in [250\mu m, 1000\mu m] \tag{4.6}$$
$$Pitch \geq L_P, L_N$$
$$Pitch \leq 5000\mu m$$

Work (W) is maximized for a given actuator electrode geometry ($\underline{x}$) (4.3), and calculated by piecewise integration of the normal component of the actuator force (F_z) at a range inter-layer heights $\Delta Z \in [\Delta Z_0, \Delta Z_1] = [25, 500]$ μm (4.4). A misalignment penalty (P) is imposed on the work calculation to prevent the optimization from converging to a solution with alignment requirements beyond manufacturing capabilities (4.5). Here, a misalignment of $\Delta Y = 25$ μm is used and the force decrease is compared at $\Delta Z_0 = 25$ μm.

Constraints (4.6) are imposed by physical limitations on minimum feature size (100 μm) for fabrication / alignment, on minimum pitch (greater than electrode widths), and on maximum feature size (1000 μm) for a reasonably compact actuator system and to limit the search space.

The optimization problem is solved in Matlab using the *fmincon* nonlinear programming solver and sequential quadratic programming (SQP) algorithm.

4.3.2 Repulsive-Force Operation

The V2, V2-H, and V2-A RFA electrode designs are compared in Fig. 4.3.

The V2 symmetric electrode design (Fig. 4.2a/d), first presented in [100], employed equal-sized positive and negative electrodes $\underline{x} = [500, 500, 1000]$ μm, which provided a decent balance of high peak force (increases with smaller unit cells), and force reduction at greater ΔZ offsets (decreases as inter-layer distance increases, and decreases faster with smaller unit cells). This behavior is evident when comparing $\underline{x} = [500, 500, 1000]$ μm and $\underline{x} = [167, 167, 333]$ μm in Fig. 4.3e.

The V2-H hierarchical electrode design (Fig. 4.2b/e) provides a compromise on the performance of both large and small unit cell sizes in the V2 design. For this V2-H [167, 167, 1000] μm pattern, peak force is higher than the V2 [500, 500, 1000] pattern at all $\Delta Z \leq 200$ μm (due to a greater number of fringing fields) and higher than the V2 [167, 167, 333] unit cell design at distances of $\Delta Z > 70$ μm (due to a more gradual reduction in force at larger ΔZ).

The V2-A asymmetric electrode designs (Fig. 4.2c/f) are quite different: positive and negative electrodes are of unequal size, and pitch is less than twice the electrode widths (to reduce unit cell size and increase electrode density). This V2-A electrode design was discovered during the course of the parameter space exploration for the work-optimization simulations. The V2-A design with $\underline{x} = [300, 400, 500]$ μm used in the majority of this chapter was derived from the optimal design $\underline{x} = [307, 391, 451]$ for a $\Delta Y = 10$ μm misalignment penalty. L_P, L_N parameters were rounded to the nearest 100 μm, and $Pitch$ was increased to $L_N + 100$ μm to conform to manufacturing tolerances. An interesting simulation result of these designs is the force reduction trend as ΔZ increases: the typical $F \propto \Delta Z^{-2}$ fall-off in force is less pronounced at $\Delta Z \geq 150$ μm and sustained 0.35–0.36 kPa pressures are predicted even at $\Delta Z \geq 500$ μm gaps. Note that this behavior is not reflected in the measured actuators (Fig. 4.7).

4.3.3 Bidirectional Repulsive-/Attractive-Force Operation

A new capability of these V2 / V2-H / V2-A electrode geometries is the ability to generate both repulsive- and attractive-forces (Fig. 4.3a-d/f). This requires the use of two channels to independently control the potential on each actuator layer: layers generate a *net repulsive force* when the two internal electrodes operate at V_+; layers generate a *net attractive force* when the two internal electrodes differentially operate at $V_1 \ll V_2$ (or vice versa).
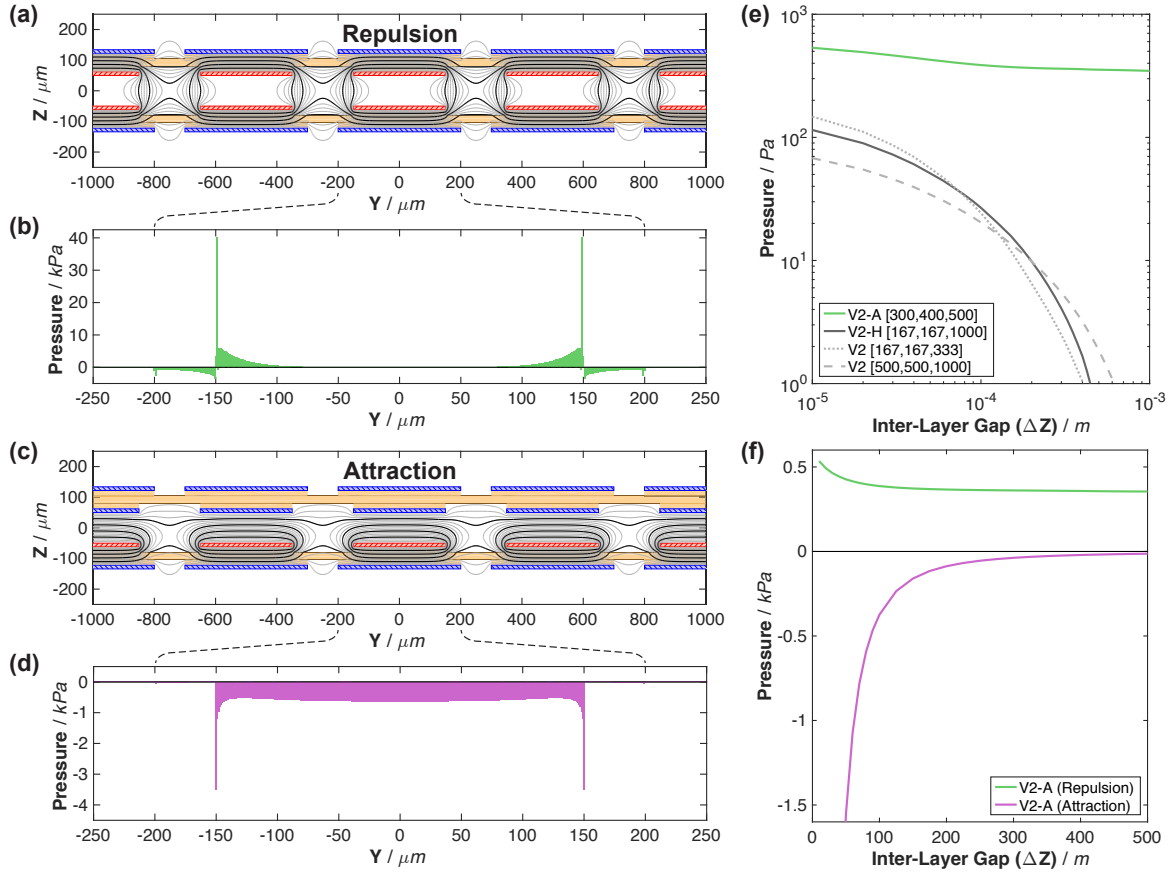
Figure 4.3: Simulation results for the bidirectional repulsive-/attractive-force electrostatic actuator. (a/c) Electrostatic potential (V) for V2-A design, with electrodes operating at 0 kV (blue) / 1.2 kV (red) and dielectric substrate (orange). (b/d) Net electrostatic pressure across the top layer of the V2-A design, focusing on the center electrode and with 1 μm mesh size. (a-b) are operating in repulsion-mode; (c-d) are operating in attraction-mode. (e) Net electrostatic pressure produced by a complete actuator versus layer separation (ΔZ) in each design, with dimensions of $\underline{x} = [L_P, L_N, Pitch]$. Operating voltage is 1.2 kV. (f) Net electrostatic pressure produced by a complete V2-A actuator versus layer separation (ΔZ) in both repulsion- and attraction-modes.
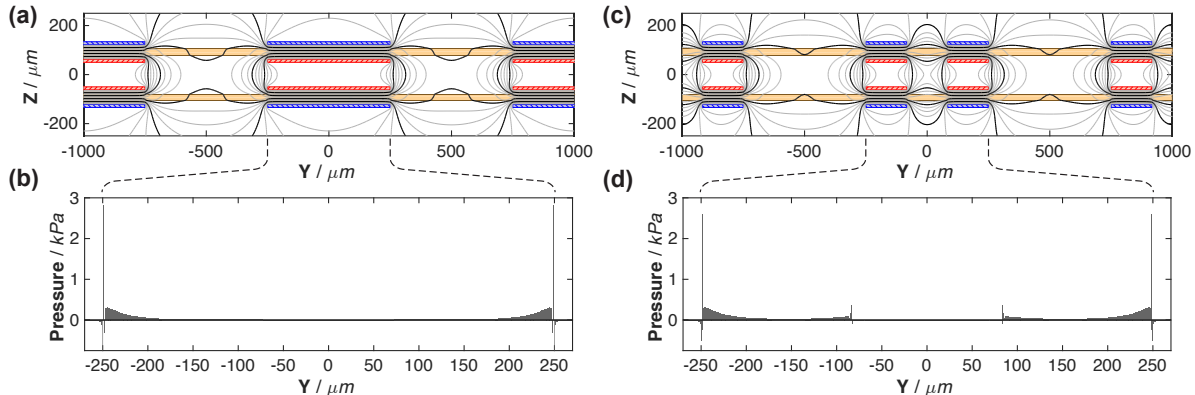
Figure 4.4: Simulation results for the repulsive-force electrostatic actuator, using the V2 (a-b) and V2-H (c-d) electrode configurations. (a/c) Electrostatic potential (V) for V2 / V2-H designs, with electrodes operating at 0 V (blue) / 1.2 kV (red) and dielectric substrate (orange). (b/d) Net electrostatic pressure across the top layer of the V2 / V2-H designs, focusing on the center electrode and with 1 μm mesh size.

As seen in Fig. 4.3f, both repulsive- and attractive-forces scale inversely proportional to displacement. Electrostatic pressures of 0.43–0.36 kPa (repulsion) and -1.55– -0.055 kPa (attraction) are generated with the same V2-A electrode geometry and $\Delta Z = 25$–250 μm range of inter-layer gaps.

4.4 Actuator Development

The V2-A electrode design was selected to be fabricated (Fig. 4.2) and characterized (Fig. 4.5– 4.7).

4.4.1 Fabrication

RFA layers are fabricated using both an in-house laser-cutting process (introduced in Chap. 3 [97] for rapid iterative design) and a commercial wet-etching process at a flex-PCB manufacturer (replaced an in-house wet-etching process introduced in Chap. 2 [100]).

In the laser-cutting process (see Chap. 3 [97]): layers are composed of stainless steel electrodes (Trinity Brand Industries, 12.7 μm) on a polyimide substrate (DuPont, Kapton FPC, 25 μm), bonded together with thermally-activated sheet adhesive (GBC, Octavia Hot Mount Adhesive, 17.5 μm).

The electrodes are prepared by cleaning a sheet of stainless steel, laminating thermal adhesive to one side, and securing the other side to GelPak (with the adhesive face-up). The substrate is prepared by cleaning the Kapton and securing it to another GelPak surface. The actuator electrode pattern and substrate extents are cut into the respective material layers

using a UV laser cutter (PhotoMachining Inc., 355 *nm* laser). Excess mask and substrate material are removed manually. The substrate / electrode layers are run through a laminator to set the thermal adhesive. Any exposed thermal adhesive is removed with acetone (Fischer Scientific). Production time is approximately 2–3 hours per sheet of actuator layers (compared to >4 hours for the wet-etching process in [100]).

In the wet-etching process (see Chap. 2 [100]): layers are composed of a flexible circuit composite (Dupont, Pyralux AP8515) with 18 μm copper foil electrodes bonded to each side of a 25 μm polyimide substrate.

A commercial manufacturer of flexible circuit boards (The Boardworks) was used to pattern an array of two-sided actuator layers (72 layers at \$3.40 per layer) on a single 9 x 12 *inch* sheet of Pyralux AP. The copper foil was etched in a wet-etch process, with electrode patterns aligned on both sides of the polyimide substrate. The polyimide substrate was subsequently patterned using the UV laser cutter. The resulting individual actuator layers (cut out of the full sheet) contain patterned electrodes surrounded by 4 polyimide suspension springs.

RAFA layers can optionally adhere film spacers (50–100 μm thick) or an extra polyimide film insulator (25 μm) over the V_+ electrode on one layer for shorting protection between layers during attractive-mode operation.

4.4.2 Process Trade-offs

As introduced above, there are three processes currently available for RFA / RAFA fabrication: in-house laser-cutting or wet-etching processes, and out-sourced commercial wet-etching. The processes are compared in Table 4.1.

The in-house processes are ideal for iterative prototyping of new robots, actuators, or electrode patterns, but produce lower electrostatic pressures due to worse electrode alignment / accuracy or thicker substrates. The commercial flexible circuit fabrication process allows anyone to produce large quantities of actuators with higher pressures, consistently accurate electrode patterns, and the best electrode alignment.

Future fabrication process iterations could also employ a conductive ink printing processes for roll-to-roll bulk fabrication on thin-film substrates.

Table 4.1: Comparison of actuator fabrication processes.

Metric	Laser (IH)	Etch (IH)	Etch (C)
Prototype Fabrication	+	o	–
Bulk Fabrication	o	–	+
Electrostatic Pressure	–	o	+
Electrode Dimensional Accuracy	+	–	o
Electrode Alignment (2-Sided)	o	–	+

(IH) – In-House   **(C)** – Commercial

4.4.3   Characterization

The repulsive forces of the fabricated actuator layers were characterized using the same blocked-force testing apparatus presented in [100]. The actuator layers are laminated to glass slides. The first layer is secured to an XY-stage; the second layer is mounted to the load cell and Z-stage with a wax interface (for proper leveling). Actuators are controlled by a DAQ (NI, USB-6341) and Labview, and powered by high-voltage amplifiers (Trek, PZD700 / XP Power, G-60).

RFA-mode testing uses a sinusoidal signals of 0–1.2 kV and 2 Hz. RAFA-mode testing uses trapezoidal signals of 0–1.2 kV and 1 Hz (with 0.1 s ramps and 0.25 s holds at peak repulsive / attractive forces).

4.4.4   Results

Fig. 4.5 demonstrates the blocked-force performance of the RFA. The RFA generates smooth sinusoidal forces (the quadratic relationship between applied voltage and measured force is shown in Fig. 4.5b) with no discernible lag or nonlinearities. Minimal hysteresis is visible and dielectric charging results in only a 14% decrease in peak force over 10 cycles.

Fig. 4.6 demonstrates the blocked-force performance of the RAFA. The RAFA quickly tracks the trapezoidal waveform during voltage ramps (in grey) and maintains stable repulsive- and attractive-forces during voltage holds at 1.0 / 1.0 kV (V_1 / V_2) and 1.0 / 0.5 kV (V_1 /
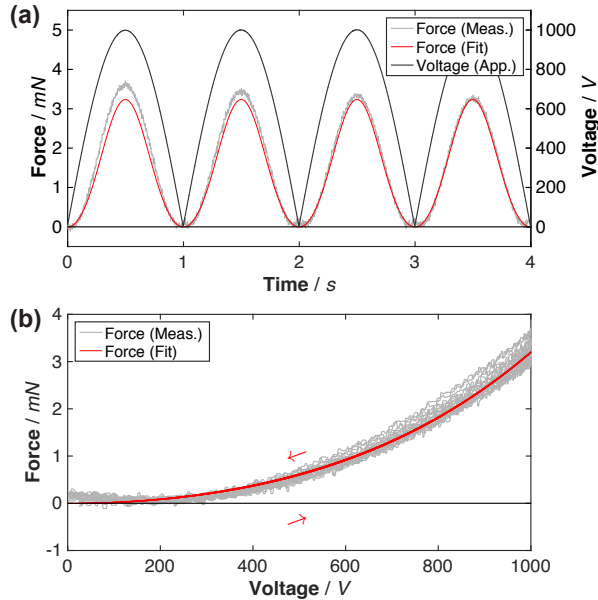
Figure 4.5: RFA with V2-A electrode pattern generating repulsive-forces at $\Delta Z = 100$ μm and 0–1.0 kV. (a) Applied square-root of sinusoid voltage and measured force versus time, with sinusoidal fit. (b) Measured force versus applied voltage, with the same fit.
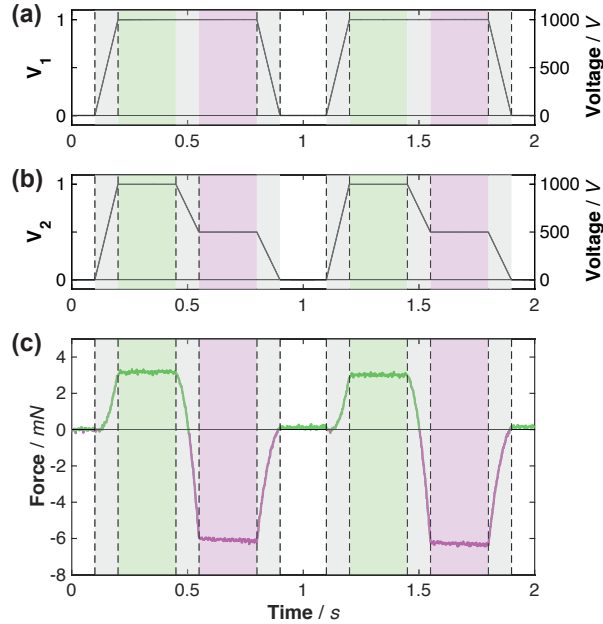
Figure 4.6: RAFA with V2-A electrode pattern controllably generating repulsive- and attractive-forces at $\Delta Z = 100$ μm and 0–1.0 kV. Commanded V_1 (a) and V_2 (b) trapezoidal signals along with measured applied voltage. (c) Measured force versus time. In (a/b), green regions represent voltage signals designed for repulsion and purple regions represent those for attraction. In (c), measured repulsive forces are green and attractive forces are purple.

V_2), respectively. Note that square waveforms reduce polyimide's mean-time-to-failure [65], and are avoided. The RAFA was tested for up to 100 cycles using this waveform (at 1 Hz), with dielectric charging causing a -19% / +10% change in repulsive / attractive force after 10 cycles and -35% / +20% change after 100 cycles (amounting to a 1.2 mN decrease in peak forces). During unpowered (0 V) periods, the RAFA exhibits near-zero force production – indicating minimal residual charge.

Fig. 4.7 presents the actuator force versus ΔZ offset, with both sinusoidal and trapezoidal applied voltages. Peak repulsive forces of 38.9 mN (156 Pa at 2.5 cm^2 electrode area) and peak attractive forces of 80.0 mN (356 Pa) were measured at $\Delta Z = 30$ μm and 1.2 / 0 kV (V_1 / V_2).

4.5 Robot Development

The Repulsive-/Attractive-Force Actuator Robot (RAFAR) is a thin-film milli-robot developed with an integrated 2-layer RAFA (Fig. 4.1). The assembled robot has dimensions of 20 (long) x 27 (wide) x 22 (tall) mm, a total mass of 132 mg, and uses an inchworm crawling sequence to locomote (Fig. 4.8). The robot successfully crawls on an aluminum foil substrate
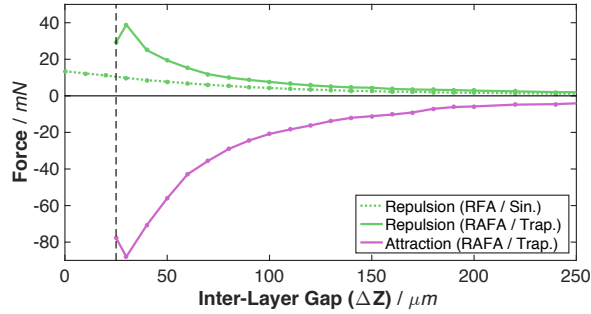
Figure 4.7: Thin-film electrostatic actuator controllably generating repulsive- and attractive-forces. Measured forces for a 2.5 cm^2 actuator operating in repulsive-force (RFA) and repulsive-/attractive-force (RAFA) modes, with sinusoidal (Sin.) and trapezoidal (Trap.) waveforms. Peak applied voltage in all cases is approx. 1.2 kV. Vertical dashed line marks contact point ($\Delta Z = 25\ \mu m$) of the two layers (in RAFA-mode) due to an inter-layer polyimide insulator.

at an average speed of 0.32 mm/s (0.012 BL/s) over 5 steps at 1 Hz (see **Video**), and its performance is compared to other milli-robots in Table 4.2.

The repeating sequence of alternating repulsive-/attractive-forces used for this crawling pattern was successfully generated (Fig. 4.6). Use of both repulsive- and attractive-actuation substantially increases the potential work-loop (over an equivalent spring restoring force), as shown in Fig. 4.9. Actuator displacements require that generated actuator forces (measured in Fig. 4.7) be greater than measured foot friction forces (Fig. 4.11). This sequence also depends on foot friction anisotropy (characterized in Fig. 4.11) for forward motion.

4.5.1 Body Design

The RAFAR is composed of a 2-layer RAFA that was wet-etched by a commercial vendor (Sec. 4.4.1) and uses the V2-A electrode configuration ([300, 400, 500] μm) to ensure the highest force production possible. The RAFA layers are connected via a folded-spring suspension (4 springs located at actuator corners) that provides actuator layer alignment, mechanical constraints (compliant to normal force / stiff to shear force), and some restoring force. The RAFA is reinforced by three carbon fiber rods (Ø 280 μm) adhered to each ground electrode (to avoid affecting the electric field) and PET spacers (2 x 2 x 0.118 mm thick) that are adhered to one actuator layer around the perimeter of the internal electrodes. The spacers act as mechanical stops to maintain inter-layer spacing ($\Delta Z \geq 100\ \mu m$) and prevent electrode contact / shorting during attractive-mode operation. Total mass is 132 mg, including: actuator (107 mg), carbon fiber reinforcement (6.0 mg), legs (19.0 mg, 4 x 4.75 mg).

Power is supplied to the robot via four 75 μm wires (V_1, V_2, and 2 V_- grounds), which are soldered directly to electrode pads on each actuator layer. The wires are routed via an
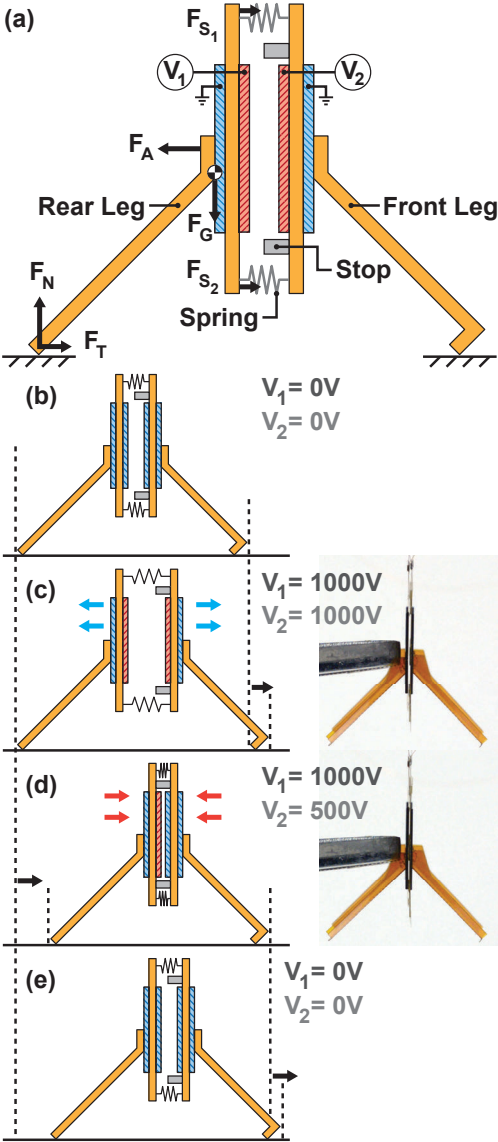
Figure 4.8: RAFAR cross-section and crawling behavior – cycling between extension of the front legs (c) (with repulsive-force) and retraction of the rear legs (d) (with attractive-force).
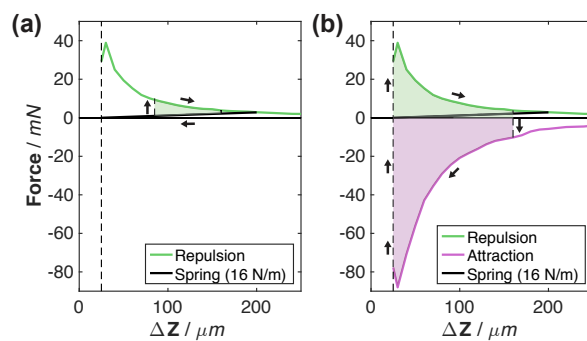
Figure 4.9: Work loops for RFA (a) and RAFA (b), based on actuator (Fig 4.7), foot friction (Fig. 4.11), and spring forces. RAFAR's actuator has 42% smaller area, thus correspondingly reduced forces are expected for the fabricated robot.
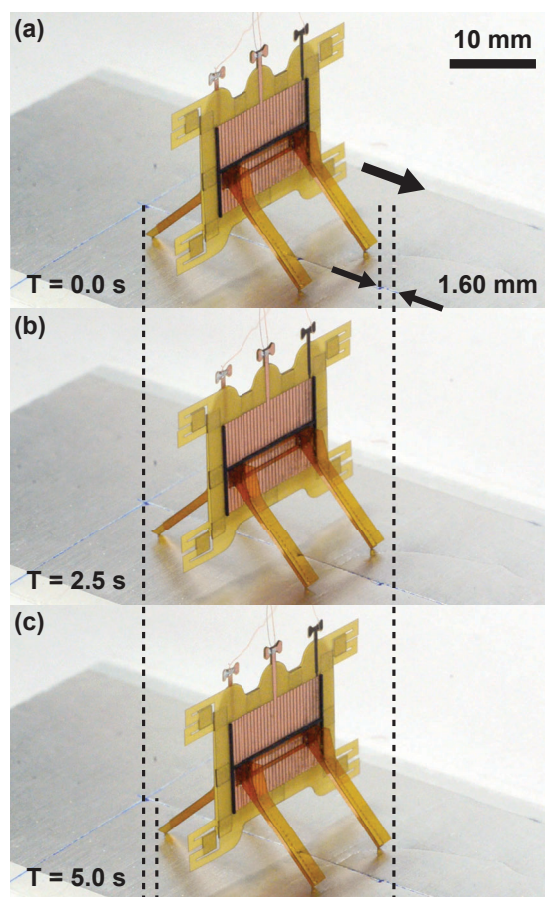
Figure 4.10: RAFAR crawling sequence at the start (a), middle (b), and end (c) of 5 steps (1.60 mm traveled).

Table 4.2: Survey of actuators used for meso-scale walking / crawling robots. Robots with greater capabilities – untethered (Tether) and steerable (Steer) – are rated higher (+) than those without (o).

Actuator Design	Act.	Tether	Steer	M / g	Dim. / m^3	Speed / m/s	BL/s	V / V	Source
Scratch Drive Electro.	2	+	+	–	60 x 250 x 10 $\cdot 10^{-6}$	$2.0 \cdot 10^{-4}$	1.25	± 140	[19]
Scratch Drive Electro.	1	o	o	–	30 x 15 x 10 $\cdot 10^{-3}$	$3.7 \cdot 10^{-4}$	0.122	4000	[104]
Zipper Electro.	1	o	o	0.55	60 x 10 x 10 $\cdot 10^{-3}$	$5.5 \cdot 10^{-4}$	0.009	700	[15]
Vibrating Electro.	1	o	o	0.047	25 x 25 x 12 $\cdot 10^{-3}$	$3.0 \cdot 10^{-2}$	1.2	2500	[85]
Vibrating Electro.	1	+	o	0.190	25 x 25 x 12 $\cdot 10^{-3}$	$2.0 \cdot 10^{-3}$	0.08	3000	[85]
Unimorph Piezo.	1	o	+	3.0	50 x 10 x 9 $\cdot 10^{-3}$	$1.4 \cdot 10^{-1}$	2.8	140	[18]
Bimorph Piezo.	6	o	+	1.27	44 x – x – $\cdot 10^{-3}$	$3.7 \cdot 10^{-1}$	8.4	200	[7]
Bimorph Piezo.	8	+	+	2.8	45 x – x – $\cdot 10^{-3}$	$1.7 \cdot 10^{-1}$	3.8	200	[32]
Shape Memory Alloy	2	+	+	2.4	30 x – x – $\cdot 10^{-3}$	$3 \cdot 10^{-2}$	1.0	13.6	[52]
RAFA	1	o	o	0.132	20 x 27 x 22 $\cdot 10^{-3}$	$3.2 \cdot 10^{-4}$	0.012	1000	This Work

Act. – Number of Actuators   **M** – Mass   **Dim.** – Dimensions   **BL/s** – Body Lengths per Second   **V** – Operating Voltage

overhead arm, and are lightweight and flexible to minimize impact on robot dynamics. Two high-voltage amplifiers (Trek, PZD700) power the two actuator layers.

4.5.2 Leg Design & Foot Characterization

The robot's leg design is seen in Fig. 4.11, mounted in a friction testing setup consisting of a paper friction pad on a cantilevered rod (k = 0.29 N/m). A known normal force (F_N) is applied to the leg and transverse force (F_T) is increased until the foot slips.

The anisotropic foot Fig. 4.11(b) is inspired by prior spine designs for milli-robot feet [35, 67, 68]. The front and rear legs are constructed of polyimide film (50 μm) with approx. 50 μm long spines. The spines contact the ground at a 45° angle pointing rearward (front legs have a 90° bend above the spines) to ensure anisotropic friction (Fig. 4.11c). Static friction is 1.3x greater for $F_T < 0$, ensuring feet will preferentially slide forward.

4.6 Conclusion

In this chapter we have demonstrated a new bidirectional, thin-film Repulsive-/Attractive-Force electrostatic Actuator (RAFA). The 2-layer RAFA employs a new, optimized electrode geometry for higher force production and is capable of controllably generating both repulsive and attractive forces by varying the applied voltage to each layer. Measured forces up to 156 Pa (38.9 mN, for 2.5 cm^2 electrode area) in repulsion and 352 Pa (88.0 mN) in attraction were generated when operating at 0–1.2 kV.
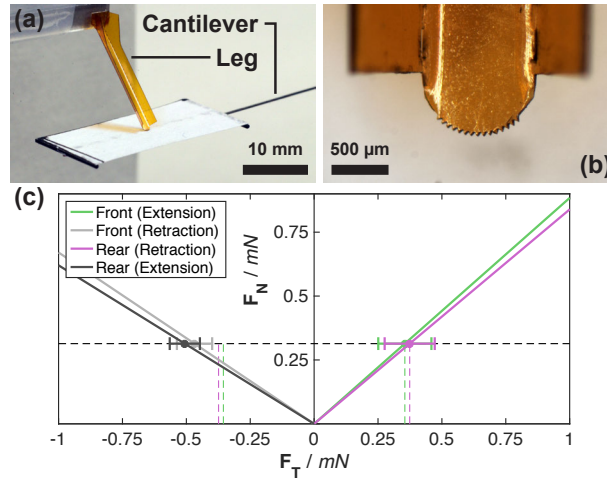
Figure 4.11: Fabricated 5 mg leg on the friction-testing stand (a) with close-up of a rear foot (b). The feet exhibit anisotropic friction (c) by terminating in a circular array of 50 μm spines. The *front foot* will preferentially extend during repulsive-actuation (green) and the *rear foot* will preferentially retract during attractive-actuation (purple). Foot friction is measured with $F_N = mg/4$ (horizontal dashed line) and is lower when legs experience loading in the forward direction (vertical dashed lines, $F_T > 0$). Error bars denote 1σ (n = 6) per foot and F_T direction.

We also demonstrate the RAFAR, a 132 mg milli-robot powered by a RAFA and capable of crawling at 0.32 mm/s (0.012 BL/s) using 1 Hz / 0–1.0 kV bidirectional actuation. A future area of research is to explore a range of control signals (waveforms, voltages, and frequencies) that could provide faster crawling locomotion.

This bidirectional RAFA – capable of controllably generating repulsive- and attractive-forces – is of value to the MEMS and milli-robotics communities alike. Repulsive-force actuators provide inherently open-loop stable actuation with peak force at initial displacements. Attractive-force actuators provide a voltage-controllable restoring force with greater magnitude than a mechanical spring force. As a result, the RAFA is ideal for applications that require electrostatic actuation with greater work-loops than unidirectional actuators (with spring returns), such as the crawling robot demonstrated in this chapter.

Chapter 5

Electrostatic Adhesives for a Flexible Gripper

Content in this chapter was originally published as "An Electrostatic Gripper for Flexible Objects," *IROS 2017* [99].

5.1 Introduction

Over 1,400 operational satellites currently orbit the Earth [119]. All but two – the International Space Station and Hubble Space Telescope – were designed to operate without repair, refueling, or upgrades. Now, NASA's Restore-L [87] and DARPA's RSGS [90] programs are developing robotic spacecraft capable of performing satellite servicing and relocation in order to extend the operational life of these satellites.

Current system architectures from both NASA [28, 29, 87, 116] and DARPA [48, 90, 110, 123] use dexterous robotic arms [17] with a suite of end effectors designed to perform specific jobs, such as cutting lock wire, removing fuel caps, and transferring cryogen or fuel. The manipulation of soft goods – primarily the multi-layer insulation (MLI) blankets that provide thermal and debris shielding for satellites [27] – is one of the most challenging tasks still without a reliable tool. The MLI must be grasped and peeled back to access many elements of the satellites, but it has no clear engagement points and is easily damaged. We believe that a flexible, hybrid electrostatic / gecko-like adhesive gripper – designed to have compliance similar to MLI and attractive engagement in zero-gravity – is ideally suited for this task.

While this chapter focuses primarily on the application of electrostatic and hybrid adhesive grippers to satellite servicing, the same gripping technology can be used in many instances here on Earth, including for industrial robots (pick-and-place or manipulation of food bags, soft goods, etc.) and wall-climbing robots [1, 16, 84, 122].
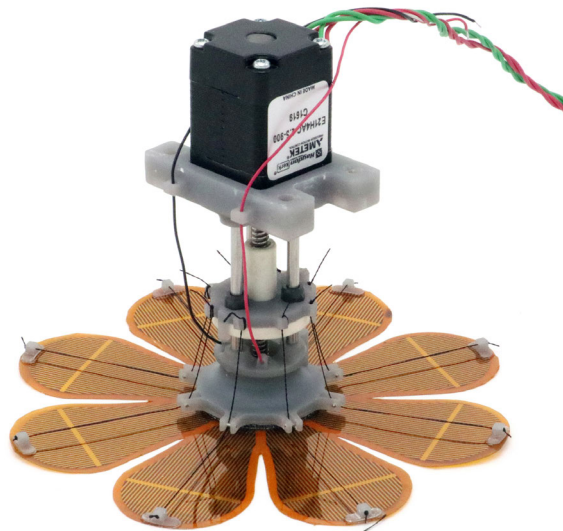
Figure 5.1: Fabricated electrostatic gripper.

5.2   Background

MLI commonly consists of outer / inner covers surrounding 15+ layers of metallized reflectors [27]. These reflectors provide thermal insulation and are each composed of a 7.5 – 130 μm substrate of Kapton (polyimide), Mylar (PET), or Teflon (PTFE) with evaporated aluminum or gold coatings. The films are conductive and readily polarizable, which allows strong engagement by electrostatic adhesives. The covers provide debris and chemical (atomic oxygen and UV) protection, and are composed of Beta cloth (woven PTFE-impregnated fiberglass cloth), reinforced Tedlar (PVF), Kapton, or Teflon. Electrostatic and gecko-like adhesives can controllably generate or remove adhesion in a space environment, making them well-suited to manipulation of MLI, whereas fingered grippers have trouble grasping thin films, magnetic grippers require magnetically susceptible materials, and vacuum grippers require a pressure differential and non-porous surface [73].

Electrostatic adhesives consist of interdigitated electrodes that generate an intense electric field when charged to high voltages [73,84]. Adjacent objects experience surface charging (in electrically conductive materials) or surface polarization (in electrically insulating materials) due to the impinging electric fields, generating an electrostatic attractive force between the objects and adhesive that is proportional to the square of the field strength [73]. Electrostatic adhesives require no direct contact to produce an adhesive force, and thus operate on variable roughness surfaces or across gaps between the adhesive and object [93,95]. Adhesion is controlled by simply turning on / off the applied voltage.

Gecko-like (or fibrillar) adhesives consist of large arrays of fibers, pillars, or wedges that adhere to surfaces through van der Waals forces (atomic-scale matching dipole polarizations that produce an electrostatic attractive force). Gecko adhesives can have directional or

non-directional adhesion, and use flexible fibers with high surface area and high surface conformation to maximize adhesive forces [3]. Adhesion is controlled by applying normal and shear preload forces to engage fibers [101]; low force disengagement is performed by angling / peeling fibers, or removing the preload [63].

Prior work [94–96] demonstrated the ability of hybrid electrostatic / gecko adhesives to generate greater adhesive forces (in shear) on a wider variety of substrates and surface roughnesses than either adhesive technology individually. Adhesive strength on spacecraft films and fabrics shows the advantages of each technology (hybrid / electrostatic / gecko): MLI (15 / 9.5 / 4.5 kPa), Beta cloth (10 / 1.5 / 8 kPa), and Kapton (6.5 / 2.5 / 2 kPa) [95].

Electrostatic adhesive [16, 31, 34, 59] and gecko adhesive [39] grippers have been successfully used in terrestrial robots for controllable grasping of rough, non-flat [105], and soft surfaces [30]. Gecko-adhesive grippers have also been in development for space applications [25, 39, 46, 47, 57, 71, 75]. These current spacecraft-focused designs, however, use rigid grippers that don't readily engage flexible films, and sacrifice adhesive strength by using gecko adhesives alone.

5.3   Adhesive Film Development

The fabricated electrostatic adhesive film is shown in Fig. 5.2 with a magnified view of the electrodes in Fig. 5.3. The fabrication process is illustrated in Fig. 5.4. The adhesive is 10 cm in diameter with 50 cm^2 of active electrostatic adhesive area divided into 8 radially symmetric fingers, each 32.5 mm long with 12.5 mm radius tips.

5.3.1   Design

The electrostatic adhesive is designed to maximize both electrostatic forces and the adhesive's flexibility. This allows the adhesive to conform to non-planar objects or non-developable surfaces like MLI, even as they are flexed.

As introduced in Sec. 5.2, an electrostatic adhesive's interdigitated electrodes produce an attractive force at an object's surface that is directly proportional to the electrode area and to the square of the electric field at the surface interface [73]. Therefore, it is advantageous to maximize both electrode density and electric field intensity through careful design of the adhesive's electrode pattern and construction.

In prior designs [93], interdigitated electrodes were patterned on a single side of a polyimide film and insulated by an epoxy (dielectric strength of 33 $V/\mu m$) [89] or silicone (14-20 $V/\mu m$) [20] bonding layer and a polyimide coverlay. In the new adhesive construction, positive and negative electrodes are patterned on opposite sides of a polyimide film, and insulated by the polyimide substrate itself (240 $V/\mu m$, at 50 μm) [22]. As a result, the maximum electric field – limited by the insulating material's dielectric strength – is increased from 14-33 $V/\mu m$ to 240 $V/\mu m$, and the minimum electrode gap size is reduced from 300 μm to 50 μm. With electrode widths of 300 μm in both cases, this yields a 71% increase in
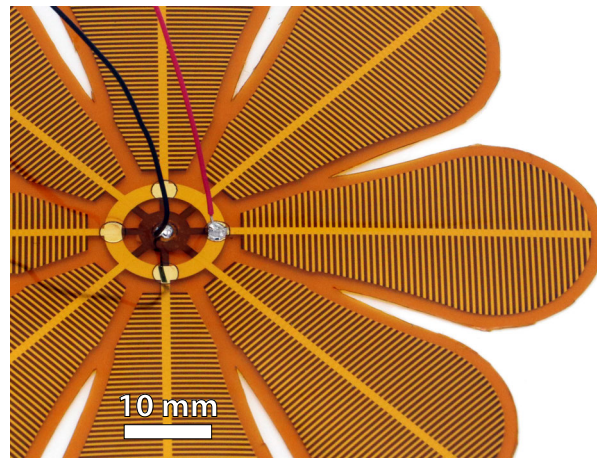
Figure 5.2: Fabricated electrostatic gripper adhesive, with polyimide cover and soldered power wires.
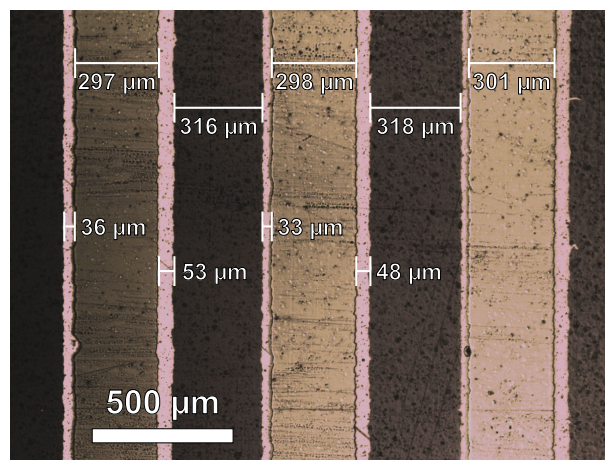
Figure 5.3: Electrodes for the electrostatic gripper adhesive, magnified under an optical microscope. Bright electrodes are on top of / dark electrodes are below the polyimide substrate.

electrode density. This new electrode geometry was optimized for maximum adhesion force using Comsol simulations, as described in [93, 95].

Flexibility is achieved primarily by using thin functional layers: the full electrostatic adhesive composite is only 85 μm thick (see Fig. 5.4e). The polyimide film substrate (50 μm) has patterned electrodes on each surface that are evaporatively deposited metal (360 nm) instead of etched copper-clad laminates (>9 μm) [23]. A cover film (25 μm) insulates only the high-voltage electrode surface; the ground electrodes remain exposed.

Flexibility is further increased by cutting the adhesive into 8 independent fingers. The fingers are radially symmetric, to handle bidirectional shear loads and wrap around curved

objects. The fingers narrow in width from tip (25 mm) to base (13.5 mm), to increase individual torsional flexibility. Bending flexibility of the fingers also allows for a "pull-in effect" during grasping: the electrostatic force can typically overcome the finger stiffness, so fingers are attracted towards an object and adhesion propagates from a contact point across the full area of each finger.

5.3.2 Fabrication

Fabrication of the electrostatic adhesive consists of a multi-layer, additive process, illustrated in Fig. 5.4. The electrostatic adhesive is fabricated on a substrate of 50 μm polyimide film (DuPont, Kapton 200 FPC), which is thermally stabilized and has an adhesion-promoting surface. The substrate is cleaned and treated in a plasma etcher (Tepla, PP300SA) for 10 seconds to further promote metal adhesion. The electrodes are patterned onto the substrate using shadow masks (Micron Laser Technology & PCB Unlimited, 250 μm stainless steel) in an electron-beam evaporator. The electrodes are composed of three metal film layers that are sequentially evaporated: a titanium (30 nm Ti) adhesive layer, a platinum (30 nm Pt) intermediary layer, and a gold (300 nm Au) conductive layer. Separate sequences are used to pattern the two sides of the substrate.

To prevent unintended shorting during operation, a 25 μm polyimide cover (DuPont, Kapton 100 FPC) is laminated over the high-voltage electrodes. For this process, the substrate is first secured to a glass tile. Next, uncured epoxy (Resin Labs, EP1290 Clear) is poured onto the substrate, the cover is placed over the epoxy, and a smooth metal rod is used to roll the epoxy down to a 10 μm film between the two polyimide layers. The composite is then cured at 120°C for 120 minutes. The grounded electrodes are left uncovered to establish common ground with any grasped object.

The gripper fingers are formed using a laser cutter (Epilog, Helix 24) or scalpel to cut the electrode array out of a full composite sheet. Power wires are soldered directly to bus bars for the high-voltage / ground electrodes at the center of the gripper. A via is cut through the polyimide substrate to access the ground electrode, while the cover film has pre-cut holes to directly access the high-voltage electrodes.

Optionally, a gecko-like adhesive – consisting of 60 μm stalks on a 20 μm thick backing – can be patterned onto the electrostatic adhesive to produce a hybrid electrostatic / gecko adhesive, as shown in [95]. To do this, individual gripper fingers are primed with an adhesion promotor (Dow Corning, PR-1200 RTV Prime Coat) and allowed to dry. For each finger, a gecko-like adhesive mold is spin-coated with uncured silicone (Dow Corning, Sylgard 170), and a gripper finger is rolled / flattened over top with a smooth metal rod. The composite is cured again at 65°C for 120 minutes. The fingers are then peeled from the mold, and the hybrid adhesive is complete.
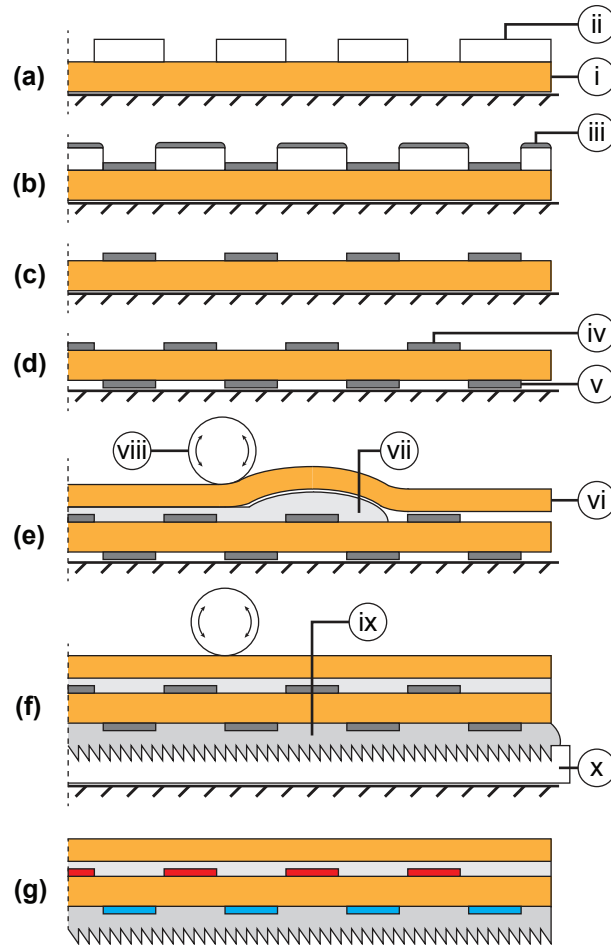
Figure 5.4: Fabrication process: (a) The polyimide film substrate (i) is prepared and the shadow mask (ii) is secured over the film. (b) Layers of Ti / Pt / Au (iii) are evaporated onto the film. (c) The shadow mask is removed. (d) The film is flipped over, the shadow mask is aligned / secured, and the metal layers are evaporated. The resulting substrate contains arrays of positive (iv) and negative (v) electrodes. (e) A polyimide film cover (vi) is laminated over the positive electrodes using an epoxy adhesive (vii), rolled flat with a metal roller (viii). (f) Gecko adhesive is optionally added by rolling the electrostatic adhesive over silicone (ix) in a patterned mold (x) and curing. (g) Finished adhesive.

5.4 Gripper Development

The assembled gripper is shown in Fig. 5.1, and its cross-section is illustrated in Fig. 5.5. The gripper body is 10 *cm* tall and 3.25 *cm* in diameter (at the adhesive mount), with a 10 *cm* diameter adhesive pad.

5.4.1 Design

The gripper is designed to controllably adhere to flexible substrates without preload, maintain adhesion through a wide range of motions / torques / forces, and controllably release with near-zero force. Sec. 5.3.1 highlights the design decisions made for the electrostatic adhesive to ensure sufficient flexibility (for conformation to objects) and adhesive force (for "pull-in" adhesion without preload). A foam spacer between the adhesive and the gripper body provides an intermediate-stiffness connector (20 *kPa* to 25% compression) that transmits torques / loads, maintains the adhesive's flexibility at the connection point, and allows passive bending / rotation that aligns the adhesive to grasped objects.

Controllable disengagement is achieved by reducing the electrostatic adhesion force in two stages: reducing the effective area of the electrostatic adhesive and turning off the electrostatic adhesive. First, the linear actuator draws in tendons attached to the fingers tips of the adhesive, producing a low-force peeling release of the electrostatic adhesive from finger
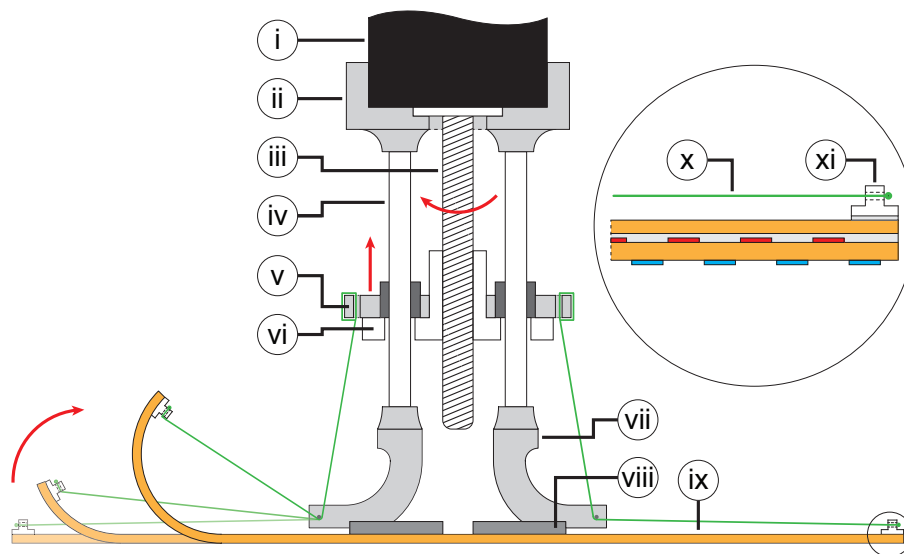
Figure 5.5: Assembled gripper with electrostatic adhesive attached to the gripper body (cross-section shown). Components include: NEMA 8 motor (i) with lead screw shaft (iii) and linear actuator nut (vi), dowel pins (iv), 3D-printed motor mount (ii) / tendon mount (v) / adhesive mount (vii) / tendon terminals (xi), foam spacer (viii), adhesive (ix), and tendon thread (x).

tips to center. Second, the adhesive's electrodes are grounded to switch off the remaining adhesive force and cleanly release the substrate. Simply grounding the electrodes rarely yields a clean release: charge flow from the electrodes induces residual charging in the gripper substrate and grasped object, which can maintain some adhesion. Peeling back the fingers first reduces this residual adhesion.

The peeling action is generated by tendons pulled by a linear actuator (Fig. 5.6). The stepper motor linear actuator is compact and provides linear motion that can simultaneously retract all 8 fingers, is controllable without encoders, and minimizes failure modes (no winding / tangling up of tendons on a spool, no complex transmission, etc.). Tendons maintain the desired finger compliance and can directly control the peel angle of the fingers: routing the tendons through the adhesive mount (small angle) yields reliable peeling from the tip and avoids pulling the entire finger up at once (large angle). Tendons can also integrate easily with future design improvements, such as load-balancing mechanisms [40].

Finally, the gripper is designed to attach easily to a variety of robotic arm end-effector interfaces using separate 3D printed motor mounts (Fig. 5.5-(ii)). Power for the electrodes (high voltage) and stepper motor (low voltage) are routed through strain-reliefs on the motor mount to an external controller that can be secured on the robot arm.
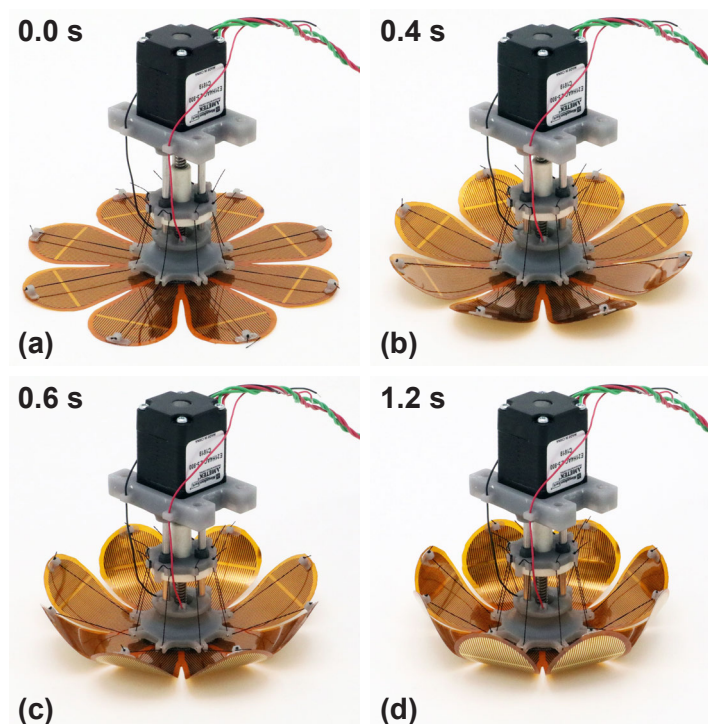
Figure 5.6: Mechanism for gripper engagement / release. A linear actuator controls tension in the tendons, which straightens / curls the gripper fingers in 1.2 *s*.

5.4.2   Fabrication

The gripper is comprised of a linear actuator, compliant spacer, and electrostatic adhesive fingers, as shown in Fig. 5.5. Structural elements of the gripper were 3D printed (FormLabs, Form 2). The linear actuator (Haydon-Kerk, E21H4AC), composed of a NEMA 8 stepper motor, linear actuator nut ($\oslash$ 20 mm), lead screw (40 mm), and housing, is connected to the compliant spacer using double-sided tape (3M, 9474LE). Tendons run from the actuator nut to each finger tip, routed using dowel pins as fast pulleys, and attached to the adhesive petals with a small 3D printed terminus. As the actuator nut is drawn up, these tendons cause the gripper fingers to curl away from a substrate. Reversing the direction of motion allows the fingers to relax to an uncurled state, conforming to the surface to be gripped.

The electrostatic adhesive fingers are controlled by a microcontroller (Arduino, Nano) and a high-voltage amplifier (HVM, UMHV0550). The linear actuator is controlled by a second Arduino Nano and stepper motor controller (Pololu, DRV8825).

5.5   Gripper Characterization

Gripper performance is characterized by measuring the gripper's electrostatic adhesion force to a variety of film substrates at different tensions (Sec. 5.5.1) and by observing the adhesion force during a complete film manipulation sequence (Sec. 5.5.2). The performance of individual gripper fingers using either electrostatic adhesive or hybrid electrostatic / gecko adhesive are also compared (Sec. 5.5.3).

5.5.1   Electrostatic Adhesion of the Gripper

The test setup in Fig. 5.7 is used to quantify gripper adhesion with varying slack in the film (an analog for grasping lightly secured MLI in space). It is comprised of a z-axis stage (Mark 10, ES30) and force gauge (Mark 10, M5-10) onto which the gripper is mounted. A laser-cut baseplate and bracket assembly clamp the film below the gripper. This setup allows us to control the film slack between the two brackets, while ensuring the film is otherwise flat and ripple free. As the film angle (α) increases from additional slack, the ratio of shear (max at $\alpha = 90°$) versus normal ($\alpha = 0°$) loading applied by the gripper adhesive also increases.

The following procedure was repeated 5x for each film material / angle combination: 1) Clamp one end of the film and apply a 50 gf tensile preload to the other. 2) Lower the gripper 3 mm into the film (for consistent preload), apply 3 kV to the electrostatic pad, and wait 10 s for full adhesion. 3) Raise the gripper to the specified film α. 4) Clamp the film's loose end. 5) Raise the gripper to its maximum adhesive load.

Results are shown in Fig. 5.8, with film details in Table 5.1 (for Polyimide[1], Polyimide[2], etc.). The gripper performs best on *Ge*-coated polyimide[1] film – supporting loads from 1.9 N at $\alpha = 0°$ (taut film) to 3.4 N at $\alpha = 7.5°$. Adhesion to MLI increases from 0.73 N ($\alpha = 0°$) to 1.2 N ($\alpha = 6.5°$). Adhesion is stronger on conductive (MLI and Polyimide[1,2]) than on non-conductive materials (Beta Cloth), due to greater surface charging. Adhesion is also higher
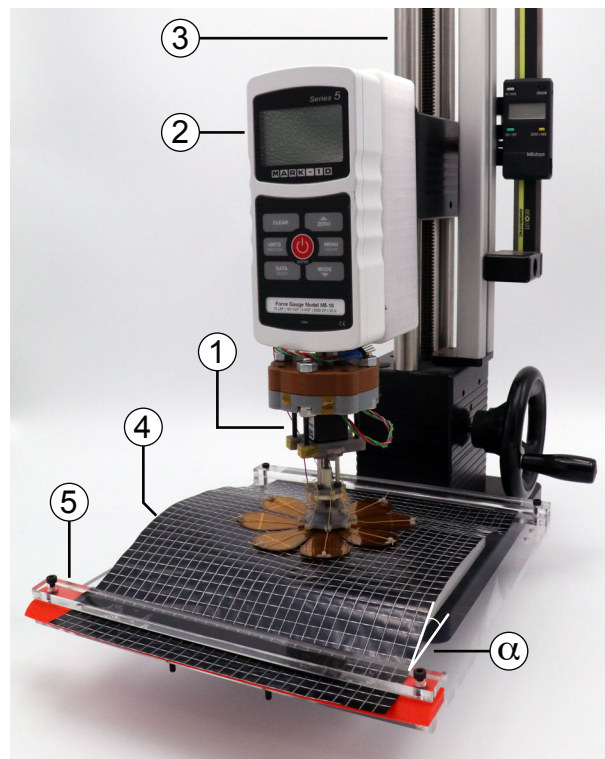
Figure 5.7: Gripper force characterization set-up. The electrostatic gripper (i) is mounted to the force gauge (ii), which slides along the z-axis stage (iii). The film (iv) being tested is secured in a bracket assembly (v) below the gripper.

on smooth (Polyimide[1]) over fiber-reinforced films (Polyimide[2]), due to improved surface conformation and film compliance. Electrostatic adhesives have been shown to support larger shear than normal loads [31, 94]: in Fig. 5.8, MLI and Polyimide[1] demonstrate this trend of increased adhesion at higher α, while Polyimide[2] and Beta Cloth do not. The disparity occurs for films with weak adhesion, as the gripper fingers conform poorly to the film and thus experience peeling separation instead of shear loading at larger α.

5.5.2 Force Profile during Grasping

The gripper force was also measured throughout a sample engagement / manipulation (pull and relax) / release sequence on Polyimide[1] (Fig. 5.9, Table 5.1). This sequence follows steps $(1 - 4)$ in Sec. 5.5.1, followed by: 5) Lower the gripper to its neutral $(0\ N)$ position. 6) Turn off the high voltage supply and wait $10\ s$ for discharge. 7) Retract the fingers using the linear actuator. 8) Raise the gripper away from the film.

Successful manipulation requires that the gripper maintains sufficient gripping force during operation while minimizing the grasping and release forces. We observe stable adhesion at $1.04\ N$ $(0.21\ kPa)$ with a dramatically smaller engagement force of $-0.08\ N$ (8% of peak
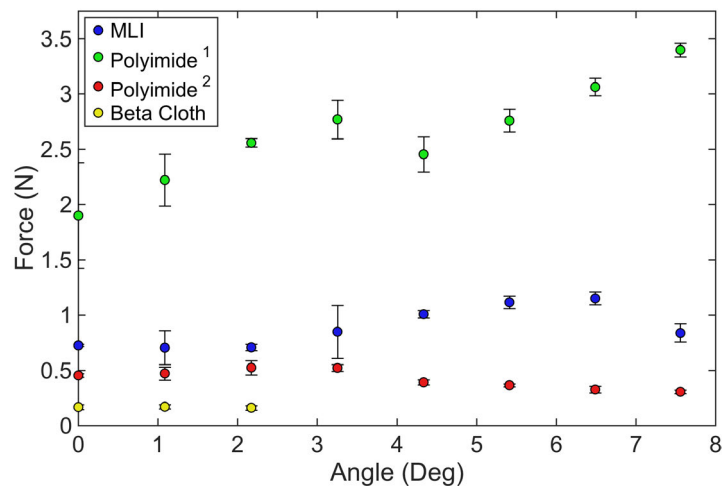
Figure 5.8: Adhesion force of the gripper to flight-qualified films, at a range of engagement angles ($\alpha = 0$–$7.5°$). Adhesive area is 50 cm^2. Polyimide[1,2] are listed in Table 5.1.
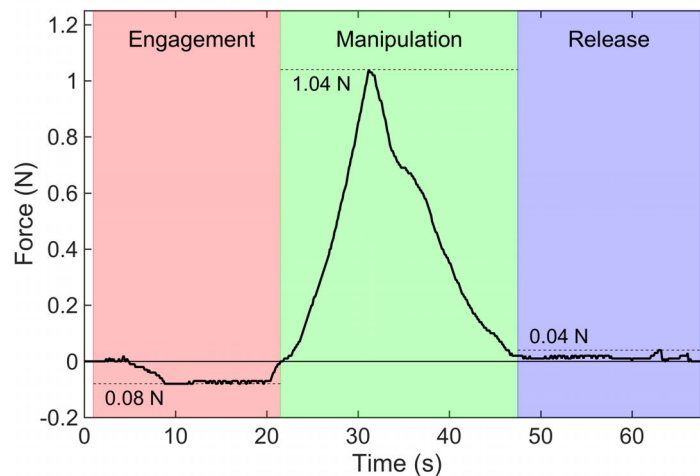
Figure 5.9: Force applied by the gripper on a substrate during a 3-step grasping sequence (engagement, manipulation, and release). The gripper applies an 0.08 N preload force during engagement, a peak adhesion force of 1.04 N during manipulation, and a 0.04 N peel force during release.

load) and disengagement force of 0.04 N (4% of peak load).

5.5.3 Electrostatic & Hybrid Adhesion of a Finger

Individual finger adhesion can be improved using a hybrid adhesive instead of an electrostatic adhesive (Table 5.1). Hybrid adhesive fingers consist of the electrostatic adhesive fingers coated with 60 μm silicone stalks [95]. This work expands on [94, 95] – using a 6-DoF force-torque sensor (ATI, Gamma Transducer) and two linear slides (Velmex, XSlide XN10) – to measure shear adhesion between individual fingers and the film substrates from Sec. 5.5.1. Testing follows the procedure: 1) Position the finger (electrostatic or hybrid adhesive) in contact with the film. 2) Charge to 3 kV, engaging the electrostatic adhesion and preloading the (optional) gecko adhesive. 3) Pull the finger in shear until separation.

Hybrid adhesives provide consistent magnitudes of adhesion – 15.2 – 47.6 kPa (3.1x range) – to flight-qualified materials with varied conductivities and surface textures (Table 5.1), and forces are 2-3x greater than reported in [95]. Electrostatic adhesives have greater variability – 0.29 – 5.04 kPa (18x range). Adding gecko adhesive to electrostatic adhesive fingers increases the absolute adhesion strength to conductive films by 8.5 – 9.5x (MLI, Polyimide[1,2]) and non-conductive films by >30x (Beta Cloth, Polyimide[3]). Note that in the hybrid configuration, the electrostatic adhesive generates the necessary attractive preload force required for the gecko adhesive to engage flexible films, as shown in [95].

5.6 Manipulation Demonstration

As a proof-of-concept, the electrostatic gripper was mounted as the end effector of a 7-DoF robot arm (Rethink Robotics, Baxter) and demonstrated a multi-step manipulation task. The task consisted of grasping a hanging metallized PET film (simulating a MLI blanket in

Table 5.1: Adhesion force (in shear, $\alpha = 90°$) for electrostatic adhesive and hybrid adhesive on flight-qualified films. Adhesive area is 9.45 cm^2. Films can be conductive (Cond.) or fiber-reinforced (Reinf.); adhesion factor of improvement (Factor) from adding gecko adhesive is calculated.

Material	Cond.	Reinf.	Electrostatic N (kPa)	Hybrid N (kPa)	Factor
MLI	+	+	3.83 (4.05)	32.23 (34.1)	8.42x
Polyimide [1]	+	−	4.76 (5.04)	45.00 (47.6)	9.45x
Polyimide [2]	+	+	3.63 (3.84)	30.94 (32.7)	8.52x
Polyimide [3]	−	+	0.37 (0.39)	14.38 (15.2)	39x
Beta Cloth	−	−	0.27 (0.29)	17.37 (18.4)	64x

[1] SSL, Germanium-Coated Kapton Film
[2] Orcon KN-90W, Nomex-Reinforced Kapton (100XC) Film
[3] Orcon KN-93W, Reinforced Kapton MLI Film
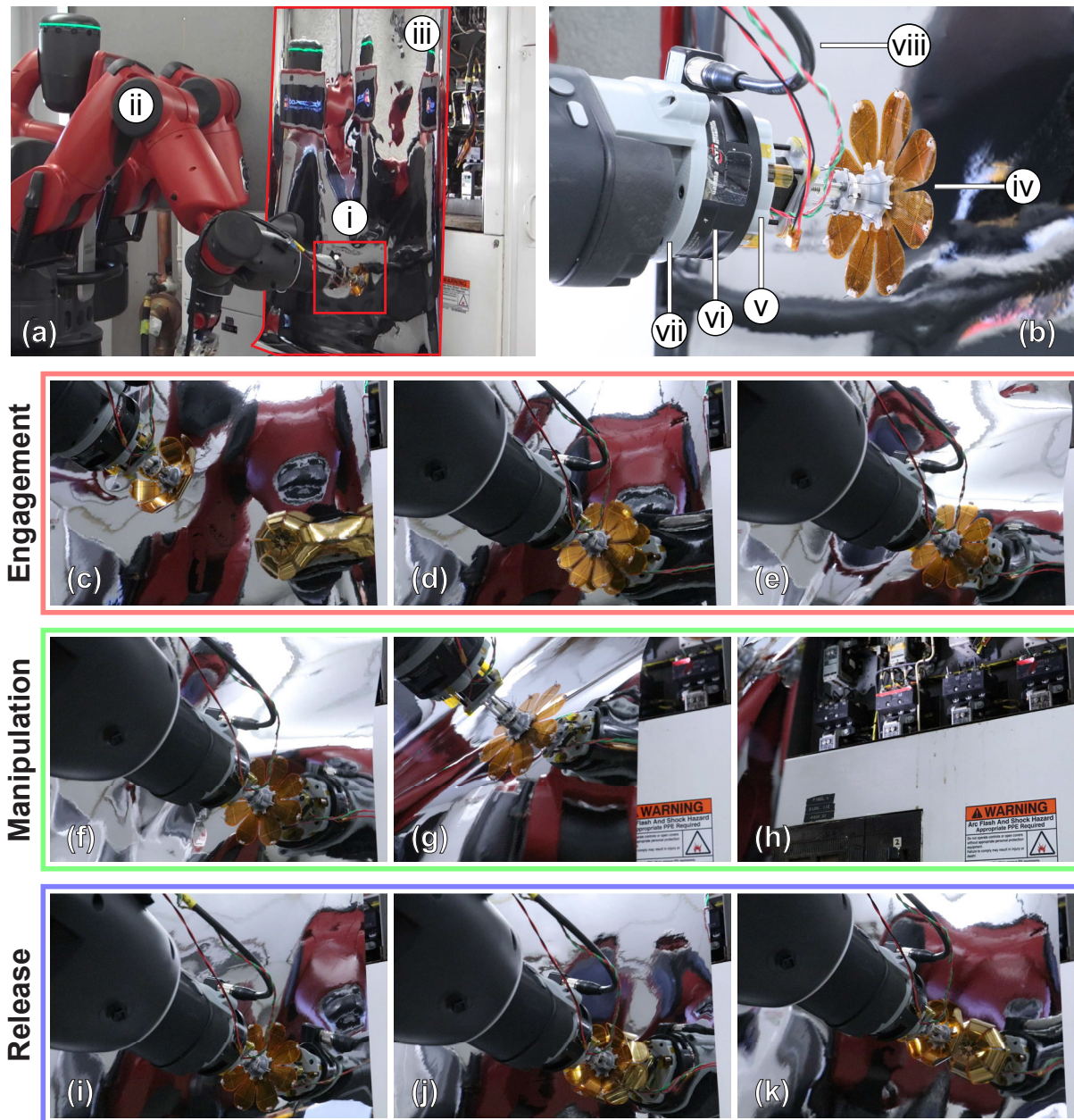
Figure 5.10: Manipulation of a hanging metallized PET film. (a) Gripper (i) mounted to Baxter 7-DoF arm (ii) with adjacent hanging film (iii). (b) Close-up of gripper (iv), with 6-DoF force / torque sensor (vi), 3D-printed adapters (v / vii), and control / data wires (viii). (c)-(e) Engagement: gripper moves to the film while its fingers uncurl. Electrostatic adhesive is charged to $3\,kV$ and attracts / adheres to the film. (f)-(h) Manipulation: robot arm pulls away the film, revealing hidden internal systems. (i)-(k) Release: gripper fingers peel back and the electrostatic adhesive is discharged, to release the film.

microgravity), manipulating the film by peeling it away from an electrical panel and moving it back to its original position (to simulate opening up / moving the film), and releasing the film with near-zero force. This generalized scenario for space-based manipulation tasks can also be applied to terrestrial jobs that handle films, flexible bags, and more. The manipulation sequence is shown in Fig. 5.10 and the accompanying video.

The robot arm followed a sequence of predetermined joint angles during the demonstration, no machine vision or object-tracking was used. A remote operator oversaw each step of the manipulation task: initiating each movement of the robot arm, controlling the high voltage supply (for electrostatic adhesion), and controlling the linear actuator (for finger peeling for disengagement).

The full manipulation sequence is shown in Fig. 5.10, and was successfully performed 10 times. The gripper fully adhered to the hanging film in as little as 2.7 s and an average of 6.3 s ($\sigma = 3.2$ s); it released the film as quickly as 2.6 s and in an average of 5.4 s ($\sigma = 3.6$ s). The end-effector was translated over 0.25 m during the test – note the film buckling during transport in Fig. 5.10g. In instances where the gripper did not complete the task, two main failure modes were identified: incomplete adhesion to the hanging film causing separation when the robot arm began to move, and severe buckling in the film during manipulation causing the film to peel off from the gripper adhesive.

5.7 Conclusion

In conclusion, we have developed a proof-of-concept flexible, electrostatic adhesive gripper capable of being mounted on a robotic arm and manipulating flexible films in simulated micro-gravity. The gripper generates electrostatic attractive forces up to 3.5 N (0.70 kPa) on Ge-coated polyimide films, and 1.2 N on MLI blanket. Individual gripper fingers with electrostatic / hybrid adhesives generated shear pressures up to 5.04 kPa / 47.6 kPa on flight-certified films, respectively. During operation, film grasping occurs quickly (2.7 s to engage and 2.6 s to release) and with minimal force (0.08 N to engage and 0.04 N to release), matching the operational parameters needed for satellite servicing applications.

Future updates to the gripper will include constructing the gripper from flight-qualified materials, modularizing the gripper fingers to increase flexibility and isolate electrical failures, and manufacturing a complete hybrid electrostatic / gecko adhesive gripper. We also plan to integrate force / torque sensors into the gripper, to enable autonomous grasping. Force-based control will allow autonomous identification of gripper engagement, release, and poses that cause film buckling, as well as minimization of peeling forces / torques throughout robot arm trajectories. Future experiments will explore using this type of gripper for object manipulation on Earth (Fig. 5.11), and assisting with MLI blanket cutting and re-sealing tasks, for full thermal blanket "surgery" in space.

Figure 5.11: Prototype gripper with two rectangular hybrid adhesive fingers, grasping and lifting a full soda can (3.6 N).

Chapter 6

Conclusion

In this dissertation, thin-film repulsive-force actuators, repulsive-/attractive-force actuators, and attractive-force adhesives were successfully developed for an array of high-voltage robotics applications.

The repulsive-force electrostatic actuators (RFAs) were successfully redesigned from prior MEMS-scale devices to incorporate novel electrode patterns that improve electrostatic pressure, minimize shorting failure modes, and facilitate meso-scale manufacturing using thin-film processes. Multiple RFA electrode patterns were demonstrated, including: the V1-A/B designs used in MEMS-scale actuators, the V2 design introduced in Chap. 2 [100], and the V2-A optimized design presented in Chap. 4 [98]. The V2-A optimized design generated measured electrostatic pressures up to 156 Pa (1200 V) in comparison to the V1-A design's 3.4 Pa (at 1000 V) – a 46x increase. Multi-layer RFAs were also fabricated for the first time in Chap. 3 [97], and shown to be a viable solution for increasing actuator stroke length, especially in combination with higher operating voltages. The 8-layer RFA stacks generated measured displacements up to 1.55 mm (at 2000 V) in comparison to 2-layer stacks' 0.62 mm (at 1000 V) – a 2.5x increase. 1- and 2-DoF micro-mirrors were also developed, with up to 8.8° angular deflections, 35 Hz bandwidth, and the ability to draw various patterns using a laser dot and open-loop control of 1–4 actuators.

The repulsive-/attractive-force electrostatic actuators (RAFAs) in Chap. 4 [98] were a further refinement of the RFA technology: by using separate control signals for each layer of a 2-layer actuator (with V2-A electrode design), the RAFA was capable generating electrostatic pressures up to 156 Pa (38.9 mN) in repulsion and 352 Pa (88.0 mN) in attraction. This bidirectional RAFA facilitated the creation and operation of an inchworm robot – RAFAR – which utilized the powered extension and retraction phases of the RAFA's work loop to crawl forward at 320 $\mu m/s$ (0.012 BL/s) using anisotropic friction feet.

The attractive-force electrostatic adhesive gripper in Chap. 5 [99] provided an additional application for thin-film electrostatic devices – a flexible, lightweight gripper with controllable adhesion that can operate in space and grasp / manipulate satellite multi-layer insulation (MLI) during repair / refueling missions. The compliant, 8-fingered electrostatic adhesive gripper (10 cm diameter with 50 cm^2 electrode area) generated attractive pressures of up to

700 Pa (3.5 N) on metallized polyimide films and 240 Pa (1.2 N) on MLI. The electrostatic adhesive fingers could also be coated with a film of fibrillar (gecko-like) dry adhesive that increased adhesion by 8–9x (on polarizable films) and over 39x (on non-polarizable films). The gripper controlled the magnitude of adhesion force both electrically – by applying up to 3000 V to the adhesive – and mechanically – by using a linear actuator and cables to simultaneously retract or extend all eight adhesive fingers. A robotic arm, using the gripper as an end-effector, demonstrated multiple grasp, manipulate, and release sequences of a flexible, hanging MLI film, and achieved a NASA Technology Readiness Level 4–5.

6.1 Future Improvements

RFA / RAFA performance – specifically electrostatic pressure, stroke length, and control – can be further improved through a variety of technical refinements, including:

Achieving closed-loop control of actuators. Fabrication of a 2-layer RFA with capacitive-sensing electrodes integrated in the ground-plane surfaces was also briefly explored, in collaboration with L. Jiang. Inter-layer height was reliably measured with a capacitive sensing circuit for unpowered actuators. Remaining work for this project involves testing of powered actuators (for electrical interference, reliability, etc.), and wrapping a closed-loop force or position controller around the system.

Fabricating actuators with thinner electrodes / substrates over larger areas. A number of processes have been explored in this dissertation that can further reduce the electrode and substrate thicknesses, or increase the area over which actuators are fabricated. Screen / ink-jet printing process with conductive inks successfully produce 2-sided actuator layers, with expected printed ink thicknesses $\leq$15 μm depending on ink viscosity, mask thickness, and printer pressure / speed settings (see Sec. A.3), and are also extendable to roll-to-roll printing processes for large-area actuators. Lithographic / shadow-masking process with evaporative deposition of metals (Chap. 5) are more expensive, but produce high-quality electrodes at 100s nm. Composite etching process with thinner materials are also possible, for example Dupont Pyralux AP 7163E consists of 9 μm copper on a 25 μm polyimide substrate (Chap. 4).

Operating actuators at higher voltages. Operation is currently limited by power supply performance, as the actuators use polyimide dielectrics rated for 240–300 MV/m. There has been some evidence of residual static charging at particularly high voltages ($>$2 kV), which can cause unintended attractive electrostatic forces and stiction between RFA / RAFA layers. The charging appears to be localized to either untreated polyimide substrates (i.e. not the polyimide in the pre-laminated Pyralux composites) or thermally-activated sheet adhesive, but further research into the conditions causing layer stiction and methods of abatement (such as plasma treatment [66]) would be useful.

Designing electrodes with higher edge density. Fractal patterns, for example, would maximize fringing fields in a finite area, at the cost of requiring precise inter-layer alignment in the XY-plane.

Further exploring optimal electrode designs in simulation and practice. There are indications (in simulation) that solid ground planes might generate the highest repulsive forces in the V2-A design ($L_N = Pitch$, $L_P < L_N$), and would be another simple design to fabricate and measure. Such an electrode pattern could also be easily adapted for use in a multi-layer actuator, where each layer would contain a solid ground plane sandwiched between two dielectrics and two additional patterned electrodes (i.e. 3 electrodes per layer).

Further exploring suspension designs for multi-layer actuators. The multi-layer actuators in Chap. 3 use cantilever spring suspensions that experience diminishing improvements in actuator stroke length as the number of layers increases. Exploring other spring suspension designs for many layers in series (e.g. the folded spring designs in Chap. 2, 4) could overcome this limitation.

6.2 Future Applications

RFA / RAFA applications have only begun to be investigated after six years of research. However, the development of reliable electrode designs (for higher-force RFAs) and fabrication processes (for both iterative design and bulk production) has laid the groundwork for a number of future projects:

Lightweight, thin-film milli-robots, with integrated electrostatic actuation and adhesion. These robots would be fabricated as a single planar composite (SCM) that integrates all circuitry, actuation regions, and adhesive pads into the robot body. Such a SCM robot would pack and transport flat, then fold up and deploy when needed. Such a design would be useful for micro-gravity / space applications, including: robot swarms for monitoring the outside of a satellite or space station, dispersed or reconfigurable sensing, inspecting solar panels, and more.

Actuator arrays for cell assays. RFAs also generate controllable pressures at the ideal magnitude and frequency ranges for mechanical stimulation of cells. Low-cost actuator arrays can be integrated into petri dishes for conducting cellular assays with a variety of tunable mechanical stimulation parameters (loading profile, frequency, etc.). L. Jiang has plans to build and test petri dishes with integrated actuators in the near future.

Large-area actuators / sensors. Long-term research can focus on developing large-area, multi-segmented actuators or pressure sensors that can be applied as thin-film coatings to

airplanes (wings) or buildings (windows / walls). The actuator arrays can modulate airflow to reduce turbulence over wings, or control film transparency to reflect / transmit light through windows. The sensors can measure wind pressure at many points across an aircraft wing during normal operation, while current technology (static pressure tubes) restrict measurements to wing segments in wind tunnels. Commercial production of these devices would be facilitated by using certain fabrication processes – flex-circuit etching (Sec. A.1.2) and screen-printing (Sec. A.3) – explored in this dissertation.

Bibliography

[1]   E. Ackerman, "Electrostatics: Good for Robot Grippers, and Lots More," *IEEE Spectrum*, 2014.

[2]   D. Aukes, S. Kim, P. Garcia, A. Edsinger, and M. R. Cutkosky, "Selectively compliant underactuated hand for mobile manipulation," in *IEEE ICRA*, may 2012, pp. 2824–2829.

[3]   K. Autumn, A. Dittmore, D. Santos, M. Spenko, and M. Cutkosky, "Frictional adhesion: a new angle on gecko attachment," *Journal of Experimental Biology*, vol. 209, no. 18, pp. 3569–3579, 2006.

[4]   S. S. Baek and R. S. Fearing, "Flight forces and altitude regulation of 12 gram I-Bird," in *IEEE BioRob*, 2010, pp. 454–460.

[5]   S. S. Baek, F. L. Garcia Bermudez, and R. S. Fearing, "Flight control for target seeking by 13 gram ornithopter," in *IEEE IROS*, 2011, pp. 2674–2681.

[6]   A. T. Baisch and R. J. Wood, "Design and Fabrication of the Harvard Ambulatory Micro-Robot," in *Robotics Research*, C. Pradalier, R. Siegwart, and G. Hirzinger, Eds. Berlin, Heidelberg: Springer, 2011, vol. 70, no. STAR, pp. 715–730.

[7]   ——, "Pop-up assembly of a quadrupedal ambulatory MicroRobot," in *IEEE IROS*, 2013, pp. 1518–1524.

[8]   J. Batterson, "Second order finite difference schemes for non-uniform grid spacing," Auburn University, Tech. Rep., 2014.

[9]   P. Birkmeyer, K. Peterson, and R. S. Fearing, "DASH: A dynamic 16g hexapedal robot," in *IEEE/RSJ IROS*, 2009, pp. 2683–2689.

[10] P. Birkmeyer, A. G. Gillies, and R. S. Fearing, "Dynamic climbing of near-vertical smooth surfaces," in *IEEE/RSJ IROS*, 2012, pp. 286–292.

[11] S. Bobbio, M. Kellam, B. Dudley, S. Goodwin-Johansson, S. Jones, J. Jacobson, F. Tranjan, and T. DuBois, "Integrated force arrays," in *IEEE MEMS*, 1993, p. 149.

[12] A. Buchan, "Towards Cooperative SLAM for Low-Cost Biomimetic Robots," Ph.D. dissertation, University of California, Berkeley, 2017.

[13] C. S. Casarez and R. S. Fearing, "Step climbing cooperation primitives for legged robots with a reversible connection," in *IEEE ICRA*, 2016, pp. 3791–3798.

[14] ——, "Dynamic terrestrial self-righting with a minimal tail," in *IEEE IROS*, 2017, pp. 314–321.

[15] A. S. Chen, H. Zhu, Y. Li, L. Hu, and S. Bergbreiter, "A paper-based electrostatic zipper actuator for printable robots," in *IEEE ICRA*, 2014, p. 5038.

[16] R. Chen, R. Liu, J. Chen, and J. Zhang, "A gecko inspired wall-climbing robot based on electrostatic adhesion mechanism," in *IEEE ROBIO*, 2013, pp. 396–401.

[17] T. Debus and S. Dougherty, "Overview and Performance of the Front-End Robotics Enabling Near-Term Demonstration (FREND) Robotic Arm," *AIAA Aero. Conf.*, 2009.

[18] A. G. Dharmawan, H. H. Hariri, S. Foong, G. S. Soh, and K. L. Wood, "Steerable miniature legged robot driven by a single piezoelectric bending unimorph actuator," in *IEEE ICRA*, 2017, pp. 6008–6013.

[19] B. Donald, C. Levey, C. McGray, I. Paprotny, and D. Rus, "An Untethered, Electrostatic, Globally Controllable MEMS Micro-Robot," *J. Microelectromech. Syst.*, vol. 15, no. 1, pp. 1–15, 2006.

[20] Dow Corning, "Sylgard 170 Silicone Elastomer," Tech. Rep., 2015.

[21] M. Duck, "Surface charging and its prevention," in *The Behavior of Systems in the Space Environment*, R. N. DeWitt, D. Duston, and A. K. Hyder, Eds. Dordrecht: Springer Netherlands, 1993, pp. 867–872.

[22] DuPont, "DuPont Kapton FPC," Tech. Rep., 2006.

[23] ——, "DuPont Kapton ®," Tech. Rep., 2012.

[24] ——, "DuPont Pyralux AP," Tech. Rep., 2016.

[25] M. A. Estrada, B. Hockman, A. Bylard, E. W. Hawkes, M. R. Cutkosky, and M. Pavone, "Free-flyer acquisition of spinning objects with gecko-inspired adhesives," in *IEEE ICRA*, 2016, p. 4907.

[26] D. Fabiani, G. C. Montanari, A. Cavallini, and G. Mazzanti, "Relation between space charge accumulation and partial discharge activity in enameled wires under PWM-like voltage waveforms," *IEEE Trans. Dielectr. Electr. Insul.*, vol. 11, no. 3, pp. 393–405, 2004.

[27] M. M. Finckenor and D. Dooling, "Multilayer Insulation Material Guidelines," NASA, Tech. Rep., 1999.

[28] A. Flores-Abad, O. Ma, K. Pham, and S. Ulrich, "A review of space robotics technologies for on-orbit servicing," *Progress in Aerospace Sciences*, vol. 68, pp. 1–26, 2014.

[29] G. Gefke, A. Janas, R. Chiei, M. Sammons, and B. B. Reed, "Advances in Robotic Servicing Technology Development," in *AIAA SPACE*, 2015, p. 4426.

[30] J. Germann, M. Dommer, R. Pericet-Camara, and D. Floreano, "Active Connection Mechanism for Soft Modular Robots," *Advanced Robotics*, vol. 26, no. 7, pp. 785–798, 2012.

[31] J. Germann, B. Schubert, and D. Floreano, "Stretchable electroadhesion for soft robots," in *IEEE IROS*, 2014, pp. 3933–3938.

[32] B. Goldberg, R. Zufferey, N. Doshi, E. F. Helbling, M. Kovac, R. J. Wood, and G. Whittredge, "Power and Control Autonomy for High-Speed Locomotion With an Insect-Scale Legged Robot," *IEEE RA-L*, vol. 3, no. 2, pp. 987–993, 2018.

[33] S. H. Goodwin-Johansson, S. M. Bobbio, C. Bartlett, N. Eleyan, J. Jacobson, J. E. Mancusi, L. Yadon, C. Ball, T. D. DuBois, W. D. Palmer, D. G. Vellenga, and F. M. Tranjan, "Measured forces and displacements of integrated force arrays," *Proc. SPIE*, vol. 2642, p. 52, 1995.

[34] M. A. Graule, P. Chirarattananon, S. B. Fuller, N. T. Jafferis, K. Y. Ma, M. Spenko, R. Kornbluh, and R. J. Wood, "Perching and takeoff of a robotic insect on overhangs using switchable electrostatic adhesion," *Science*, vol. 352, no. 6288, pp. 978 – 982, 2016.

[35] D. W. Haldane, C. Casarez, J. Karras, J. Lee, C. Li, A. Pullin, E. Schaler, D. Yun, A. Javey, and R. S. Fearing, "Integrated manufacture of exoskeleton and sensing for folded millirobots," *J. Mech. Robot.*, vol. 7, no. 2, p. 19, 2015.

[36] D. W. Haldane and R. S. Fearing, "Running beyond the bio-inspired regime," in *IEEE ICRA*, 2015, pp. 4539–4546.

[37] D. W. Haldane, K. C. Peterson, F. L. Garcia Bermudez, and R. S. Fearing, "Animal-inspired design and aerodynamic stabilization of a hexapedal millirobot," in *IEEE ICRA*, 2013, pp. 3279–3286.

[38] M. M. Hamedi, V. E. Campbell, P. Rothemund, F. Güder, D. C. Christodouleas, J.-F. Bloch, and G. M. Whitesides, "Electrically activated paper actuators," *Adv. Funct. Mater.*, vol. 26, no. 15, pp. 2446–2453, 2016.

[39] E. Hawkes, D. Christensen, E. Eason, M. Estrada, M. Heverly, E. Hilgemann, M. Pope, A. Parness, and M. Cutkosky, "Dynamic Surface Grasping with Directional Adhesion," *IEEE/RSJ IROS*, 2013.

[40] E. W. Hawkes, E. V. Eason, D. L. Christensen, and M. R. Cutkosky, "Human climbing with efficiently scaled gecko-inspired dry adhesives," *J. R. Soc. Interface*, vol. 12, no. 102, 2014.

[41] S. He and R. Ben Mrad, "Large-stroke microelectrostatic actuators for vertical translation of micromirrors used in adaptive optics," *IEEE Trans. Ind. Electron.*, vol. 52, no. 4, pp. 974–983, 2005.

[42] ——, "Performance assessment of a multi-level repulsive-force out-of-plane microelectrostatic actuator," *Can. J. Elect. Comput. Eng.*, vol. 31, no. 2, pp. 71–75, 2006.

[43] ——, "Design, modeling, and demonstration of a MEMS repulsive-force out-of-plane electrostatic micro actuator," *J. Microelectromech. Syst.*, vol. 17, no. 3, pp. 532–547, 2008.

[44] S. He, R. Ben Mrad, and J. S. Chang, "Development of a high-performance microelectrostatic repulsive-force rotation actuator," *J. Microelectromech. Syst.*, vol. 19, no. 3, pp. 561–569, 2010.

[45] S. He, R. Ben Mrad, and J. Chong, "Repulsive-force out-of-plane large stroke translation micro electrostatic actuator," *J. Micromech. Microeng.*, vol. 21, no. 7, p. 075002, 2011.

[46] M. Henrey, J. Tellez, K. Wormnes, L. Pambaguian, and C. Menon, "Sticking in Space: Manufacturing Dry Adhesives and Testing Their Performance in Space Environments," *ASTRA*, 2013.

[47] M. Henrey, J. P. D. Téllez, K. Wormnes, L. Pambaguian, and C. Menon, "Towards the use of mushroom-capped dry adhesives in outer space: Effects of low pressure and temperature on adhesion strength," *Aerospace Sci. and Tech.*, vol. 29, no. 1, pp. 185–190, 2013.

[48] G. Henshaw and B. Kelm, "DARPA Phoenix: Overview and Risk Reduction Plans," p. 20, 2014.

[49] K. L. Hoffman and R. J. Wood, "Passive undulatory gaits enhance walking in a myriapod millirobot," in *IEEE IROS*, vol. 2, 2011, pp. 1479–1486.

[50] A. M. Hoover, S. Burden, X. Y. Fu, S. S. Sastry, and R. S. Fearing, "Bio-inspired design and dynamic maneuverability of a minimally actuated six-legged robot," *IEEE/RAS Bio. Rob.*, p. 869, 2010.

[51] A. M. Hoover and R. S. Fearing, "Fast scale prototyping for folded millirobots," in *IEEE ICRA*, 2008, p. 886.

[52] A. M. Hoover, E. Steltz, and R. S. Fearing, "RoACH: An autonomous 2.4 g crawling hexapod robot," *IEEE IROS*, pp. 26–33, 2008.

[53] I. Hunter and S. Lafontaine, "A comparison of muscle with artificial actuators," in *IEEE Solid-State Sens. Actuators*, 1992, pp. 178–185.

[54] E. Husain and R. S. Nema, "Analysis of Paschen curves for Air, N2, and SF6 using the Townsend breakdown equation," *IEEE Trans. Electrical Insulation*, vol. EI-17, no. 4, pp. 350–353, 1982.

[55] M. Ito and K. Saneyoshi, "Development of large-scale stacked-type electrostatic actuators for use as artificial muscles," *Adv. Robotics*, vol. 1864, pp. 1–9, 2014.

[56] N. T. Jafferis, M. Lok, N. Winey, G.-Y. Wei, and R. J. Wood, "Multilayer laminated piezoelectric bending actuators: design and manufacturing for optimum power density and efficiency," *Smart Mater. Struct.*, vol. 25, no. 5, p. 055033, 2016.

[57] H. Jiang, E. W. Hawkes, V. Arutyunov, J. Tims, C. Fuller, J. P. King, C. Seubert, H. L. Chang, A. Parness, and M. R. Cutkosky, "Scaling controllable adhesives to grapple floating objects in space," in *IEEE ICRA*, vol. 4545, no. June, 2015, pp. 2828–2835.

[58] R. C. Julian, C. J. Rose, H. Hu, and R. S. Fearing, "Cooperative control and modeling for narrow passage traversal with an ornithopter MAV and lightweight ground station," in *AA-MAS*, 2013, pp. 103–110.

[59] A. Kalantari, K. Mahajan, D. Ruffatto, and M. Spenko, "Autonomous perching and take-off on vertical walls for a quadrotor micro air vehicle," in *IEEE ICRA*, 2015, pp. 4669–4674.

[60] M. Karpelson and R. J. Wood, "A review of actuation and power electronics options for flapping-wing robotic insects," in *IEEE ICRA*, 2008, pp. 779–786.

[61] N. Kellaris, V. Gopaluni Venkata, G. M. Smith, S. K. Mitchell, and C. Keplinger, "Peano-HASEL actuators: Muscle-mimetic, electrohydraulic transducers that linearly contract on activation," *Science Robotics*, vol. 3, no. 14, p. eaar3276, 2018.

[62] Keng Peng Tee, S. Ge, and F. Eng Hock Tay, "Adaptive Control of Electrostatic Microactuators With Bidirectional Drive," *IEEE Trans. Control Syst. Technol*, vol. 17, no. 2, pp. 340–352, 2009.

[63] S. Kim, M. Spenko, S. Trujillo, B. Heyneman, D. Santos, and M. R. Cutkoskly, "Smooth Vertical Surface Climbing With Directional Adhesion," *IEEE Trans. Robot.*, vol. 24, no. 1, pp. 65–74, 2008.

[64] N. J. Kohut, A. M. Hoover, K. Y. Ma, S. S. Baek, and R. S. Fearing, "MEDIC: A legged millirobot utilizing novel obstacle traversal," in *IEEE ICRA*, 2011, p. 802.

[65] T. Lebey, P. Castelan, G. Montanari, and I. Ghinello, "Influence of PWM-type voltage waveforms on reliability of machine insulation system," in *IEEE Int. Conf. on Harmonics and Quality of Power*, vol. 2, 1998, pp. 994–998.

[66] J. H. Lee and H. C. Jeong, "Removal of static electricity on polyimide film surface by O2 or Ar cold plasma etching," *Fibers and Polymers*, vol. 5, no. 2, pp. 151–155, 2004.

[67] J. Lee, R. Fearing, and K.-J. Cho, "Compound Foot for Increased Millirobot Jumping Ability," in *CLAWAR*, 2016, pp. 1–8.

[68] J. S. Lee and R. S. Fearing, "Anisotropic collapsible leg spines for increased millirobot traction," in *IEEE ICRA*, 2015, pp. 4547–4553.

[69] K. Y. Ma, P. Chirarattananon, S. B. Fuller, and R. J. Wood, "Controlled flight of a biologically inspired, insect-scale robot." *Science*, vol. 340, no. 6132, pp. 603–7, 2013.

[70] K. Meijer, M. S. Rosenthal, and R. J. Full, "Muscle-like actuators? A comparison between three electroactive polymers," *Proc. SPIE*, vol. 4329, p. 7, 2001.

[71] C. Menon, M. Murphy, F. Angrilli, and M. Sitti, "WaalBots for Space applications," in *55th IAC Conference, Vancouver, Canada*, 2004.

[72] K. Minami, S. Kawamura, and M. Esashi, "Fabrication of distributed electrostatic micro actuator (DEMA)," *J. Microelectromech. Syst.*, vol. 2, no. 3, pp. 121–127, 1993.

[73] G. J. Monkman, "An Analysis of Astrictive Prehension," *The International Journal of Robotics Research*, vol. 16, no. 1, pp. 1–10, 1997.

[74] T. Niino, S. Egawa, and T. Higuchi, "High-power and high-efficiency electrostatic actuator," in *IEEE MEMS*, 1993, pp. 236–241.

[75] A. Parness, M. Heverly, E. Hilgemann, D. Copel, N. Wettels, T. Hilgendorf, V. White, and B. Kennedy, "ON-OFF Adhesive Grippers for Earth-Orbit," *AIAA Space*, 2013.

[76] R. Pelrine, R. Kornbluh, Q. Pei, and J. Joseph, "High-speed electrically actuated elastomers with strain greater than 100%," *Science*, vol. 287, no. 5454, pp. 836–839, feb 2000.

[77] R. E. Pelrine, R. D. Kornbluh, and J. P. Joseph, "Electrostriction of polymer dielectrics with compliant electrodes as a means of actuation," *Sens. Actuators. A Phys.*, vol. 64, no. 1, pp. 77–85, 1998.

[78] I. Penskiy and S. Bergbreiter, "Optimized electrostatic inchworm motors using a flexible driving arm," *J. Micromech. Microeng.*, vol. 23, no. 1, p. 015018, 2013.

[79] K. Peterson, P. Birkmeyer, R. Dudley, and R. S. Fearing, "A wing-assisted running robot and implications for avian flight evolution," *Bioinspir. Biomim.*, vol. 6, no. 4, p. 046008, 2011.

[80] K. Peterson and R. S. Fearing, "Experimental dynamics of wing assisted running for a bipedal ornithopter," in *IEEE IROS*, 2011, pp. 5080–5086.

[81] R. S. Pierre and S. Bergbreiter, "Gait Exploration of Sub-2 g Robots Using Magnetic Actuation," *IEEE RA-L*, vol. 2, no. 1, pp. 34–40, 2017.

[82] K. Pister, M. Judy, S. Burgett, and R. Fearing, "Microfabricated hinges," *Sens. Actuators. A Phys.*, vol. 33, no. 3, p. 249, 1992.

[83] J.-S. Plante and S. Dubowsky, "On the performance mechanisms of Dielectric Elastomer Actuators," *Sens. Actuators. A Phys.*, vol. 137, no. 1, pp. 96–109, jun 2007.

[84] H. Prahlad, R. Pelrine, S. Stanford, J. Marlow, and R. D. Kornbluh, "Electroadhesive robots—wall climbing robots enabled by a novel, robust, and electrically controllable adhesion technology," *IEEE Robot. Autom.*, 2008.

[85] M. Qi, Y. Zhu, Z. Liu, X. Zhang, X. Yan, and L. Lin, "A fast-moving electrostatic crawling insect," in *MEMS*, 2017, p. 761.

[86] J. Qu, J. Choi, and K. Oldham, "Dynamic Structural and Contact Modeling for a Silicon Hexapod Microrobot," *J. Mech. Robot.*, vol. 9, 2017.

[87] B. B. Reed, R. C. Smith, B. J. Naasz, J. F. Pellegrino, and C. E. Bacon, "Restore-L Servicing Mission," in *AIAA SPACE*, 2016, p. 5478.

[88] H. Ren, W. Wang, F. Tao, and J. Yao, "A Bi-Directional Out-of-Plane Actuator by Electrostatic Force," *Micromachines*, vol. 4, no. 4, pp. 431–443, 2013.

[89] ResinLabs, "EP1290 Epoxy Adhesive," Tech. Rep., 2015.

[90] G. Roesler, "Robotic Servicing of Geosynchronous Satellites," 2016.

[91] C. J. Rose, P. Mahmoudieh, and R. S. Fearing, "Coordinated launching of an ornithopter with a hexapedal robot," in *IEEE ICRA*, 2015, pp. 4029–4035.

[92] ——, "Modeling and control of an ornithopter for diving," in *IEEE IROS*, 2016, pp. 957–964.

[93] D. Ruffatto, "Hybrid electrostatic and micro-structured adhesives for robotic applications," Ph.D. dissertation, Illinois Institute of Technology, 2015.

[94] D. Ruffatto, D. Beganovic, A. Parness, and M. Spenko, "Experimental results of a controllable electrostatic/gecko-like adhesive on space materials," in *IEEE Aero. Conf.*, 2014, pp. 1–7.

[95]   D. Ruffatto, A. Parness, and M. Spenko, "Improving controllable adhesion on both rough and smooth surfaces with a hybrid electrostatic/gecko-like adhesive," *J. R. Soc. Interface*, vol. 11, no. 93, 2014.

[96]   D. Ruffatto, J. Shah, and M. Spenko, "Optimization and experimental validation of electrostatic adhesive geometry," in *IEEE Aero. Conf.*, 2013, pp. 1–8.

[97]   E. W. Schaler, L. Jiang, and R. S. Fearing, "Multi-Layer, Thin-Film Repulsive-Force Electrostatic Actuators for a 2-DoF Micro-Mirror," in *Actuators 2018 (to appear)*, Bremen, 2018, p. 4.

[98]   E. W. Schaler, L. Jiang, C. Lee, and R. S. Fearing, "Bidirectional, Thin-Film Repulsive-/Attractive-Force Electrostatic Actuators for a Crawling Milli-Robot," in *MARSS 2018 (to appear)*, 2018, pp. 1–8.

[99]   E. W. Schaler, D. Ruffatto III, P. Glick, V. White, and A. Parness, "An Electrostatic Gripper for Flexible Objects," in *IEEE IROS*, 2017, pp. 1172–1179.

[100] E. W. Schaler, T. I. Zohdi, and R. S. Fearing, "Thin-film repulsive-force electrostatic actuators," *Sens. Actuators. A Phys.*, vol. 270, pp. 252–261, 2018.

[101] B. Schubert, J. Lee, C. Majidi, and R. S. Fearing, "Sliding-induced adhesion of stiff polymer microfibre arrays. II. Microscale behaviour," *J. R. Soc. Interface*, vol. 5, no. 25, pp. 845–853, aug 2008.

[102] Z. Shen, Y. Liu, J. Zhao, X. Tang, and W. Chen, "Design and Experiment of a Small Legged Robot Operated by the Resonant Vibrations of Cantilever Beams," *IEEE Access*, vol. 5, pp. 8451–8458, 2017.

[103] S. Shian, K. Bertoldi, and D. R. Clarke, "Dielectric elastomer based "grippers" for soft robotics," *Adv. Mater.*, vol. 27, no. 43, p. 6814, 2015.

[104] H. Shigemune, S. Maeda, V. Cacucciolo, Y. Iwata, E. Iwase, S. Hashimoto, and S. Sugano, "Printed paper robot driven by electrostatic actuator," *IEEE Robot. Autom. Lett.*, vol. 2, no. 2, p. 1001, 2017.

[105] J. Shintake, S. Rosset, B. Schubert, D. Floreano, and H. Shea, "Versatile soft grippers with intrinsic electroadhesion based on multifunctional polymer actuators," *Adv. Mater.*, vol. 28, no. 2, pp. 231–238, 2016.

[106] P. Slade and E. Taylor, "Electrical breakdown in atmospheric air between closely spaced (0.2 μm-40 μm) electrical contacts," *IEEE Trans. Comp. Pack. Tech.*, vol. 25, no. 3, pp. 390–396, 2002.

[107] P. S. Sreetharan, J. P. Whitney, M. D. Strauss, and R. J. Wood, "Monolithic fabrication of millimeter-scale machines," *J. Micromech. Microeng.*, vol. 22, no. 5, p. 055027, 2012.

[108] E. Steltz, S. Avadhanula, and R. S. Fearing, "High lift force with 275 Hz wing beat in MFI," in *IEEE/RSJ IROS*, 2007, pp. 3987–3992.

[109] E. Steltz, "Optical position sensing for characterization of the micromechanical flying insect," M.S. thesis, University of California, Berkeley, 2006.

[110] B. R. Sullivan, B. Kelm, G. Roesler, and C. G. Henshaw, "Robotic Satellite Servicer Concept: On-Demand Capabilities in GEO," in *AIAA SPACE*, 2015, p. 4664.

[111] T. Takahashi, K. Takei, A. G. Gillies, R. S. Fearing, and A. Javey, "Carbon nanotube active-matrix backplanes for conformal electronics and sensors," *Nano Letters*, vol. 11, no. 12, p. 5408, dec 2011.

[112] W. C. Tang, "Electrostatic comb drive for resonant sensor and actuator applications," Ph.D. dissertation, University of California, Berkeley, 1990.

[113] W. C. Tang, M. G. Lim, and R. T. Howe, "Electrostatic comb drive levitation and control method," *J. Microelectromech. Syst.*, vol. 1, no. 4, pp. 170–178, 1992.

[114] W. C. Tang, T.-C. Nguyen, and R. Howe, "Laterally driven polysilicon resonant microstructures," in *IEEE MEMS*, vol. 20, 1989, pp. 53–59.

[115] Texas Instruments, "DMD 101: Introduction to Digital Micromirror Device (DMD)," Tech. Rep., 2013.

[116] R. L. Ticker, F. Cepollina, and B. B. Reed, "NASA's In-Space Robotic Servicing," in *AIAA SPACE*, 2015, p. 4644.

[117] M. T. Tolley, S. M. Felton, S. Miyashita, D. Aukes, D. Rus, and R. J. Wood, "Self-folding origami: shape memory composites activated by uniform heating," *Smart Mater. Struct.*, vol. 23, no. 9, p. 094006, 2014.

[118] S. Towfighian, S. He, and R. Ben Mrad, "A low voltage electrostatic micro actuator for large out-of-plane displacement," in *ASME IDETC/CIE*, 2014, pp. 1–7.

[119] Union of Concerned Scientists, "UCS Satellite Database," 2016.

[120] D. Verdin, "Electrostatic discharging behaviour of Kapton irradiated with electrons," *Spacecraft Charging Technology*, pp. 96–114, 1981.

[121] D. Vogtmann, R. St Pierre, and S. Bergbreiter, "A 25 mg magnetically actuated microrobot walking at > 5 body lengths/sec," in *IEEE MEMS*, 2017, pp. 179–182.

[122] H. Wang, A. Yamamoto, and T. Higuchi, "Electrostatic-motor-driven electroadhesive robot," in *IEEE/RSJ IROS*, 2012, p. 914.

[123] G. Warwick, "Orbital Recyling," *Aviation Week and Space Technology*, vol. 175, no. 4, 2013.

[124] J. P. Whitney, P. S. Sreetharan, K. Y. Ma, and R. J. Wood, "Pop-up book MEMS," *J. Micromech. Microeng.*, vol. 21, no. 11, p. 115021, nov 2011.

[125] R. Wood, E. Steltz, and R. Fearing, "Optimal energy density piezoelectric bending actuators," *Sens. Actuators. A Phys.*, vol. 119, no. 2, pp. 476–488, 2005.

[126] R. J. Wood, S. Avadhanula, R. Sahai, E. Steltz, and R. S. Fearing, "Microrobot design using fiber reinforced composites," *J. Mech. Des.*, vol. 130, no. 5, p. 052304, 2008.

[127] Z. Yang, B. Jeong, A. Vakakis, and S. Kim, "A tip-tilt-piston micromirror with an elastomeric universal joint fabricated via micromasonry," *J. Microelectromech. Syst.*, vol. 24, no. 2, pp. 262–264, 2015.

[128] R. Yeh, S. Hollar, and K. Pister, "Single mask, large force, and large displacement electrostatic linear inchworm motors," *J. Microelectromech. Syst.*, vol. 11, no. 4, pp. 330–336, 2002.

[129] X. Zhang, Z. Yu, C. Wang, D. Zarrouk, J.-W. T. Seo, J. C. Cheng, A. D. Buchan, K. Takei, Y. Zhao, J. W. Ager, J. Zhang, M. Hettick, M. C. Hersam, A. P. Pisano, R. S. Fearing, and A. Javey, "Photoactuators and motors based on carbon nanotubes with selective chirality distributions," *Nature Communications*, vol. 5, pp. 1–8, 2014.

Appendix A

Fabrication Process Details

For the reader's benefit and to assist in replication of this research / advancement of future research, we have included additional fabrication process details not provided in the various chapters. All manufacturing settings are appropriate for the equipment utilized in the Biomemetic Millisystems Lab.

All processes are suitable for fabricating 2-sided thin-film actuator layers. For various stages of research, the following processes are recommended:

- **Prototyping Methods** – A.1.1, A.2

- **Bulk-Production Methods** – A.1.2, A.3

A.1   Wet Etching Process

A.1.1   In-House

This is the recipe for performing in-house fabrication of actuator layers. Layers were manufactured out of Dupont Pyralux AP 8515 copper-clad polyimide laminates.

1. Materials

   - Substrate – Dupont, Pyralux AP 8515
   - Mask – Dupont, Kapton 100 HN (25 μm)
   - Adhesive – GBC, Octavia Hot Mount Sheet Adhesive (18 μm)

2. Equipment

   - Laser-Cutter – PhotoMachining, Inc. (PMI), 355 nm Laser
   - Cutting Surface – Rigid plate coated with GelPak, WF Film X8

- Laminator – Professional Laminating Systems, Inc., PL-1200 hp
- Etchant – Ferric Chloride ($FeCl_3$)

3. Preparation

   a) Cut 60 x 60 mm squares of Substrate (x1), Mask (x2), and Adhesive (x2).

   b) Laminate one Adhesive sheet to each Mask sheet at +220°F.

   c) Remove Adhesive backing, and lightly attach Mask / Adhesive to Substrate (on both sides). This assembly is referred to as the Composite. **Do Not Laminate.**

4. Cutting

   a) Secure Composite onto the GelPak-covered cutting surface

   b) Place Composite in the Laser, then adjust focus height and alignment.

   c) Cut alignment marks (through all)
      - Power – 70%
      - Speed – 10 mm/s
      - Passes – 25x

   d) Cut mask (front side mask only)
      - Power – 60%
      - Speed – 30 mm/s
      - Passes – 6x

   e) Remove Composite from GelPak.

   f) Flip Composite over and resecure to GelPak.

   g) Align Composite in the Laser according to the previously cut alignment marks.

   h) Cut mask (back side mask only)
      - Power – 60%
      - Speed – 30 mm/s
      - Passes – 6x

   i) Cut actuator extents (through all)
      - Power – 70%
      - Speed – 30 mm/s
      - Passes – 25x

   j) Remove Composite cutouts – now referred to as actuator Layers – from GelPak.

5. Etching

   a) Peel patterned Mask off of Layers to expose Cu to be etched.

b) Laminate Layers at +220°F (to secure patterned Masks to Substrate).

c) Wipe away excess exposed Adhesive using cloth coated in acetone.

d) Submerge Layers in $FeCl_3$ bath.

e) Etch for approx. 30 mins (or until all exposed Cu is removed). Agitate as necessary. Heat bath to 40°C for accelerated etching.

f) Remove Layers from $FeCl_3$ bath and wipe away excess etchant.

g) Rinse Layers with water (to remove etchant).

6. Cleaning

a) Soak Layers in acetone (to release Mask). Agitate as necessary.

b) Rinse Layers with water (to remove etchant / residue).

A.1.2   Outsourced

Fabrication of flex-circuit actuator layers was also outsourced to a commercial vendor. This is the contact information for a reliable vendor:

Boardworks, Inc. (Rod Appeldorn)

- (510) 832-2228 (Work)

- (510) 418-1072 (Cell)

- boardworks@aol.com

- The Boardworks c/o Rob Appeldorn
  5700 Balboa Dr.
  Oakland, Calif. 94611

Average lead time of under 1 week, and responsive to custom designs / process requests. Supply AutoCAD or Gerber files.

Layers were manufactured out of Dupont Pyralux AP 8515 copper-clad polyimide laminates. Layers are returned as a single sheet with patterned copper electrodes (1- or 2-sided) in an array on the polyimide substrate. The layers are post-processed in lab: actuator extents (springs, etc.) are cut into the polyimide substrate using the Laser-Cutter described throughout this dissertation.

A.2   Laser Cutting Process

This is the recipe for performing in-house fabrication of actuator layers, using metal foil (12.7 μm Stainless Steel) laminated onto a polyimide substrate (25 μm Polyimide).

1. Materials

    - Substrate – Dupont, Kapton 100 HN (25 μm)
    - Electrode – Trinity Brand Industries, Stainless Steel (12.7 μm)
    - Adhesive – GBC, Octavia Hot Mount Sheet Adhesive (18 μm)

2. Equipment

    - Laser-Cutter – PhotoMachining, Inc. (PMI), Coherent Matrix Laser (355 nm, 2 $Watt$)
    - Cutting Surface – Rigid plate coated with GelPak, WF Film X8
    - Laminator – Professional Laminating Systems, Inc., PL-1200 hp
    - Microscope – Zeiss, Stemi 2000-C

3. Preparation

    a) Cut 60 x 60 mm squares of Substrate (x1), Electrode (x2), and Adhesive (x2) material.
    b) Laminate one Adhesive sheet to each Electrode sheet at +220°F.

4. Cutting

    a) Remove Adhesive backings from Electrode sheets
    b) Secure Substrate and Electrode (Adhesive side up) sheets onto GelPak.
    c) Place in the Laser, then adjust focus height and alignment.
    d) Pattern Substrate
        - Power – 70%
        - Speed – 11 mm/s
        - Passes – 2x
    e) Pattern Top and Bottom Electrodes on the separate Electrode sheets. Include the Substrate outline around the Electrode patterns for subsequent alignment.
        - Power – 70%
        - Speed – 11 mm/s
        - Passes – 4x

5. Assembly

    a) Remove patterned Substrate sheets from the GelPak.

    b) Remove scrap material from around Electrode patterns on each Electrode sheet (between Electrode pattern and Substrate outline, only).

    c) Align and place Substrate sheet over one Electrode pattern (using Substrate outline for alignment).

    d) Place a heated, flat metal block (heated to +220°F) on top of the Substrate, to partially bond the Electrode and Substrate.

    e) Peel off the Electrode / Substrate from the GelPak.

    f) Laminate Layers at +220°F (to fully bond the patterned Electrode to Substrate).

    g) Repeat alignment, placement, heating, peeling, and lamination steps with the reverse side of the Substrate and the second Electrode pattern. Ensure careful alignment of the Electrodes between the two sides of the Substrate.

A.3 Printing Process

Actuators were also fabricated via screen printing: electrode patterns were printed in silver conductor ink (Dupont 5025) directly onto a variety of substrates, including Dupont Kapton FPC (thermally-stable Kapton), Photo Paper (Staples), Vellum (Blick, non-animal), and Ripstop Nylon (see Fig. A.1). Screen printing was performed in the Arias Lab, using either a manual or automated screen printer (ASYS Group, ASP01M) and a commercial Screen. This is the contact information for acquiring patterned Screens for screen printing:

Dynamesh, Inc.

- (800) 235-5056

- dynamesh.com

- 512 Kingsland Drive
  Batavia, Ill. 60510

Screens consisted of 15 x 15 *inch* (ID) solid-core frames with 325 Stainless Steel (0.9 *mil* diameter) woven mesh (49–53 μm total thickness) and coated in a MM1 emulsion (10-15 μm thick). The emulsion is patterned lithographically into the desired electrode shapes.

The automated screen printer was capable of printing both 1- and 2-sided actuators, using cameras to monitor alignment features. Sheets of printed actuators up to 10 x 15 *cm* were successfully printed. The layers are post-processed in the Fearing Lab, as described in other processes: actuator extents (springs, etc.) are cut into the substrate using the UV Laser-Cutter.
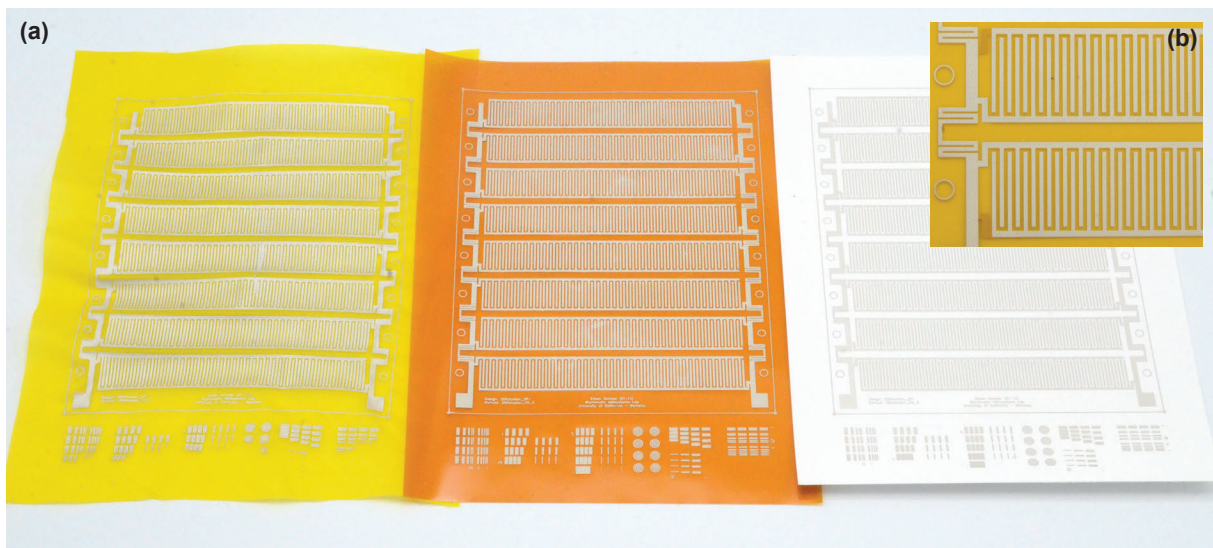
Figure A.1: RFAs printed with Dupont 5025 silver conductor ink on a variety of substrates (a), and with 2-sided printing (b). Substrates include (left to right): rip-stop nylon, polyimide, and photo-paper. The 2-sided RFA is printed on 25 μm thick polyimide.

Appendix B

MATLAB Code

Code for the Electrostatics Simulation is inconveniently long to include in this dissertation, but is available upon request.